DOCTORAL THESIS

Fabrication of Novel Metal, Nitrogen Co-doped Carbon Materials based on a Unique Organic Ligand

Mahboob Alam

TALLINNA TEHNIKAÜLIKOOL
TALLINN UNIVERSITY OF TECHNOLOGY
TALLINN 2022

TALLINN UNIVERSITY OF TECHNOLOGY
DOCTORAL THESIS
59/2022

Fabrication of Novel Metal, Nitrogen Co-doped Carbon Materials based on a Unique Organic Ligand

MAHBOOB ALAM

TALTECH
PRESS

TALLINN UNIVERSITY OF TECHNOLOGY
School of Science
Department of Chemistry and Biotechnology

This dissertation was accepted for the defense of the degree of Doctor of Philosophy in Chemistry on September 22, 2022

Supervisor	Dr Pavel Starkov Dept of Chemistry and Biotechnology Tallinn University of Technology Tallinn, Estonia
Co-supervisor	Associate Professor Nadežda Kongi Institute of Chemistry University of Tartu Tartu, Estonia
External examiners	Dr Roman Mysyk Centre for Cooperative Research on Alternative Energies Basque Research and Technology Alliance Vitoria-Gasteiz, Spain
	Dr Sander Ratso National Institute of Chemical Physics and Biophysics Tallinn, Estonia

Defense of the thesis: October 19, 2022, Tallinn

Declaration:
I, Mahboob Alam, confirm that the work presented in this thesis is my own. Where information has been derived from other sources, I confirm that it has been indicated and acknowledged. This thesis has not been submitted for doctoral or equivalent academic degree at any other institution.

European Union
European Regional
Development Fund

Investing
in your future

ISSN 2585-6898 (publication)
ISBN 978-9949-83-909-4 (publication)
ISSN 2585-6901 (PDF)
ISBN 978-9949-83-910-0 (PDF)
Printed by Koopia Niini & Rauam

TALLINNA TEHNIKAÜLIKOOL
DOKTORITÖÖ
59/2022

Uue orgaanilise ligandi kasutuselevõtt metalli ja lämmastikuga rikastatud süsinikmaterjalide sünteesimiseks

MAHBOOB ALAM

TALTECH
KIRJASTUS

Dedicated to my parents
Alam Sher and Sureyya Nosheen Alam

Contents

List of publications

I Ping, K.; Brashinsky, A.; Alam, M.; Bhadoria, R.; Mihkli, V.; Mere, A.; Vlassov, S.; Kook, M.; Rähn, M.; Sammelselg, V.; Aruväli, J.; Tammeveski, K.; Kongi, N.; Starkov, P.

Fused hybrid linkers for metal–organic framework-derived bifunctional oxygen electrocatalysts.

ACS Appl. Energy Mater. **2020,** *3,* 152–157.

DOI:10.1021/acsaem.9b02039

II Ping, K.; Alam, M.; Kahnert, S. R.; Bhadoria, R.; Mere, A.; Mikli, V.; Käärik, M.; Aruväli, J.; Paiste, P.; Kikas, A.; Kisand, V.; Järving, I.; Leis, J.; Tammeveski, K.; Kongi, N.; Starkov, P.

Multi-purpose chemo- and electrocatalyst material from an amorphous cobalt metal–organic framework.

Mater. Adv. **2021,** *2,* 4005–4019.

DOI:10.1039/D1MA00414J

III Avila-Bolívar, B.; Cepitis, R.; Alam, M.; Assafrei, J.-M.; Ping, K.; Aruväli, J.; Kikas, A.; Kisand, V.; Vlassov, S.; Käärik, M.; Leis, J.; Ivaništštev, V.; Starkov, P.; Montiel, V.; Solla-Gullón, J.; Kongi, N.

CO_2 Reduction to formate on an affordable bismuth metal-organic framework based catalyst.

J. CO_2 Util. **2022,** *59,* 101937.

DOI:10.1016/j.jcou.2022.101937

IV Alam, M.; Ping, K.; Danilson, M.; Mikli, V.; Käärik, M.; Leis, J.; Aruväli, J.; Paiste, P.; Rähn, M.; Sammelselg, V.; Tammeveski, K.; Kramm, U.; Kongi, N.; Starkov, P.

Comparison of benzimidazolediol-derived iron triad M–N–C nanomaterials as trifunctional catalysts in alkaline and acidic media

Manuscript submitted.

Author contribution

I Electrochemical characterization of MOF-derived materials; writing of the manuscript and the SI

II Electrochemical characterization of MOF-derived materials; assembly and testing of solid state zinc–air battery; writing of the manuscript and the SI

III Preparation and physical characterization of MOF-derived materials; writing of the manuscript and the SI

IV Preparation and electrochemical characterization of MOF-derived materials; assembly and testing of batteries; writing of the manuscript and the SI

Abbreviations

Ac	acetyl
acac	acetylacetonate
BET	Brunauer−Emmett−Teller method
CNT	carbon nanotube
CO_2RR	carbondioxide reduction reaction
CV	cyclic voltammetry/cyclic voltammograms
DABCO	1,4-diazabicyclo[2.2.2]octane
DCDA	dicyandiamide
DMSO	dimethyl sulfoxide
DAP	2,6-diacetylpyridine
DAB	3,3′-diaminobenzidine
EDTMPS	sodium ethylenediamine tetra(methylenephosphonicacid)
FC	fuel cell
FTIR	Fourier transform infrared spectroscopy
GC	glassy carbon
GO	graphene oxide
h	hour
HAADF	high-angle annular dark-field
HER	hydrogen evolution reaction
HMT–PMBI	hexamethyl-p-terphenyl poly(benzimidazolium)
HEDP	1-hydroxyethylidene-1,1-diphosphonic acid
K–L	Koutecky−Levich
MAB	metal–air battery
Me	methyl
mel	melamine
2-mim	2-methylimidazole
MNC	metal, nitrogen-doped carbon
$M–N_x$	nitrogen coordinated metal center
MOF	metal–organic framework
NMR	nuclear magnetic resonance
NP	nanoparticle
NRR	nitrogen reduction reaction
OAc	acetate
OER	oxygen evolution reaction
ORR	oxygen reduction reaction
P123	Pluronic P123 cros-sblock polymer
PGM	platinum group metal
Ph	phenyl
PPy	polypyrrole nanowires

PTFE	polytetrafluoroethylene
PVP	polyvinylpyrrolidone
PXRD	powder X-ray diffraction
Py	pyridinyl
RDE	rotating disk electrode
RRDE	rotating ring disk electrode
ref	reference
rGO	reduced graphene oxide
SEM	scanning electron microscopy
SI	supporting information
STEM	scanning transmission electron microscopy
TEM	transmission electron microscopy
THB	1,3,5-tris (4′-hydroxy-5′-formylphenyl) benzene
TOP	trioctylphosphine
TCPP	tetra(4-carboxyphenyl)porphyrin
UV	ultraviolet
XPS	X-ray photoelectron spectroscopy

Introduction

The nexus of electrochemical processes is the use of heterogenous electrocatalyst materials. They can and should be tailored with a high level of precision and control to broaden their use.

In this doctoral thesis, I developed and optimized several metal, nitrogen-doped carbon (MNC) electrocatalyst materials. These novel materials were derived from polycrystalline and amorphous metal–organic frameworks (MOFs), which contained various non-platinum group metals such as iron, cobalt, nickel and bismuth for various applications including oxygen reduction reaction (ORR), oxygen evolution reaction (OER) and hydrogen evolution reaction (HER). In addition, multimetallic systems based on iron triad metals have been screened. With the best performing materials in hand, I have fabricated single fuel cells and zinc–air batteries. These studies emphasize the use of rationally designed organic linkers in electrocatalysis and the potential of this approach in energy conversion and storage devices.

Chapter 1 gives a short overview of MNC materials used for the electrochemical conversions of small molecules (CO_2, H_2O, N_2, O_2). Chapter 2 focuses on novel iron and cobalt based electrocatalysts used in electrochemical reactions such as ORR, OER and HER. In Chapter 3, I introduce and electrochemically evaluate multimetallic materials developed on the basis of combinations of various iron triad metals (Fe, Co, Ni), which were prepared using 1*H*-benzo[*d*]imidazole-5,6-diol as an alternative organic ligand. In Chaptrer 4, the same linker was used to fabricate optimized MNC materials that incorporate Bi(0) nanoparticles for their use in electrochemical reduction of CO_2 to formate.

1 MNC catalyst materials for energy demand

In this Chapter, I present a concise description of the metal, nitrogen-doped carbon (MNC) based materials used in energy conversion and storage devices. I also briefly summarize electrochemical conversions that were used to test their performance.

The EU aims to become climate-neutral by the year 2050, which is in line with the Paris Agreement [1] and the EU Green Deal [2]. The ultimate goal of the electrocatalysis is to use renewable energy to convert small molecules (H_2O, N_2 and CO_2) into high value added products, e.g. methane, alcohols, formic acid and ammonia (Fig. 1) [3–6]. These transformations also present us with an opportunity to store energy. For example, conversion of water to hydrogen gives rise to hydrogen, which can be used as fuel. Although electrochemical conversions are thermodynamically feasible, there are some outstanding issues with their long-term performances, which mainly come down to optimization of materials and device engineering. In case of the materials used, a special attention needs to be drawn to their activity, selectivity for a particular process and durability [7].

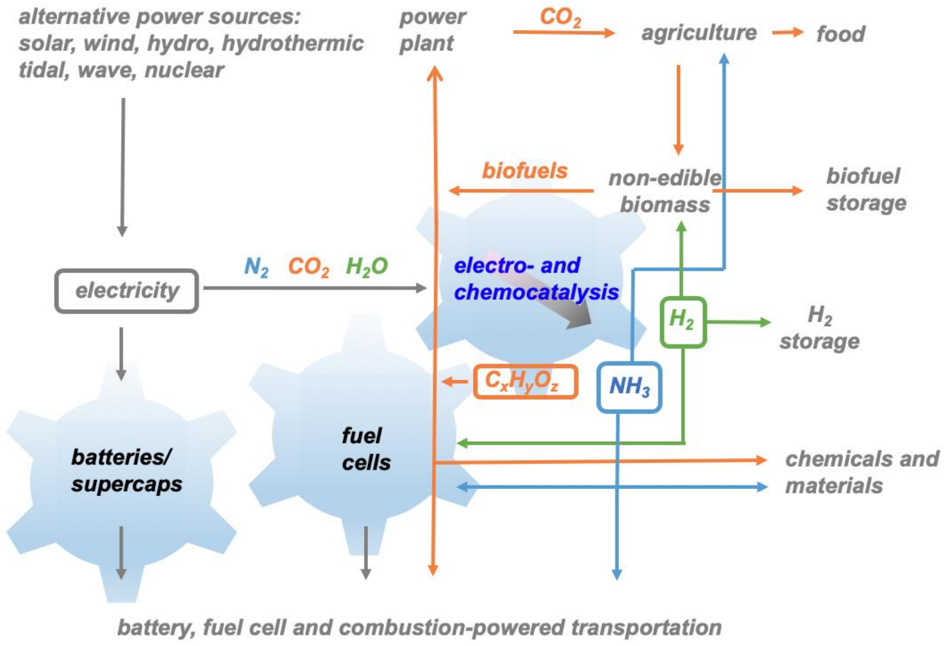

Figure 1. *Electrochemical conversions as the engine for circular economy. Figure adapted with permission from Pavel Starkov (the author).*

Metal-containing nitrogen-doped carbon materials are relatively inexpensive; however, they may often lack chemical stability and require rounds of optimization to be directly employed in the large-scale applications (Table 1) [8–12]. Availability of various fabrication routes helps finetune the underlying materials through changing several chemical and physical properties, e.g. their conductivity, stability, porosity and surface morphology.

Table 1 *Comparison of various parameters for trifunctional ORR/OER/HER catalysts.*

entry	***catalyst***	***precursors***	***catalyst loading*** mg cm $^{-2}$	***ORR*** $E_{1/2}$ @−3 mA cm^{-2} @1600 rpm	***OER*** E_{10} @10mA cm^{-2} @1600 rpm	***ΔE***	***HER*** –E_{-10} @10 mA cm^{-2} @1600 rpm	***reference***
cobalt-based materials								
1	**Co/MMCs**	PPy + carbon fibers + $CoCl_2$	0.22	0.84 (1 M KOH)	1.41 (1 M KOH)	0.57	0.086 (1 M KOH)	[13]
2	**Co/CNFs (1000)**	Co foil + melamine	0.3	0.896 (0.1 M KOH)	1.55 (1 M KOH)	0.65	0.19 (1 M KOH)	[14]
3	**Co_2B/Co/N-B-C/B_4C**	B_4C + $Co(OAc)_2$ + melamine	0.127	0.83 (0.1 M KOH)	1.53 (0.1 M KOH)	0.70	0.22 (0.1 M KOH)	[15]
4	**CoT@NC**	NH_4@$Zn_3OH(PzC)_3$	0.2	0.86 (0.1 M KOH)	1.58 (1 M KOH)	0.72	0.209 (1 M KOH)	[16]
5	**Co_4N@NC-2**	ZIF-67	0.3	0.84 (0.1 M KOH)	1.52 (0.1 M KOH)	0.68	0.283 (1 M KOH)	[17]
6	**Co@N-C-800**	THB + $Co(OAc)_2$	0.36	0.85 (0.1 M KOH)	1.58 (1 M KOH)	0.73	0.292 (0.5 M H_2SO_4)	[18]
7	***TAL-2-900***	***$CoCl_2$ + L1***	***0.50***	***0.85 (0.1 M KOH)***	***1.60 (0.1 M KOH)***	***0.75***	***0.264 (1 M KOH) 0.289 (0.5 M H_2SO_4)***	[19]
8	**Co@N-CNTF**	$Co(OAc)_2$ + adenine	0.28	0.81 (0.1 M KOH)	1.58 (1 M KOH)	0.77	0.26 (1 M KOH)	[20]
9	**Co/NGC-3**	g-C_3N_4 + glucose + ZIF-67	0.20	0.85 (0.1 M KOH)	1.636 (0.1 M KOH)	0.786	0.293 (0.1 M KOH)	[21]
10	**D–Co@CNG**	GO + $Co(NO_3)_2$ + $Zn(NO_3)_2$ + 2-MIM	0.20	0.81 (0.1 M KOH)	1.60 (1 M KOH)	0.79	0.205 (1 M KOH)	[22]
11	**Co/CoO@Co–N-C-800**	shrimp-shell + $Co(NO_3)_2$ + pyrrole	0.305	0.854 (0.1 M KOH)	1.664 (0.1 M KOH)	0.81	0.376 (0.1 M KOH) (@20 mA cm^{-2})	[23]
12	**Co_2P**	$Co(acac)_2$ + TOP	0.2	0.839 (0.1 M KOH)	1.51 (1 M KOH)	0.671	0.075 (1 M KOH)	[24]

13	**CoP NPs/CNSs**	$Co(OAc)_2$ + melamine + phytic acid	0.25	0.88 (0.1 M KOH)	1.58 (1 M KOH)	0.7	0.115 (1 M KOH)	[25]
14	**Co_2P/CoNPC**	ZIF-67 + red phosphorus	0.39	0.843 (0.1 M KOH)	1.556 (1 M KOH)	0.713	0.28 (1 M KOH)	[26]
15	**Co_2P/NPG–900**	$CoPc(NH_2)_4$ + GO + $Cl_6N_3P_3$	0.254	0.81 (0.1 M KOH)	1.55 (1 M KOH)	0.74	0.245 (1 M KOH)	[27]
16	**CoP@SNC**	$Co(Ac)_2$·+ HEDP	0.6	0.79 (0.1 M KOH)	1.58 (1 M KOH)	0.79	0.174 (1 M KOH)	[28]
17	**Co_2P/CoN in NCNTs**	melamine + P123 + TPP + $Co(NO_3)_2$	0.1	0.85 (0.1 M KOH)	1.65 (0.1 M KOH)	0.80	0.098 (0.5 M H_2SO_4)	[29]
18	**CoP-PBSCF**	$NaH_2PO_2·H_2O$ + H-PBSCF	0.255	0.752 (0.1 M KOH)	1.57 (0.1 M KOH)	0.81	0.24 (0.1 M KOH)	[30]
19	**Co-B-O/NPC–50%**	$Co(Ac)_2$+ $NaBH_4$ + lecithin + g-C_3N_4	0.42	0.83 (0.1 M KOH)	1.58 (1 M KOH)	0.753	0.316 (1 M KOH)	[31]
20	**CoSA+Co_9S_8/HCNT**	ZnS + ZIF-67 + polydopamine	NA	0.855 (0.1 M KOH)	1.56 (0.1 M KOH)	0.705	0.25 (1 M KOH)	[32]
21	**NS/rGO-Co_4**	$Co(NO_3)_2$ + thiourea + GO + sodium dodecyl benzene sulfonate (SDBS)	0.404	0.79 (0.1 M KOH)	1.495 (0.1 M KOH)	0.705	0.15 (0.5 M H_2SO_4)	[33]
22	**$Co_{0.85}$Se@NC**	ZIF-67 + Se	0.20	0.817 (0.1 M KOH)	1.55 (1 M KOH)	0.733	0.230 (1 M KOH)	[34]
23	**DAP–DAB–$Co(OAc)_2·4H_2O$**	DAP +DAB + $Co(OAc)_2$	0.30	0.90 (0.1 M KOH)	1.62 (0.1 M KOH)	0.72	0.20 (1 M KOH)	[35]
24	**CF–NG–Co**	$Co(Ac)_2$ + GO + melamine	0.28	0.88 (0.1 M KOH)	1.63 (1 M KOH)	0.75	0.212 (1 M KOH)	[36]
iron-based materials								
25	**BA-TAP-Fe-800**	2,4,6-triaminopyrimidine + barbituric acid + $FeCl_3$	0.283	0.85 (0.1 M KOH)	1.55 (0.1 M KOH)	0.7	0.33 (0.1 M KOH)	[37]
26	**FeP_x/Fe-N-C/NPC**	tannic acid + $FeCl_2·4H_2O$ + Na_2HPO_4	0.21/0.42 (HER)	0.86 (0.1 M KOH)	1.565 (1 M KOH)	0.705	0.075 (0.5 M H_2SO_4)	[38]
27	**PPy/FeTCPP/Co**	pyrrole + FeTCPP + $Co(NO_3)_2$	0.3	0.86 (0.1 M KOH)	1.61 (0.1 M KOH)	0.75	0.24 (0.1 M KOH)	[39]
28	**FeS/Fe_3C@N-S-C-800**	benzenetricarboxylic acid + $Pd(PPh_3)_4$ + 3,8-DBPT-dibromophenanthroline + $Fe(OAc)_2$ + DMSO	0.3/0.6	0.87 (0.1 M KOH)	1.80 (1 M KOH)	0.93	0.174 (0.5 M H_2SO_4)	[40]

other metal based materials [Ni, W, Ru, Mo]								
29	**Ni-NC700**	$Ni(NO_3)_2$+ 2,6-pyridine dicarboxylic acid + 4,4′-bipy	0.31	0.75 (0.1 M KOH)	1.66 (0.1 M KOH)	0.91	0.301 (0.1 M KOH)	[41]
30	**W_2N/WC**	WO_3 powder + DCDA	0.20	0.83 (0.1 M KOH)	1.56 (1 M KOH)	0.73	0.148 (1 M KOH)	[42]
31	**Ru-SA/$Ti_3C_2T_x$**	Ti_3AlC_2 + $RuCl_3$	0.61	0.80 (0.1 M $HClO_4$)	1.53 (0.1 M $HClO_4$)	0.73	0.07 (0.5 M H_2SO_4)	[43]
32	**G@N-MoS_2**	sulfur + $MoCl_5$ + MgO + NH_3	0.25	0.716 (0.1 M KOH)	1.63 (0.1 M KOH)	0.914	0.243 (0.5 M H_2SO_4)	[44]
multi-transition-metals based materials								
33	**CoO_x-NeC/TiO_2C (22.7%)**	$Ti_3C_2T_x$ + $Co(NO_3)_2$ + $Zn(NO_3)_2$ + 2-mim	0.141	0.85 (0.1 M KOH)	1.58 (1 M KOH)	0.72	0.367 (1 M KOH)	[45]
34	**N/CF-EC-900**	$Co(NO_3)_2$ + $Fe(NO_3)_3$ + albumin	0.17	0.849 (0.1 M KOH)	1.61 (0.1 M KOH)	0.761	0.164 (0.1 M KOH)	[46]
35	**IrO_2-ZnO**	$ZnCl_2$ + $IrCl_3$ + NH_3	0.2547	0.81 (1 M KOH)	1.59 (1 M KOH)	0.78	0.25 (1 M KOH)	[47]
36	**ZnCo−PVP-900**	$Zn(NO_3)_2$ + $K_3Co(CN)_6$ + PVP	0.28	0.83 (0.1 M KOH)	1.63 (1 M KOH)	0.80	0.25 (1 M KOH)	[48]
37	**Co_2Mn_1 DH**	$Mn(NO_3)_2$ + $Co(NO_3)_2$	0.25	0.78 (0.1 M KOH)	1.58 0.1 M KOH	0.80	0.187 (1 M KOH)	[49]
38	**Ni_2P/CoN-PCP**	$NiCl_2$ + CoN–PCP support + NaH_2PO_2 +	0.26	0.871 (0.1 M KOH)	1.50 (1 M KOH)	0.629	0.094 (1 M KOH)	[50]
39	**NiCoP/CNF-900**	polyacrylonitrile + $Ni(NO_3)_2$ + $Co(NO_3)_2$ + red P	NA	0.82 (0.1 M KOH)	1.508 (1 M KOH)	0.688	0.130 (1 M KOH)	[51]
40	**FeNi@N-CNT/NCSs**	g-C_3N_4 + aniline + $Fe(NO_3)_3$ + $Ni(NO_3)_2$	0.255	0.84 (0.1 M KOH)	1.59 (0.1 M KOH)	0.75	0.203 (1 M KOH)	[52]
41	**Pt/NiO/Ni/CNT-3**	CNTs + Zn plate + $NiCl_2$ + K_2PtCl_6	0.255	0.94 (0.1 M KOH)	1.7 (0.1 M KOH)	0.76	0.117 (0.1 M KOH)	[53]
42	**CoP/Ni_2P@NC**	$CoCl_2{\cdot}6H_2O$ + $NiCl_2{\cdot}6H_2O$ + EDTMPS	NA	0.79 (0.1 M KOH)	1.57 (1 M KOH)	0.78	0.330 (1 M KOH)	[54]
43	**NiCoOS**	ZIF-67 + $Ni(NO_3)_2{\cdot}6H_2O$ + thioacetamide	0.318	0.79 (0.1 M KOH)	1.7 (0.1 M KOH)	0.91	0.3 (0.1 M KOH)	[55]
44	**FeCo/Co_2P@NPCF**	bacterial cellulose + $K_3[Fe(CN)_6]$ + $CoCl_2$ + melamine + phytic acid	0.28	0.79 (0.1 M KOH)	1.56 (0.1 M KOH)	0.77	0.26 (1 M KOH)	[56]

45	**Rh_6Cu_1/C**	$RhCl_3$ + $CuCl_2$+ PVP + ascorbic acid	0.282	0.85 (0.1 M KOH)	1.54 (1 M KOH)	0.69	0.017 (0.5 M H_2SO_4)	[57]
46	**Co_9S_8@MoS_2**	$Co(OAc)_2$ + Na_2MoO_4 + PVP	0.407	0.88 (0.1 M KOH)	1.57 (1 M KOH)	0.69	0.143 (1 M KOH)	[58]
47	**O-$Co_{0.5}Mo_{0.5}Se_2$**	nickel foam + $Co(NO_3)_2$ + Na_2MoO_4 + hexamethylenetetramine + Se	NA	0.83 (0.1 M KOH)	1.406 (1 M KOH)	0.576	0.102 (1 M KOH)	[59]
48	**Co_9S_8-MoS_2/N-CNAs@CNFs**	$Zn(NO_3)_2$ + $Co(NO_3)_2$ + 2-MIM + Na_2MoO_4	0.17	0.82 (0.1 M KOH)	1.57 (1 M KOH)	0.75	0.163 (1 M KOH)	[60]
49	**$Co_{5.47}N$@Co_3Fe_7/N-C**	urea + GO + oxidized CNTs + $FeCl_3$ + $CoCl_2$	0.60	0.94 (0.1 M KOH)	1.72 (0.1 M KOH)	0.78	0.181, (1 M KOH) 0.115, (0.5 M H_2SO_4)	[61]
50	**Cu-foam@CuCoNC–500**	$Cu(OH)_2$ + Cu foam + $Co(NO_3)$ + dimethylimidazole	NA	0.84 (0.1 M KOH)	1.485 (1 M KOH)	0.645	0.059 (1 M KOH)	[62]
51	**Fe_3C-Co/NC**	P123 + $Co(NO_3)_2$ + $Fe(NO_3)_3$ + melamine	0.2 ORR 0.4 OER 0.3 HER	0.885 (0.1 M KOH)	1.58 (1 M KOH)	0.695	0.238 (1 M KOH)	[63]
non-metal based materials								
52	**SHG**	melamine + $NiSO_4$ + KCl	0.71	0.87 (0.1 M KOH)	1.60 (0.1 M KOH)	0.73	0.31 (0.1 M KOH)	[64]
53	**NOGB-800**	sodium citrate + $Co(NO_3)_2$ + $K_3[Fe(CN)_6]$ + dopamine	0.4	0.84 (0.1 M KOH)	1.65 (1 M KOH)	0.81	0.22 (1 M KOH)	[65]
54	**N-doped graphene**	graphene + melamine	0.283	0.76 (0.1 M KOH)	1.57 (1 M KOH)	0.81	0.15 (0.5 M H_2SO_4)	[66]
55	**NCN-1000-5**	citric acid + NH_4Cl	0.2	0.82 (0.1 M KOH)	1.64 (0.1 M KOH)	0.82	0.09 (0.5 M H_2SO_4)	[67]

MNC materials can be inferior to the electrocatalysts containing precious metals (Pt, Pd, Ru, Ir) [68,7]. Such materials are essential to overcome the burden exerted by the scarcity and high prices of noble metals. In the future, by using these novel energy materials the dependency on fossil fuels is prospected to be reduced.

The porosity and nanostructure of MNC materials play an important role in catalytic performance, albeit the molecular nature of specific active centers is not always completely understood. To reduce the ambiguity, these materials are subject to acid etching to remove metal impurities, which are present at the surface. The catalytic activity may sometimes get affected due to harsh acidic etching due to metal leaching from the metal sites. To alleviate these issues, polymer templates and silica nanoparticles are used to retain the original porous structure [69].

In addition to more conventional uses in ORR, OER and HER (Table 1), MNC materials can also be engineered to address selective CO_2 conversion to various products including carbon oxide [70,71,72] and methane [73,74]. Copper and bismuth are considered as big contenders for efficient CO_2 reduction reaction (CO_2RR) to produce alcohols and hydrocarbons [75].

Preparation of MNC materials heavily relies on carbonization of organometallic compounds or a mixture of transition metal salts with nitrogen and carbon sources. Often additional heteroatoms are used to dope the materials to increase activity and durability without significantly increasing their cost of production (Table 2). Alternatively, hydrothermal and solvothermal methods are used to prepare metal containing carbon composites.

To prepare atomically dispersed MNC electrocatalysts, various templating strategies (polymers [76], silica [77], magnesium oxide [78], micelles [79]) have been employed. Metal–organic frameworks can often be used for the templating purposes. Coordination of metal to nitrogen not only creates the number of catalytically active M–N_x sites, but it also helps stabilize metal centers and ensures that the sites are atomically dispersed. Acid etching is used both to remove metal impurities and as sacrificial scaffold [8].

Table 2. *Examples of heteroatom doping.*

heteroatom	*heteroatom source*
boron	$B(OH)_3$ B_2O_3
phosphorous	phytic acid hexachlorocyclophosphazene H_3PO_4 NaH_2PO_2
sulfur	KSCN sulfur thiourea
nitrogen	DCDA melamine DABCO urea thiourea and the metal complexes (Fig. 2)
oxygen	H_2O_2 air
fluorine	NH_4F PTFE

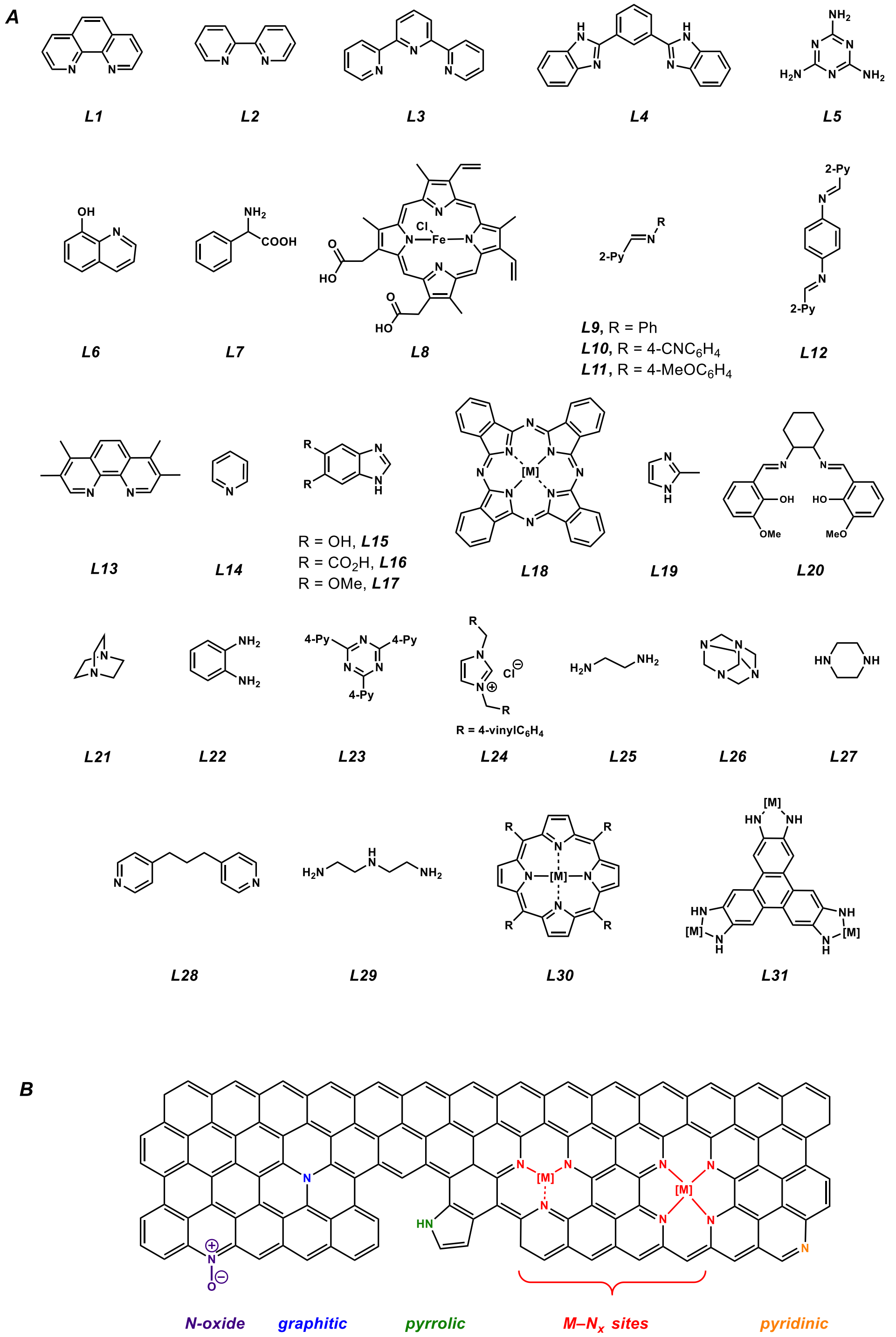

Figure 2. *(A) Widely used nitrogen containing ligands for MNC catalysts. (B) Different nitrogen catalytic sites. Adopted with alterations from [80].*

Metal–organic frameworks (MOFs) form a good general platform to fabricate MNC electrocatalysts and, by varying the organic linkers, one can prepare more sophisticated hybrid materials. Importantly, post-synthetic modifications further help functionalize materials in accordance with specific applications in energy devices [81]. Prominent features of the materials derived from MOFs are their high porosity and high surface area. Both characteristics favor molecular diffusion and catalytic processes. For example, ionic conduction is employed by incorporating guest ions within the pores and integrating post-synthetic strategies to induce polarity [82]. To reduce the cost of production, typically, mechanochemical tools – ball milling and grinding – are used to avoid the use of solvents, and the platinum-group-metals are replaced with more abundant and affordable metals (e.g. iron triad) [83].

Electroconductivity and higher surface area of MNC materials make them viable for the use as supercapacitors [84]. The electrical properties of these materials, accompanied with mesopores, facilitate ion transport and electron transfer. Typically, the carbon sources are graphite, g-C_3N_4 (graphitic carbon nitride) and smaller organic molecules. For example, N-doped wrinkled carbon foils were prepared from 2D MOFs, pyrolyzed in ammonia atmosphere and etched with acid to remove metallic nanoparticles from the surface of the catalyst. These carbon foils are used in sodium storage devices [85].

Lithium ion batteries (LIBs) have gained place in the industrial applications including in electric vehicles [86]. The biggest issue with these devices is the low specific density of metal ion anodes. Most of LIBs are based on intercalation of lithium ions in graphite anode, which assist in enhancing energy density of the metal-ion batteries [87]. Recently, the research agenda has shifted to materials that are economically viable, efficient and hold potential for multifunctional storage. Organic–inorganic hybrid materials serve this purpose very well.

Overall, the MNC composites are one of the alternative solutions to address environmental challenges. Their development receives great attention because of their potential use to transform electricity obtained from renewable energy sources such as wind, solar, nuclear, geothermal and hydroelectric sources. Through advances in molecular engineering they also represent a good platform for many energy conversion and storage devices, including fuel cells, chemical converters, portable and wearable devices.

1.2 Outlook

To meet higher green energy demands, many groups are working on the building blocks used to fabricate MNC materials (different metal sources, heteroatoms and carbon supports). Transitions metals (e.g. Fe, Co, Ni, Cu, Bi) provide a good alternative to platinum group metals. Their use has potential to bring down the cost of the devices. However, to be applicable at the large scale, more work needs to be done to reduce their catalyst loadings and increase their durability. So far, metal–organic frameworks used to produce MNC materials lacked novelty and largely relied on 2-methylimidazole. Although these catalysts were shown to be effective in several applications, their non-modularity prevents us from finetuning the electrocatalyst materials. To address the need for energy conversion and energy storage devices, also the stability of MNC materials has to be considered.

1.3 Aims and objectives

The main objective of this research work was to create new functional materials, which would be derived from a subset of novel metal–organic frameworks. They would be used as precursors to better control activity of materials employed in electrochemical and heterogeneous catalysis applications. Namely,

1. to substitute cost-inefficient constituents such as porphyrins, phthalocyanines, 1,10-phenanthroline with new adaptable carbonaceous ligands based on the benzimidazole core;
2. to assess their catalytic performance in oxygen reduction reaction (ORR), oxygen evolution reactions (OER), hydrogen evolution reaction (HER) and CO_2 reduction reaction (CO_2RR);
3. to formulate electrodes with the most active electrocatalysts and test them in zinc–air batteries and single fuel cells.
4. to test applicability of the new ligand to fabricate MNC materials, which contain various metal(0) nanoparticles.

2 Development of iron and cobalt materials

Three structurally diverse benzimidazoles **TL1**, **TL2** and **TL3** were used to prepare iron and cobalt based catalyst materials TAL-1-900, TAL-6-900, TAL-7-900 and TAL-2-900, TAL-26-900, TAL-27-900, respectively. In the case of TAL-1-900, by testing different metal to ligand ratios, it was shown that there was no impact on the reactivity of the final materials in ORR and OER. As for the cobalt counterpart, which were prepared from amorphous MOF TAL-2, carbonization at different temperatures (800, 900 to 1000 °C) indicated that the material pyrolyzed at 900 °C was the optimal one.

Upon carbonization of various precursors and subsequent acid etching, the materials contained various nanoparticles imbedded into the carbon matrix (Fig. 3A). For example, iron carbide was observed in TAL-1-900 and TAL-7-900 samples, while Fe_3O_4 nanoparticles were detected in TAL-6-900 [88]. In case of the cobalt derived catalysts, only Co(0) nanoparticles were present (Fig. 3E). Acid etching was required to remove much of the nanoparticles (α-Fe in the case of iron catalysts and cobalt oxides in the case of cobalt catalysts) found at the surface of the catalyst. This was done by etching with a mixture of HNO_3 and/or H_2SO_4 (50 °C, 8 h). The samples were then recarbonized to remove sulfonate and nitro groups.

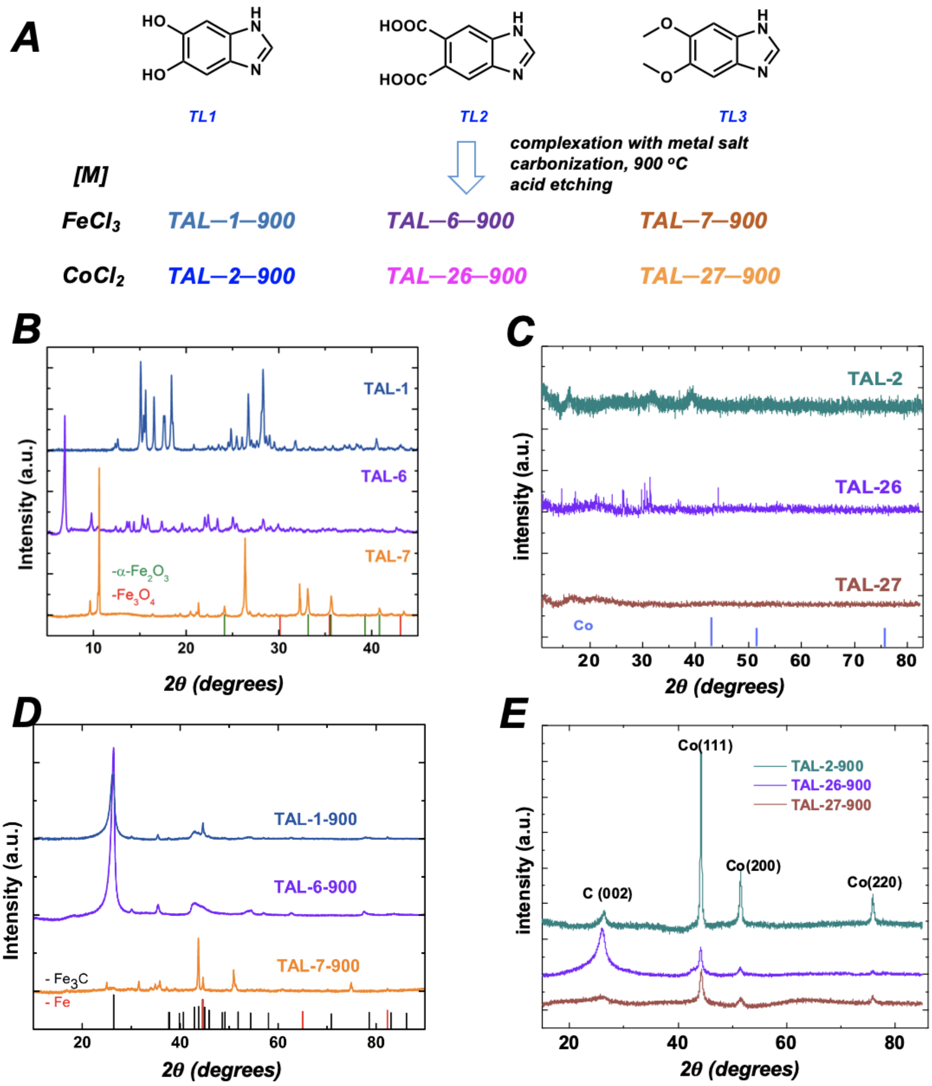

Figure 3. *(A) Preparation of TAL-derived catalyst materials using different organic linkers and metal sources. PXRD patterns for (B) iron TAL MOFs, (C) cobalt TAL MOFs, (D) iron-TAL derived materials, and (E) cobalt-TAL-derived materials.*

We assessed the afore-mentioned catalysts in three classical electrocatalytic transformations – oxygen reduction, oxygen evolution and hydrogen evolution reactions. Rotating disc electrode (RDE) technique was used to perform the measurements. Glassy carbon (GC) electrodes were modified with the material suspended in isopropanol with 5% Nafion, a fluoropolymer/co-polymer, as a binder.

The catalytic performance of MOF derived iron materials (TAL-1-900, TAL-6-900 and TAL-7-900) was assessed in 0.1 M KOH (Fig. 4; 800 μg cm^{-2}). CVs showed larger surface in case of TAL-1-900 as compared to Pt/C within the same potential window [88].

The polarization curves of TAL-1-900 for ORR exhibited a higher halfwave potential (E_{onset} = 1.01 V, $E_{1/2}$ = 0.87 V) than Pt/C ($E_{1/2}$ = 0.85 V). Altogether, TAL-1-900 was more active than TAL-6-900 and TAL-7-900.

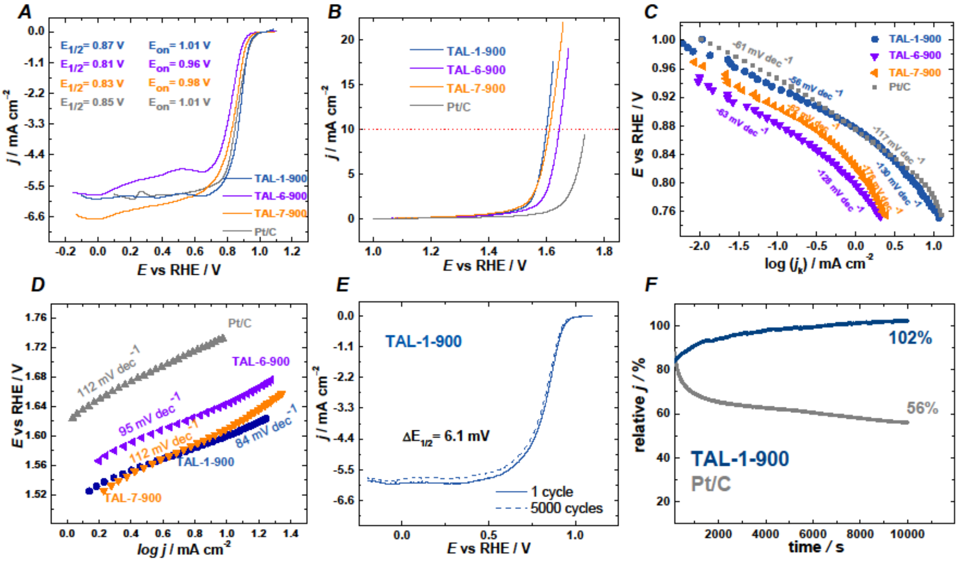

Figure 4. *Electrochemical characterization of iron based TAL electrocatalysts. (A) ORR and (B) OER polarization curves at 1600 rpm with scan rate of 10 mV s^{-1} in 0.1 M KOH. Tafel plots for (C) ORR and (D) OER. (E) ORR stability test for TAL-1-900 over 5000 cycles in the potential range 0.6–1.0 V. (F) OER chronoamperometric measurement at 1.6 V for TAL-1-900.*

The Koutechy–Levich (K–L) and Tafel plots were constructed to better understand the reaction kinetics and the mechanism occurring on the surface of electrode. The linearity of the K–L plots indicated that it was a first order reaction with a number of electrons per O_2 being four. This means dioxygen was converted to water via a *2×2e*$^{-}$ mechanism and that water, not hydrogen peroxide, was produced. The Tafel plot for TAL-1-900 strongly overlapped with that for Pt/C indicated that the reaction mechanisms are similar (Fig. 4C).

The same trend was observed when comparing the OER performances, in which TAL-1-900 (E_{10} = 1.60 V @ 10 mA cm^{-2} vs RHE) had higher activity than TAL-6-900 (E_{10} = 1.64 V), TAL-7-900 (E_{10} = 1.61 V) and Pt/C (E_{10} = 1.73 V), which was used a standard (Fig.4B). The bifunctional performance (ΔE) of all materials in hand was calculated by subtracting $E_{1/2}$ from E_{10}. TAL-1-900 had the lowest value of ΔE = 0.73 V when compared to TAL-6-900 (0.83 V), TAL-7-900 (0.78 V) and $^{\text{ORR}}$Pt/C + $^{\text{OER}}$Pt/C (0.84 V).

Next, TAL-1-900 catalyst was tested for stability. In ORR, TAL-1-900 was cycled in the potential range of 0.6–1.0 V vs RHE for 5000 cycles. The electrocatalyst proved to be stable with only a small change in the halfwave potential ($\Delta E_{1/2}$ = 6.1 mV) (Fig. 4E). Similarly, TAL-1-900 was stable under OER conditions after 5000 cycles in the potential window of 1–1.8 V [88]. To check the durability of TAL-1-900, chronoamperometric test at 1.6 V in 0.1 M KOH was performed for 10000 seconds and compared to Pt/C (Fig. 4F). The enhanced ORR/OER activity of the fabricated electrocatalysts means that these materials hold potential to be employed in real-life applications.

The same three ligands were used to prepare cobalt catalysts TAL-2-900, TAL-26-900 and TAL-27-900 (Fig. 5; catalyst loading 500 µg cm^{-2}). All the materials were carbonized at 900 °C before and etched with 0.5 M HNO_3. The structure–activity dependencies of ligands employed for the preparation of the cobalt and iron materials were similar. In ORR, electrocatalyst TAL-2-900 (E_{onset} = 1.00 V, $E_{1/2}$ = 0.85 V), which was derived from the diol linker, performed better than TAL-26-900 and TAL-27-900. In OER, TAL-2-900 (E_{10} = 1.60 V) outperformed RuO_2 (Fig. 5B). The activity in both ORR and OER conditions was comparable or better than the standards (Fig. 5A).

The ORR stability test was performed in a wider potential window (0.2–1.2 V vs RHE) corresponding to harsher conditions. TAL-2-900 turned out to be rather stable with a change in halfwave potential between the first and 5000th cycle being 20 mV. The chronoamperometric test was performed at 1.6 V vs RHE in 0.1 M KOH. RuO_2 gradually degraded down to 74% of its initial activity after 10000 seconds, while the TAL-2-900 activity remained virtually unchanged (99%) (Fig. 5F).

The only significant difference between the cobalt (TAL-2-900) and iron (TAL-1-900) catalysts was the fact that the cobalt materials performed much better in HER. The overpotential for TAL-2-900 was –308 mV at –10 mA cm^{-2}, while the one for Pt/C was –233 mV in 0.1 M KOH (Fig. 5G). In 1 M KOH electrolyte, the HER activity of TAL-2-900 improved to –264 mV vs RHE @–10 mA cm^{-2}, while the one for Pt/C was –57 mV (Fig. 5I).

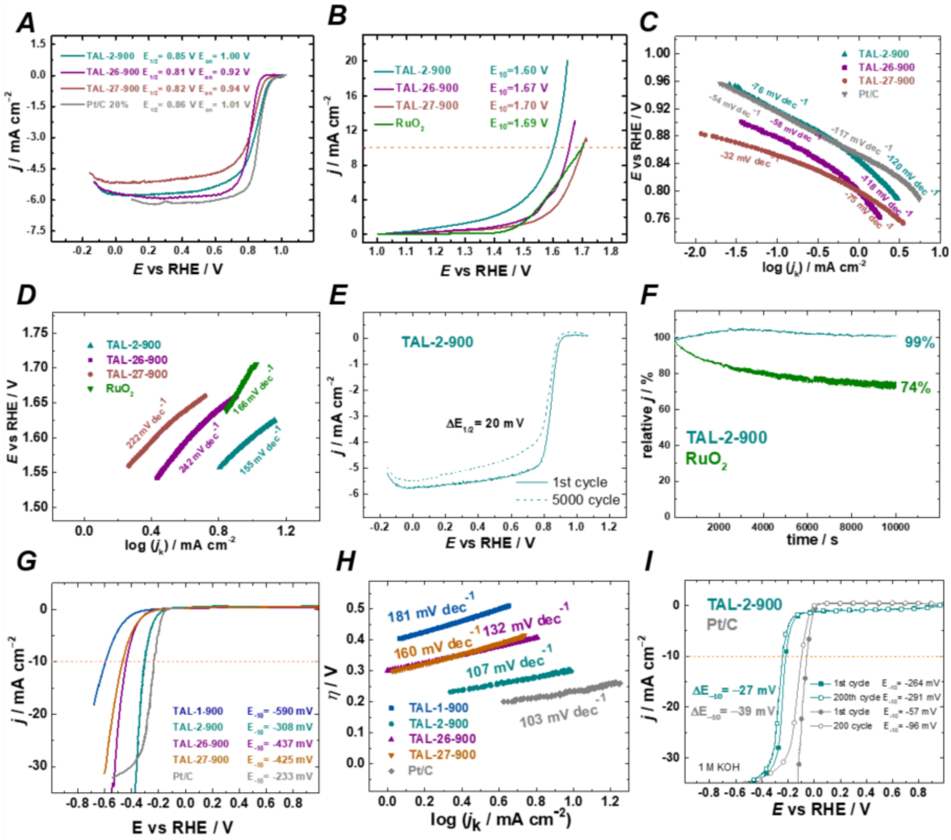

Figure 5. *Electrochemical characterization of cobalt based TAL electrocatalysts. (A) ORR and (B) OER polarization curves at 1600 rpm with scan rate of 10 mV s^{-1} in 0.1 M KOH. Tafel plots for (C) ORR and (D) OER. (E) ORR stability test for TAL-2-900 over 5000 cycles in the potential range 0.2–1.2 V. (F) Chronoamperometric measurements at 1.6 V for TAL-2-900. (G) HER polarization curves for TAL-1-900 and TAL-2-900, TAL-26-900 and TAL-27-900 in 0.1 M KOH. (H) Tafel plots for HER curves in 0.1 M KOH. (I) HER stability tests for TAL-2-900 and Pt/C in 1 M KOH.*

Additionally, TAL-2 was carbonized at different temperatures (800, 900 and 1000 °C) to gain more insight into the structure–activity relationships (Fig. 6A, B, and C). All of the three carbonized materials contained Co(0) nanoparticles, albeit, as observed by PXRD (Fig. 6D), there was less graphite and Co(0) in the sample prepared at 800 °C. Out of these series, TAL-2-900 was the best performing catalyst in all the transformations.

Rotating ring disc electrode (RRDE) was used to find out the percentage production of hydrogen peroxide (Fig. 6E). Production of H_2O_2 was in the range of 25–30% for all the catalyst (Fig. 6F). Altogether, TAL-2-900 showed promising results as a *trifunctional* electrocatalyst.

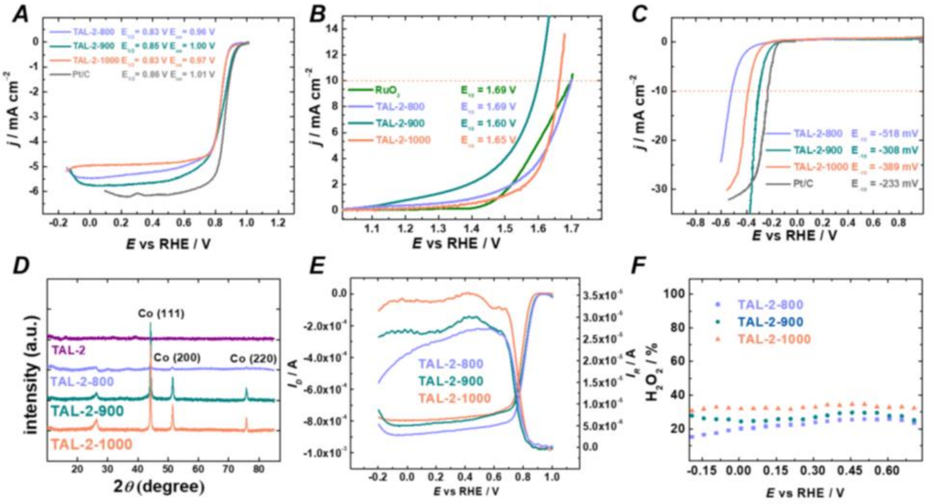

Figure 6. *Comparison of TAL-2 derived materials carbonized at different temperatures. (A) ORR (B) OER (C) HER polarization curves of TAL-2 derived materials carbonized at 800, 900 and 1000 °C at 1600 rpm with scan rate of 10 mV s^{-1} in 0.1 M KOH. (D) PXRD pattern of TAL-2 and TAL-2-800, 900, 1000. (E) RRDE curves for TAL-2-800, 900 and 1000. (F) H_2O_2 percentage production during RRDE measurements.*

To evaluate the real-life use of the best performing materials, TAL-1-900 and TAL-2-900 were applied in anion exchange membrane fuel cell as cathode materials. The mass loading was 2 mg cm^{-2} and HMT-PMBI was used as polymer hydroxide membrane [89]. TAL-2-900 exhibited higher power density (> 400 mW cm^{-2}) and current density (1100 mA cm^{-2}) and outperformed both Pt/C and TAL-1-900 (Fig. 7) Usually, while the benchmark for power density is considered as 1 W cm^{-2}[90], TAL-2-900 only reached the half of this target.

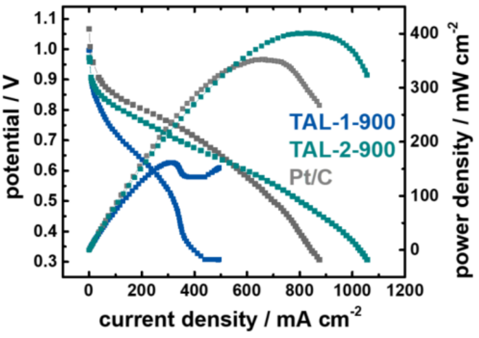

Figure 7. *Power density and polarization curves for H_2/O_2 single cell alkaline anion-exchange membrane fuel cell using TAL-1-900, TAL-2-900 and Pt/C (2 mg cm^{-2}) along with HMT-PMBI anion-exchange membrane. Pt-Ru/C (0.8 mg$_{Pt\text{-}Ru}$ cm^{-2}) was used as the anode. T = 60 °C*

In the iron and cobalt systems, we saw that the choice of the ligand (***TL1***–***TL3***) was important for the overall activity. Hence, I have screened an additional series of rationally designed ligands (***TL4***–***TL9***) recently developed within our group [91] (Table 3). Specifically, I used heterogenous catalysts developed only from the corresponding iron containing MOFs (Table 3) in ORR and OER (Fig. 8). Overall, the electrochemical data indicated that the diol moiety was essential for high efficiency. More studies are needed to understand the role of different substitution patterns in the benzimidazole core in the fabricated final catalysts.

Table 3. *Differentially substituted nitrogen ligands and final iron based catalyst materials used in this work.*

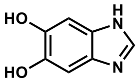
TL1

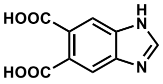
TL2

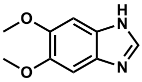
TL3

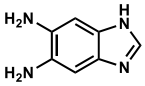
TL4

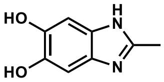
TL5

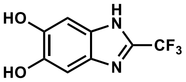
TL6

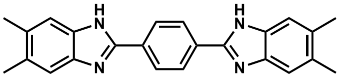
TL7

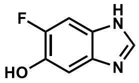
TL8

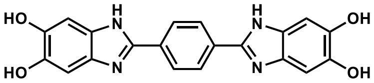
TL9

ligands	*catalyst material*
TL4	TAL-13-900
TL5	TAL-20-900
TL6	TAL-22-900
TL7	TAL-23-900
TL8	TAL-24-900
TL9	TAL-25-900

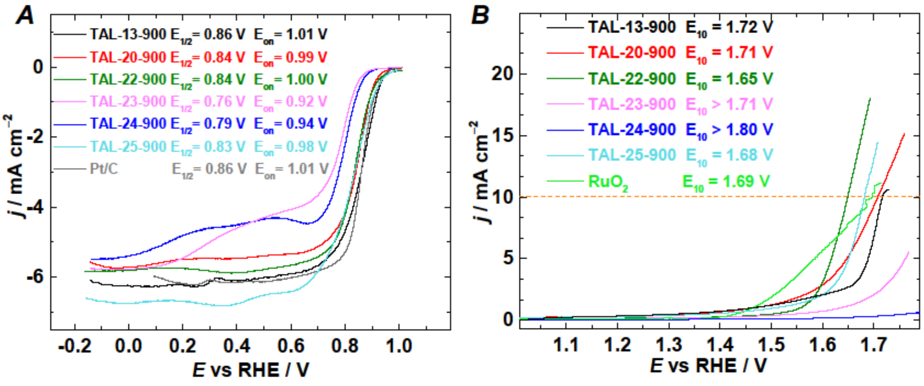

Figure 8. *Electrochemical screening of iron based materials derived from different ligands in (A) ORR and (B) OER. Polarization curves at 1600 rpm with scan rate of 10 mV s^{-1} in 0.1 M KOH.*

3 Multimetallic alloy nanomaterials

In the earlier sections of this PhD thesis, I have tested various single metal MNC materials. Often, however, employing metal various combinations can be advantageous, because this may give rise to synergistic effects, which can further enhance the stability of such materials in long-term operations [92]. In this chapter, I have focused on bi- and trimetallic MNC materials comprising of iron, cobalt and nickel.

Using two or more metals can lead to (1) new active sites containing dual metals [92], (2) mixed oxide nanoparticles or (3) mixed metal nanoalloys. The use of the diverse combinations of metals and, perhaps, ligands can provide different compositions and an increased number of active centers that may boost the intrisic activity of the electrocatalysts and, importantly, their durability [93,94]. Electrocatalysts comprising of different metals tend to give lower overpotentials for OER when compared to other combinations [96].

The majority of multimetallic materials explored so far are based mixed metal oxides [95–100]. MOFs have also been reported as precursors for metal/metal oxide composites [101]. Multimetallic 2D MOFs obtained from terephthalic acid were active in OER without a need for carbonization [102–104]. Li *et al.* also reported that the activity of CoFe OER catalysts was improved by doping them with Ni, V and Cr [99]. Most often, in such studies combinations of various metals are not compared.

With our optimized ligand ***TL1***, I surveyed a series of materials derived from a set of iron triad metals. Namely, I evaluated FeCo (TAL-18-900), CoNi (TAL-31-900), FeNi (TAL-32-900) and FeCoNi (TAL-36-900) containing materials (Fig. 9). The preparation of multimetallic electrocatalysts was similar to that of TAL-1-900 and TAL-2-900 and we were using MOFs obtained from equimolar amounts of the initial salts. The obtained MOFs were carbonized at 900 ^{o}C and etched with HNO_3.

STEM micrographs indicated the presence of metallic nanoparticles that are covered by the carbon onion-like shells (Fig. 10). All the materials were porous with pore sizes of 2–4 nm (Fig. 9C, D). The XPS data had confirmed that M–N_x and pyridinic nitrogen were the major nitrogen species in all of the samples (Fig. 9E).

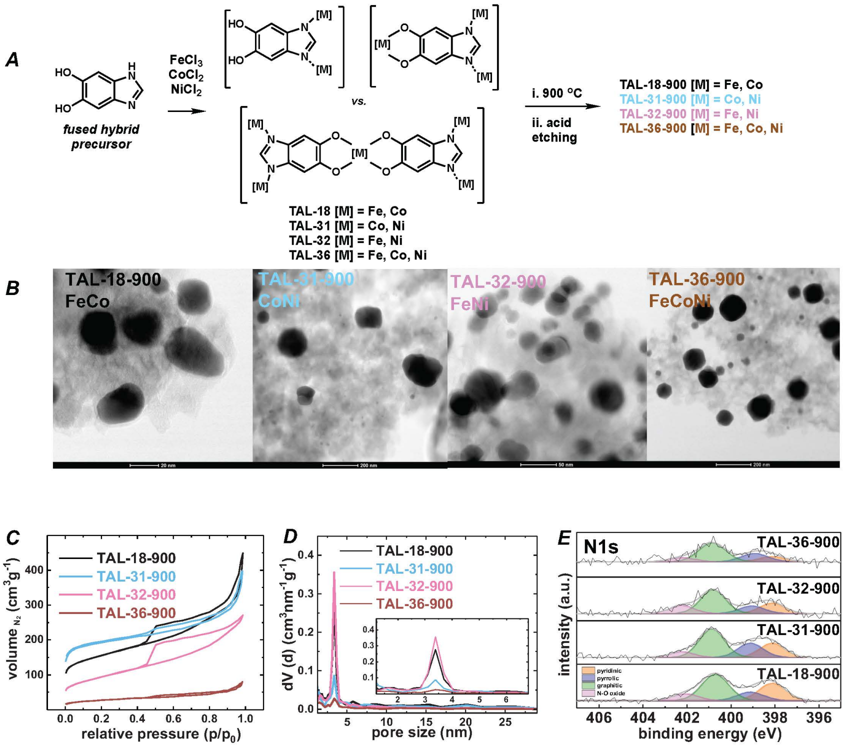

Figure 9. *(A) Scheme of preparation of multimetallic electrocatalysts, (B) STEM micrograph of different catalyst, (C) N_2 uptake isotherms, (D) pore size distribution and (E) XPS spectra for N1s region for all the electrocatalysts.*

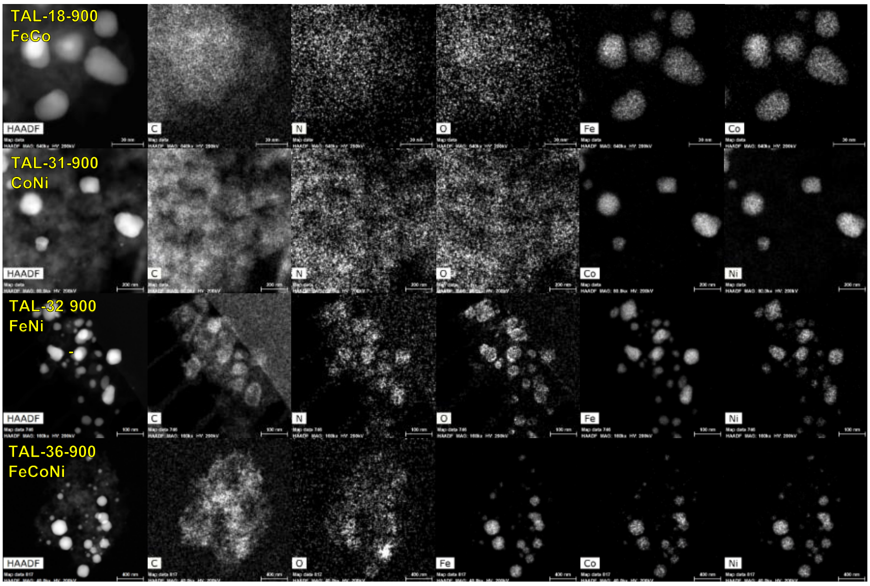

Figure 10. *Elemental mapping of different materials using HAADF–STEM.*

The electrocatalysts were tested under three conditions – ORR, OER and HER in 0.1 M KOH (Fig. 11 A). The materials showed comparable activity in the ORR and HER, and TAL-32-900 outperformed Pt/C under the ORR conditions. The higher activity may be associated with synergistic effect of iron and nickel metals in both the ORR and OER reactions. The lower values in the Tafel plots for ORR (Fig. 11B) indicated that the $4e^-$ mechanism was predominant, in which oxygen is reduced to water. In the OER, TAL-36-900 catalyst performed the best, and metal alloys that included nickel showed better performance. In HER, there was no significant difference in the activity among the materials.

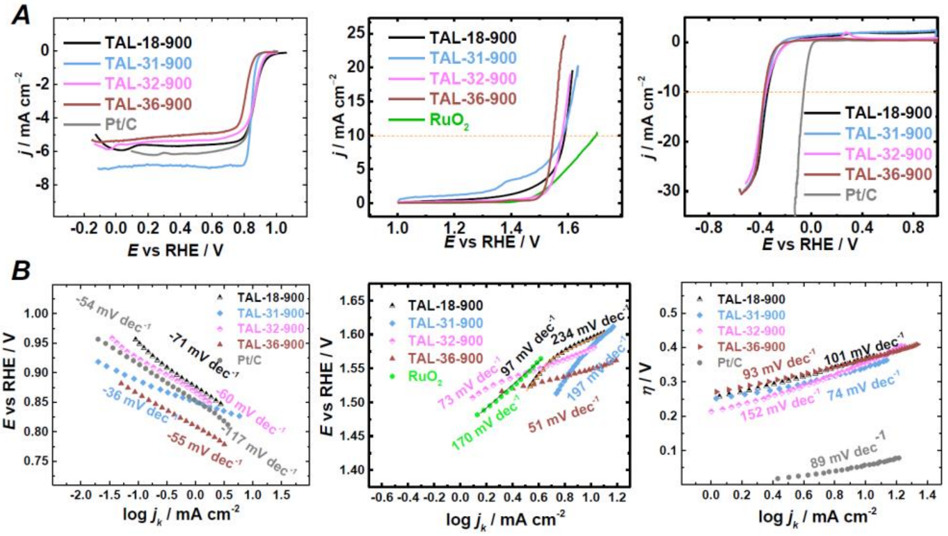

Figure 11. *(A) Electrochemical characterization of FeCoNi electrocatalyst in ORR, OER and HER in at 1600 rpm with scan rate of 10 mV* s^{-1} *in 0.1 M KOH, (B) Tafel plots for ORR, OER and HER.*

All the materials were less active than Pt/C in ORR and RuO_2 in OER when tested in acidic media (0.5 M H_2SO_4; Fig. 12A). Interestingly, TAL-18-900 performed better among other materials under all three conditions. Higher values of Tafel slopes in OER indicated fast deterioration of materials' performance (Fig. 12B). In HER, the overpotential values at –10 mA cm^{-2} were similar to that of Pt/C.

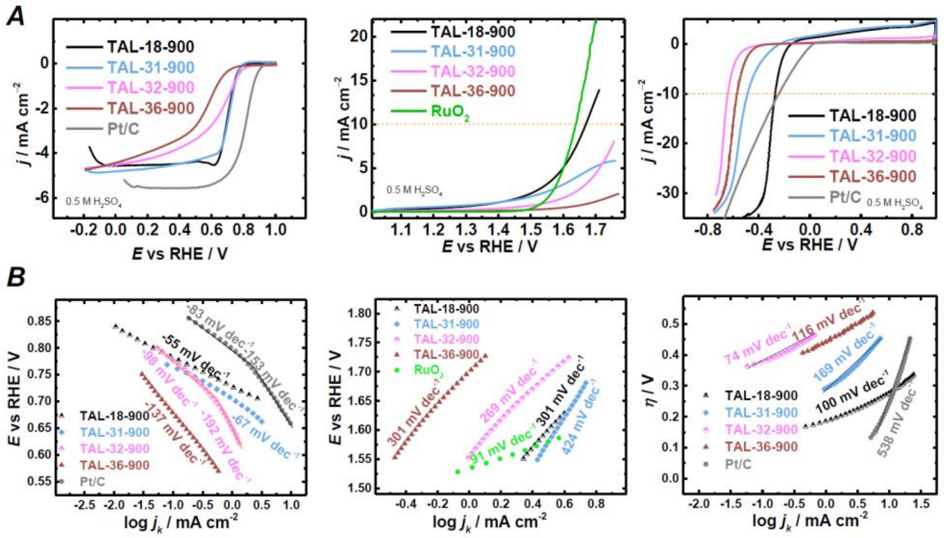

Figure 12. *(A) Electrochemical characterization of FeCoNi electrocatalyst in ORR, OER and HER in 0.5 M H_2SO_4 (B) Tafel plot for ORR, OER and HER, respectively.*

To access the stability of materials in alkaline media, more stringent cycling conditions were employed with a wider potential window (0.2–1.2 V for ORR and 1–1.8 V for OER) (Fig. 13). TAL-18-900 and TAL-31-900 were stable in ORR with shifts in halfway potential of 12 and 11 mV, respectively. TAL-32-900 and TAL-36-900, however, were more stable in OER with minor shifts in potential at 10 mA cm^{-2} (Fig. 13B). The negative shift in performance might be a result of loss of material from the surface of the electrode during long-term operation. In OER, the stability of TAL-31-900 (FeNi) and TAL-36-900 (FeCoNi) could be associated with formation of nickel hydroxide as the active species, which is protected by additional iron [105].

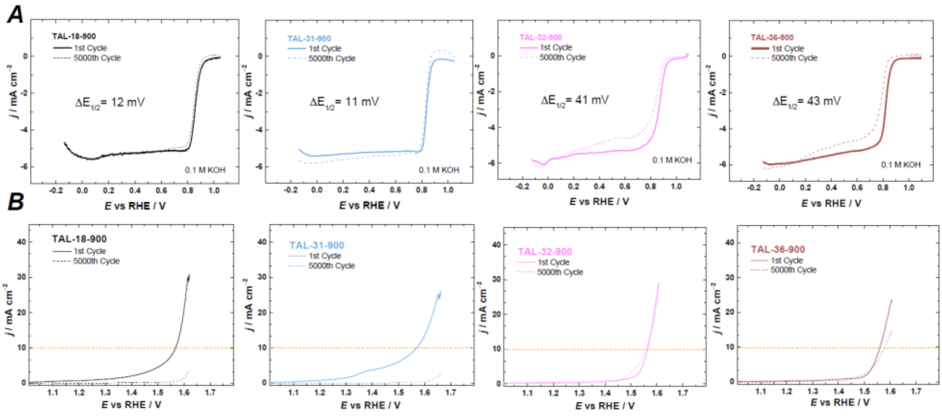

Figure 13. *Stability test of FeCoNi electrocatalysts in (A) ORR and (B) OER for 5000 cycles in 0.1 M KOH.*

In acidic media, stability test showed the same trend as was the case in alkaline medium in ORR (Fig. 14A). However, all the materials were not stable in OER in 0.5 M H_2SO_4 (Fig. 14B).

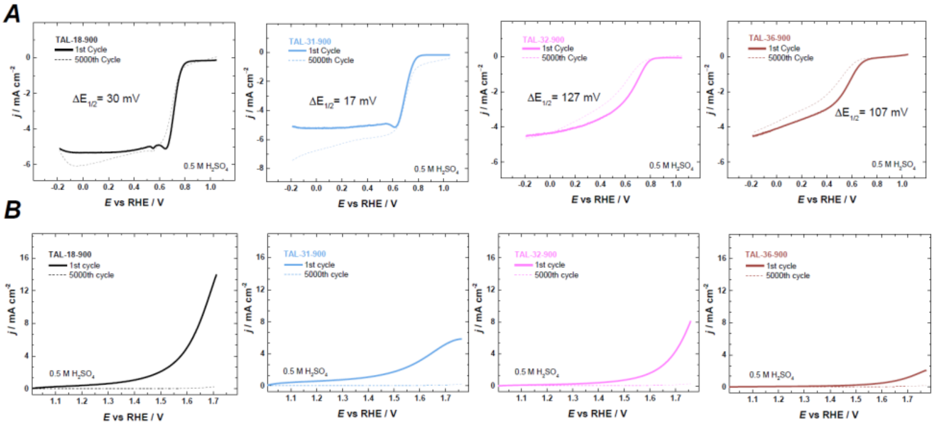

Figure 14. *Stability test of FeCoNi electrocatalysts in (A) ORR and (B) OER after 5000 cycles in 0.5 M* H_2SO_4*.*

All the catalysts were subjected to solid-state zinc–air battery (ZAB) tests. The cycling stability was demonstrated by using galvano charging/discharging up to 60000 s, and the persistence of ZABs was evaluated using standard CV tests (Fig. 15). They showed that TAL-18-900 was a better performing catalyst yielding 12 mW cm^{-2} as power density peak, which dropped significantly after the galvano charging/discharging performance (Fig. 15A). A similar trend was observed for TAL-31-900 with an exception that at the starting point of cycling the potential range was narrower (1.2–1.7 V), and the battery failed to retain the range (Fig. 15B).

TAL-32-900 and TAL-36-900 showed promising results in the *preliminary* solid-state battery tests, which have outperformed the commercial Pt-Ru/C battery in cycling (c.f. Fig. 15C, D, and E). The electopolarization curves of power density for TAL-32-900 before and after charging/discharging cycling confirmed its durability, while TAL-36-900 exhibited rather low current and power densities. Importantly, TAL-32-900 (FeNi) indicated excellent durability within a higher potential range (1–2 V) (Fig. 15C), whereas Pt-Ru/C (0.4–1.6 V) failed to retain the discharging potential over longer period of time (Fig. 15E).

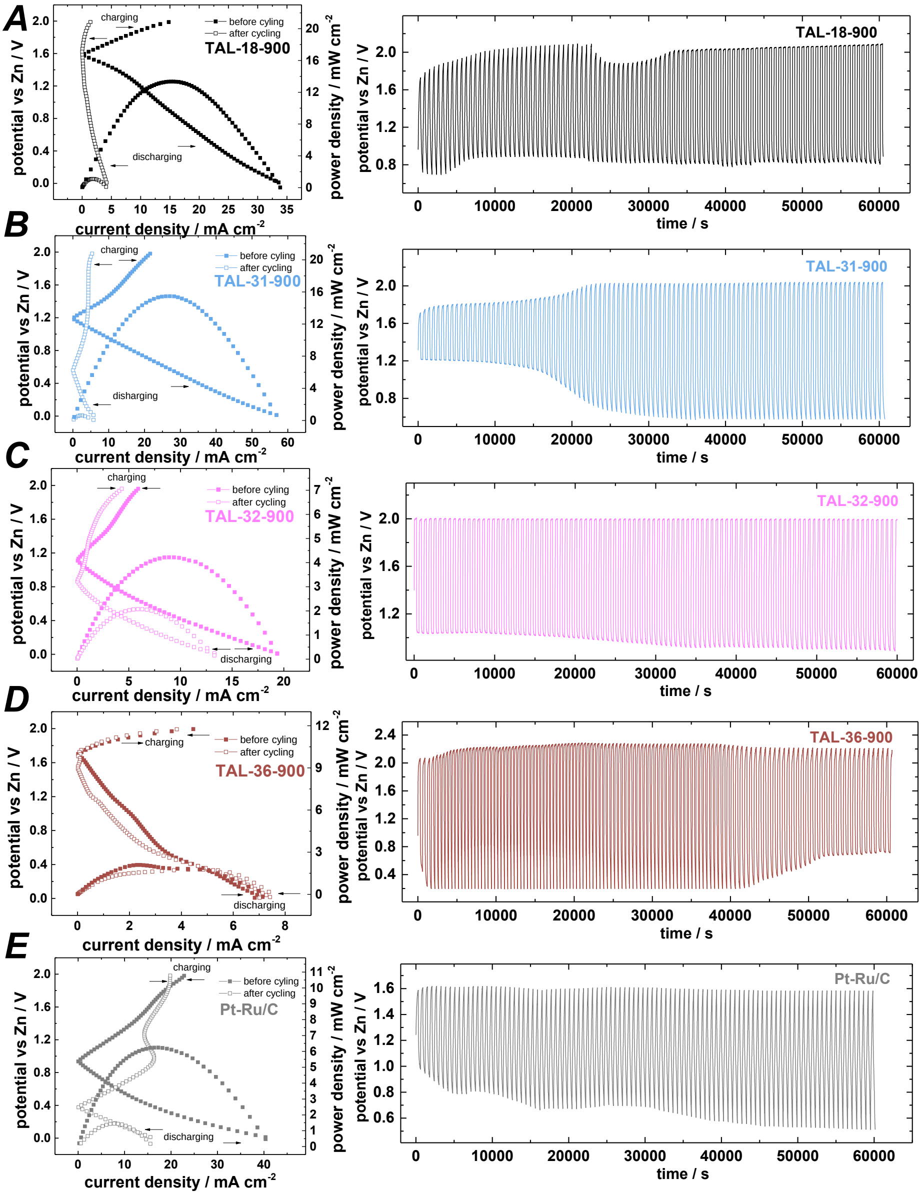

Figure 15. Zinc–air battery based electro polarization and power curves with respective charge/discharge cycling results for (A) TAL-18-900, (B) TAL-31-900, (C) TAL-32-900, (D) TAL-36-900 and (E) Pt-Ru/C.

4 Development of bismuth materials for electrochemical reduction of CO_2

It is well established that the anthropogenic activities, particularly CO_2 emisions, are caused by the excessive use of fossil fuels and that they have an overall negative impact on climate change. Within the framework of the UN Paris Agreement, it was decided to work together to keep the rise in average temperatures below two degrees (i.e. 2 °C) [1].

In the recent past, electrochemical reduction of carbon dioxide (CO_2RR) coupled with intermittent sources of energy supply (specifically, wind and solar sources) have emerged as a promising way to store and convert energy. By using appropriate electrocatalysts, CO_2 can be converted into higher value added products such as carbon monoxide (CO), formic acid (HCOOH), ethylene (C_2H_4) and higher hydrocarbons. However, it remains to be an outstanding challenge to produce products with high selectivity because of the similar thermodynamic potentials and the concurrence of hydrogen evolution reaction. These similar potentials for several products also give rise to various reaction intermediates that go on to form multiple products. Hence, the much sought after selective product formation will often depend on multiple variables such as the potential applied, the electrolytes, electrochemical reactor setup, membranes and the electrocatalysts used at hand. To date, there is a lack in high-durability protocols to compare electrocatalyst activities in the experimental research.

The majority of studies reported to date have focused on copper-based electrocatalysts to produce hydrocarbons [108]. In these cases, carbon monoxide often serves as an intermediate, which binds strongly to the metal sites to afford the overall progress to various CO_2RR products. Unfortunately, CO is often an effective metal poison and this concurrently leads to the overproduction of hydrogen. In contrast, use of other transition metal catalysts (especially, nickel and silver) reduce CO_2 conversion to CO, however, using them the multi-carbon products are produced at lower efficiencies [108].

In this work, we have tested our newly developed ligand in application towards the formation of a bismuth(0)-based MNC material for selective electrochemical reduction of CO_2 to formate.

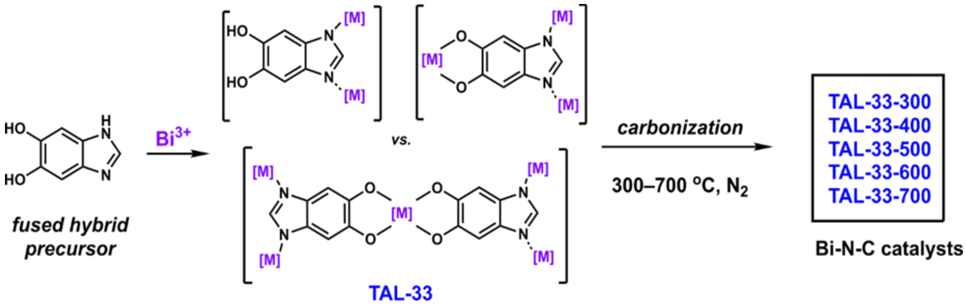

Figure 16. *Scheme of preparation of novel bismuth-metal based electrocatalysts*

The preparation of bismuth-based electrocatalysts was done by carbonizing polycrystalline bismuth metal–organic frameworks derived from 1*H*-benzo[*d*]imidazole-5,6-diol ligand (Fig. 16), whereby carbonization at various temperatures was tested. Flash pyrolysis was applied for two hours under inert atmosphere using dinitrogen and led to formation of materials with variable structural morphology and electrochemical activity. Altogether, five samples were assessed: TAL-33-300, TAL-33-400, TAL-33-500, TAL-33-600 and TAL-33-700. The XRD data demonstrated that the most active electrocatalysts were rich in amorphous carbon and metallic bismuth. Another interesting observation was that upon the increase in annealing temperatures, the concentration of metallic bismuth particles increased and, overall, had in resulted in better CO_2 reduction efficiencies (Fig. 17).

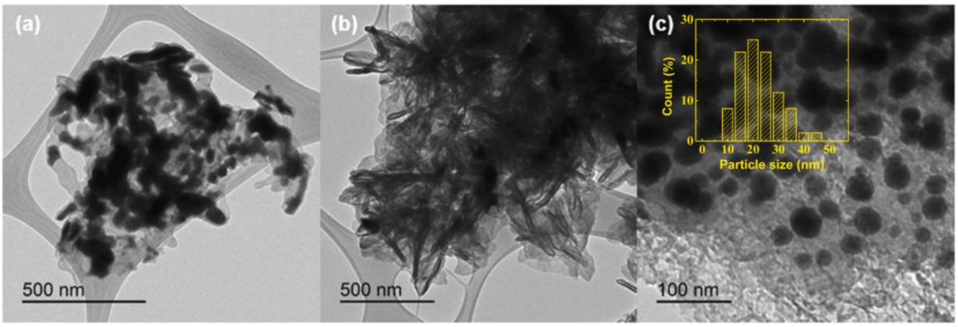

Figure 17. *TEM images of bismuth electrocatalysts (A) TAL-33-400, (B) TAL-33-500 and (C) TAL-33-600.*

Electrochemical characterization was done by characterizing the products formed in solution by performing cyclic voltammetry and chronoamperometry under CO_2RR conditions. The typical H-type cell was used with 0.45 M $KHCO_3$ and 0.5 M KCl solution saturated with CO_2 as catholyte at pH of 8.4 at 25 °C. The analyte was 1 M KOH separated by cation membrane activated in 0.1 M NaOH for 24 h. Under similar conditions, electrolyte CVs were measured to compare electrocatalytic performances across all of the samples (Fig. 18) in CO_2 and argon-saturated solutions. The electrocatalyst loading was kept constant at 1 mg cm^{-2}.

Out of all of the samples, only TAL-33-400, TAL-33-500 and TAL-33-600 displayed CO_2 electroreduction at –1.43 V vs AgCl/Cl. This suggests that there is a narrow window of carbonization conditions, which deliver active electrocatalysts.

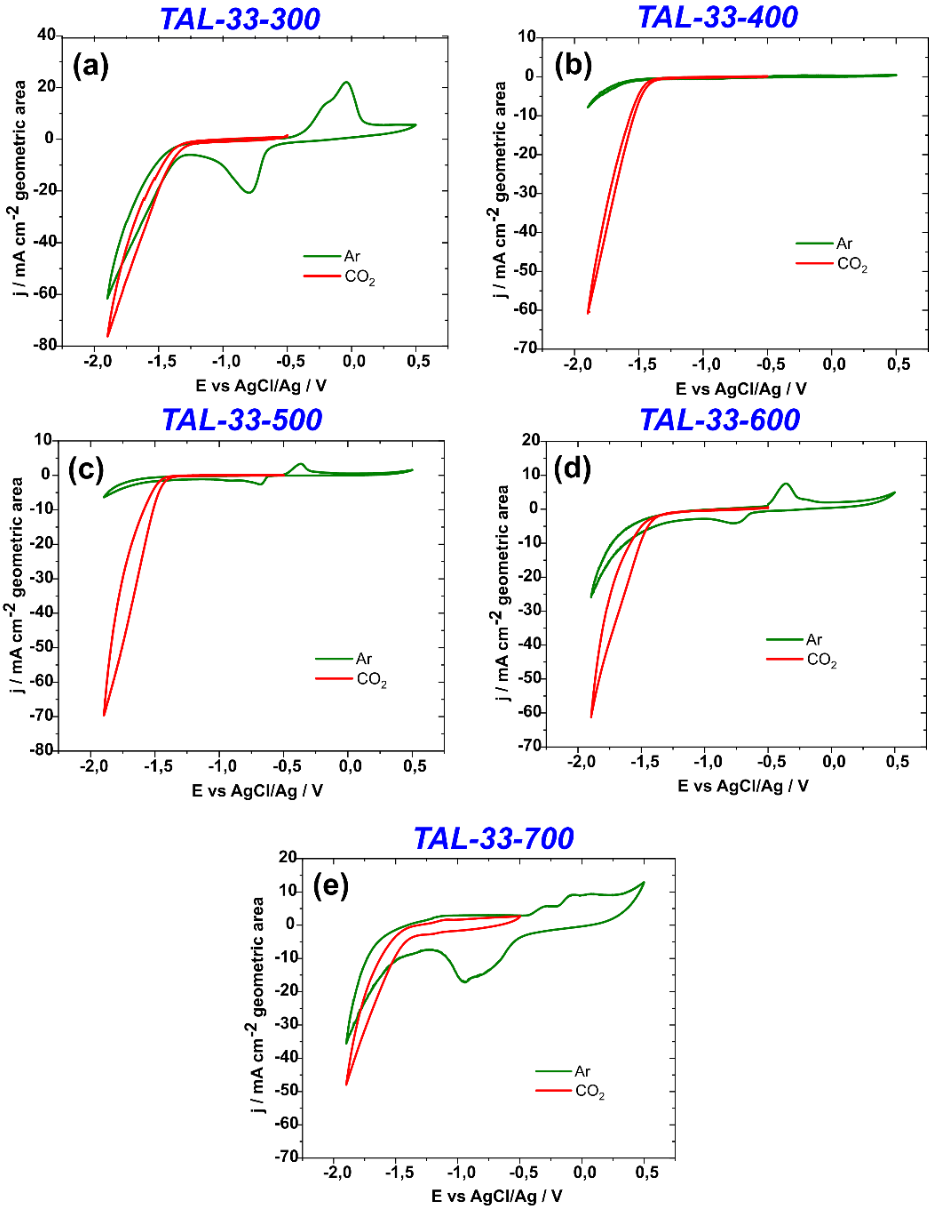

Figure 18. *Cyclic voltammetry in CO_2 and argon-saturated electrolyte (0.5 M KHO_3 and 0.5 M KCl), (A) TAL-33-300, (B) TAL-33-400, (C) TAL-33-500, (D) TAL-33-600 and (E) TAL-33-700.*

To elucidate the product selectivity and investigate catalyst stability, chronoamperometric measurements were performed using H-type cell at –1 V vs RHE for 1.5 h, subsequently for 4 h. The bismuth electrocatalysts carbonized at 400–600 °C exhibited higher selectivity towards formate formation. TAL-33-600 retained high Faradaic efficiency close to 100% for 1.5 h as compared to other catalyst materials.

After 1.5 h, TAL-33-400 efficiency started to drop off (Fig. 19). In contrary, the amount and the nature of the bismuth(0) nanoparticles present in TAL-33-600 ensured its continued performance.

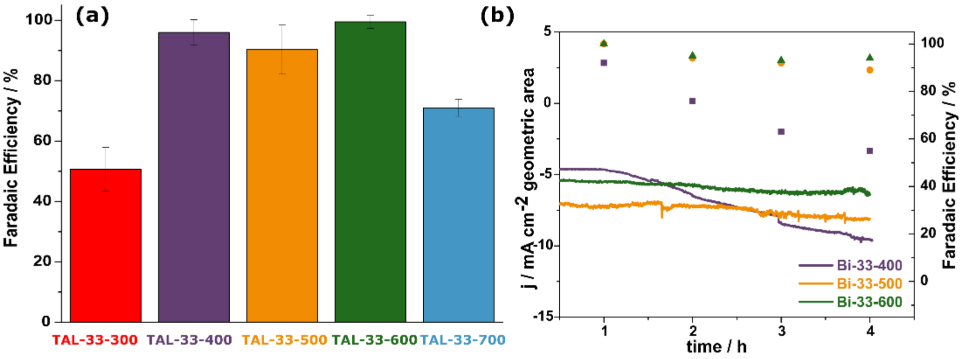

Figure 19. *(A) Faradaic efficiency of bismuth based electrocatalysts for 1.5 h at –1.0 V vs RHE, (B) Stability measurement at –1.0 V vs RHE for 4 h and their Faradaic efficiency.*

As is evident from the obtained electrochemical results, TAL-33-600 delivered the best activity along with the highest Faradaic efficiency and stability with just a minor loss of 6% over the span of 4 h. On this basis of these data, we conclude that the size and the number of Bi(0) nanoparticles formed at 600 °C is central in determining in the high electroactivity of the underlying catalyst. This points out that the interplay of the nitrogen-doped carbon network and the carbonization parameters are important in establishing the catalytically active Bi(0) nanoparticles.

Conclusions

In this PhD thesis, I have fabricated multifunctional MNC materials from polycrystalline and amorphous metal–organic frameworks, which are based on carbon rich benzimidazole linkers.

1. I have screened a family of catalysts based on iron and variously substituted benzimidazoles to identify 1*H*-benzo[*d*]imidazole-5,6-diol as the best performing and most cost-efficient ligand for iron-based materials fabrication used in ORR and OER.
2. With three selected ligands, I showed that a similar trend is valid in the cobalt based series in ORR, OER and HER.
3. I have developed multimetallic systems using various combinations of iron triad metals in ORR, OER, HER. Additionally, have proved that these novel catalysts can be applied as cathode materials in single fuel cell and zinc–air batteries.
4. I fabricated new MNC materials that contain nitrogen-doped carbon-supported Bi(0) nanoparticles for CO_2RR.

References

[1] The Paris Agreement. United Nations, Paris, **2015.**

[2] The European Green Deal. European Commission, Brussels, COM(2019) 640 final, **2019**.

[3] Varela, A. S.; Ju, W.; Strasser, P. Molecular nitrogen–carbon catalysts, solid metal organic framework catalysts, and solid metal/nitrogen-doped carbon (MNC) catalysts for the electrochemical CO_2 reduction. *Adv. Energy. Mater.* **2018,** *8,* 1703614.
DOI: 10.1002/aenm.201703614

[4] Minteer, S. D.; Christopher, P.; Linic, S. Recent developments in nitrogen reduction catalysts: A virtual issue. *ACS Energy Lett.* **2018,** 4, 163–166.
DOI: 10.1021/acsenergylett.8b02197

[5] Guo, X.; Du, H.; Qu, F.; Li, J. Recent progress in electrocatalytic nitrogen reduction. *J. Mater. Chem. A,* **2019,** 7, 3531–3543.
DOI: 10.1039/C8TA11201K

[6] Qing, G.; Ghazfar, R.; Jackowski, S. T.; Habibzadeh, F.; Ashtiani, M. M.; Chen, C. P.; Smith III, M. R.; Hamann, T. W. Recent advances and challenges of electrocatalytic N2 reduction to ammonia. *Chem. Rev.* **2020.** 120, 5437–5516.
DOI: 10.1021/acs.chemrev.9b00659

[7] Masa, J.; Andronescu, C.; Schuhmann, W. Electrocatalysis as the nexus for sustainable renewable energy: The gordian knot of activity, stability, and selectivity. *Angew. Chem., Int. Ed.* **2020**, *59*, 15298–15312.
DOI: 10.1002/anie.202007672

[8] Shi, Z.; Yang, W.; Gu, Y.; Liao, T.; Sun, Z. Metal-nitrogen-doped carbon materials as highly efficient catalysts: Progress and rational design. *Adv. Sci.* **2020,** 7, 2001069.
DOI: 10.1002/advs.202001069

[9] Pei, J.; Zhao, R.; Mu, X.; Wang, J.; Liu, C.; Zhang, X.-D. Single-atom nanozymes for biological applications. *Biomater. Sci.* **2020,** 8, 6428–6441.
DOI: 10.1039/D0BM01447H

[10] Masa, J.; Xia, W.; Muhler, M.; Schuhmann, W. On the role of metals in nitrogen-doped carbon electrocatalysts for oxygen reduction. *Angew. Chem., Int. Ed.* **2015,** 54, 10102–10120.
DOI: 10.1002/anie.201500569

[11] Wei, Y.-S.; Zhang, M.; Zou, R.; Xu, Q. Metal–organic framework-based catalysts with single metal sites. *Chem. Rev.* **2020,** 120, 12089–12174.
DOI: 10.1021/acs.chemrev.9b00757

[12] Deng, Y.; Xie, Y.; Zou, K.; Ji, X. Review on recent advances in nitrogen-doped carbons: Preparations and applications in supercapacitors. *J. Mater. Chem. A* **2016,** 4, 1144–1173.
DOI: 10.1039/C5TA08620E

[13] Huang, N.; Yang, L.; Zhang, M.; Yan, S.; Ding, Y.; Sun, P.; Sun, X. Cobalt-embedded N-doped carbon arrays derived in situ as trifunctional catalyst toward hydrogen and oxygen evolution, and oxygen reduction. *ChemElectroChem* **2019**, *6*, 4522–4532.
DOI:10.1002/celc.201901106

[14] Yang, Z.; Zhao, C.; Qu, Y.; Zhou, H.; Zhou, F.; Wang, J.; Wu, Y.; Li, Y. Trifunctional self-supporting cobalt-embedded carbon nanotube films for ORR, OER, and HER triggered by solid diffusion from bulk metal. *Adv. Mater.* **2019**, *31*, 1808043. DOI:10.1002/adma.201808043

[15] Liu, X.; Wang, Y.; Chen, L.; Chen, P. Jia, S.; Zhang, Y.; Zhou, S.; Zang, J. Co_2B and Co nanoparticles immobilized on the N–B-doped carbon derived from nano-B_4C for efficient catalysis of oxygen evolution, hydrogen evolution, and oxygen reduction reactions. *ACS Appl. Mater. Interfaces* **2018**, *10*, 37067–37078. DOI:10.1021/acsami.8b13359

[16] Shi, M.; Wang, J.-H.; Zhang, Y.; Zhang, X.-M. A rational design of efficient trifunctional electrocatalysts derived from tailored Co^{2+}-functionalized anionic metal–organic frameworks. *Dalton Trans.* **2020**, *49*, 2280–2289. DOI:10.1039/C9DT04930D

[17] Ge, H.; Li, G.; Shen, J.; Ma, W.; Meng, X.; Xu, L. Co_4N nanoparticles encapsulated in N-doped carbon box as tri-functional catalyst for Zn–air battery and overall water splitting. *Appl. Catal. B Environ.* **2020**, *275*, 119104. DOI:10.1016/j.apcatb.2020.119104

[18] Kong, F.; Fan, X.; Zhang, X.; Wang, L.; Kong, A.; Shan, Y. Soft-confinement conversion of Co-salen-organic-frameworks to uniform cobalt nanoparticles embedded within porous carbons as robust trifunctional electrocatalysts. *Carbon* **2019**, *149*, 471–482. DOI:10.1016/j.carbon.2019.04.079

[19] Ping, K., Alam, M., Kahnert, S.R., Bhadoria, R., Mere, A., Mikli, V., Käärik, M., Aruväli, J., Paiste, P., Kikas, A. and Kisand, V., Järving, I.; Leis, J.; Kongi, N.; Starkov, P. Multi-purpose heterogeneous catalyst material from an amorphous cobalt metal–organic framework. *Mater. Adv.* **2021,** *2,* 4009–4015. DOI: 10.1039/D1MA00414J

[20] Guo, H.; Feng, Q.; Zhu, J.; Xu, J.; Li, Q.; Liu, S.; Xu, K.; Zhang, C.; Liu, T. Cobalt nanoparticle-embedded nitrogen-doped carbon/carbon nanotube frameworks derived from a metal–organic framework for trifunctional ORR, OER and HER electrocatalysis. *J. Mater. Chem. A* **2019**, *7*, 3664–3672. DOI:10.1039/C8TA11400E

[21] Li, J.; Kang, Y.; Liu, D.; Lei, Z.; Liu, P. Nitrogen-doped graphitic carbon-supported ultrafine co nanoparticles as an efficient multifunctional electrocatalyst for HER and rechargeable Zn–air batteries. *ACS Appl. Mater. Interfaces* **2020**, *12*, 5717–5729. DOI:10.1021/acsami.9b18101

[22] Huang, Y.; Liu, Q.; Lv, J.; Babu, D. D. Wang, W.; Wu, M.; Yuan, D.; Wang, Y. Co-intercalation of multiple active units into graphene by pyrolysis of hydrogen-bonded precursors for zinc–air batteries and water splitting. *J. Mater. Chem. A* **2017**, *5*, 20882–20891. DOI:10.1039/C7TA06677E

[23] Zhang, X.; Liu, R.; Zang, Y.; Liu, G.; Wang, G.; Zhang, Y.; Zhang, H.; Zhao, H. Co/CoO nanoparticles immobilized on Co–N-doped carbon as trifunctional electrocatalysts for oxygen reduction, oxygen evolution and hydrogen evolution reactions. *Chem. Commun.* **2016**, *52*, 5946–5949. DOI:10.1039/C6CC02513G

[24] Li, H.; Li, Q.; Wen, P.; Williams, T. B.; Adhikari, S.; Dun, C.; Lu, C.; Itanze, D.; Jiang, L.; Carroll, D. L.; Donati, G. L.; Lundin, P. M.; Qiu, Y.; Geyer, S. M. Colloidal cobalt phosphide nanocrystals as trifunctional electrocatalysts for overall water splitting powered by a zinc–air battery. *Adv. Mater.* **2018**, *30*, 1705796. DOI:10.1002/adma.201705796

[25] Zou, W.; Dou, K.; Jiang, Q.; Xiang, J.; Kaun, C.-C.; Tang, H. Nearly spherical CoP nanoparticle/carbon nanosheet hybrids: A high-performance trifunctional electrocatalyst for oxygen reduction and water splitting. *RSC Adv.* **2019**, *9*, 39951–39957. DOI:10.1039/C9RA07334E

[26] Liu, H.; Guan, J.; Yang, S.; Yu, Y.; Shao, R.; Zhang, Z.; Dou, M.; Wang, F.; Xu, Q. Metal–organic framework-derived Co_2P nanoparticle/multi-doped porous carbon as a trifunctional electrocatalyst. *Adv. Mater.* **2020**, 2003649. DOI:10.1002/adma.202003649

[27] Shao, Q.; Li, Y.; Cui, X.; Li, T.; Wang, H.; Li, Y.; Duan, Q.; Si, Z. Metallophthalocyanine-based polymer-derived Co_2P nanoparticles anchoring on doped graphene as high-efficient trifunctional electrocatalyst for Zn–air batteries and water splitting. *ACS Sustain. Chem. Eng.* **2020**, *8*, 6422–6432. DOI:10.1021/acssuschemeng.0c00852

[28] Meng, T.; Hao, Y.-N.; Zheng, L.; Cao, M. Organophosphoric acid-derived CoP quantum dots@S,N-codoped graphite carbon as a trifunctional electrocatalyst for overall water splitting and Zn–air batteries. *Nanoscale* **2018**, *10*, 14613–14626. DOI:10.1039/C8NR03299H

[29] Guo, Y.; Yuan, P.; Zhang, J.; Xia, H.; Cheng, F.; Zhou, M.; Li, J.; Qiao, Y.; Mu, S.; Xu, Q. Co_2P–CoN double active centers confined in N-doped carbon nanotube: Heterostructural engineering for trifunctional catalysis toward HER, ORR, OER, and Zn–air batteries driven water splitting. *Adv. Funct. Mater.* **2018**, *28*, 1805641. DOI:10.1002/adfm.201805641

[30] Zhang, Y.-Q.; Tao, H.-B.; Chen, Z.; Li, M.; Sun, Y.-F.; Hua, B.; Luo, J.-L. In situ grown cobalt phosphide (CoP) on perovskite nanofibers as an optimized trifunctional electrocatalyst for Zn–air batteries and overall water splitting. *J. Mater. Chem. A* **2019**, *7*, 26607–26617. DOI:10.1039/C9TA08936E

[31] Gao, L.; Zhu, M.; Zhang, Z.; Cui, G. Cobalt-boron-oxide supported on N,P dual-doped carbon nanosheets as the trifunctional electrocatalyst and its application in rechargeable Zn–air battery and overall water-electrolysis. *Electrochim. Acta* **2019**, *327*, 134980. DOI:10.1016/j.electacta.2019.134980

[32] Li, Y.; Cao, R.; Li, L.; Tang, X.; Chu, T.; Huang, B.; Yuan, K.; Chen, Y. Simultaneously integrating single atomic cobalt sites and Co_9S_8 nanoparticles into hollow carbon nanotubes as trifunctional electrocatalysts for Zn–air batteries to drive water splitting. *Small* **2020**, *16*, 1906735. DOI:10.1002/smll.201906735

[33] Wang, N.; Li, L.; Zhao, D.; Kang, X.; Tang, Z.; Chen, S. Graphene composites with cobalt sulfide: Efficient trifunctional electrocatalysts for oxygen reversible catalysis and hydrogen production in the same electrolyte. *Small* **2017**, *13*, 1701025. DOI:10.1002/smll.201701025

[34] Meng, T.; Qin, J.; Wang, S.; Zhao, D.; Mao, B.; Cao, M. *In situ* coupling of $Co_{0.85}Se$ and N-doped carbon via one-step selenization of metal–organic frameworks as a trifunctional catalyst for overall water splitting and Zn–air batteries. *J. Mater. Chem. A* **2017**, *5*, 7001–7014. DOI:10.1039/C7TA01453H

[35] Lyu, D.; Du, Y.; Huang, S.; Mollamahale, B. Y.; Zhang, X.; Hasan, S. W.; Yu, F.; Wang, S.; Tian, Z. Q.; Shen, P. K. Highly efficient multifunctional Co–N–C electrocatalysts with synergistic effects of Co–N moieties and Co metallic nanoparticles encapsulated in a N-doped carbon matrix for water-splitting and oxygen redox reactions. *ACS Appl. Mater. Interfaces* **2019**, *11*, 39809–39819. DOI:10.1021/acsami.9b11870

[36] Pei, Z.; Tang, Z.; Liu, Z.; Huang, Y.; Wang, Y.; Li, H.; Xue, Q.; Zhu, M.; Tang, D.; Zhi, C. Construction of a hierarchical 3D Co/N-carbon electrocatalyst for efficient oxygen reduction and overall water splitting. *J. Mater. Chem. A* **2018**, *6*, 489–497. DOI:10.1039/C7TA09254G

[37] Zhou, Z.; He, F.; Shen, Y.; Chen, X.; Yang, Y.; Liu, S.; Mori, T.; Zhang, Y. Coupling multiphase-Fe and hierarchical N-doped graphitic carbon as trifunctional electrocatalysts by supramolecular preorganization of precursors. *Chem. Commun.* **2017**, *53*, 2044–2047. DOI:10.1039/C6CC09442B

[38] Qin, Q.; Jang, H.; Li, P.; Yuan, B.; Liu, X.; Cho, J. A tannic acid–derived N,P-codoped carbon-supported iron-based nanocomposite as an advanced trifunctional electrocatalyst for the overall water splitting cells and zinc–air batteries. *Adv. Energy Mater.* **2019**, *9*, 1803312. DOI:10.1002/aenm.201803312

[39] Yang, J.; Wang, X.; Li, B.; Ma, L.; Shi, L.; Xiong, Y.; Xu, H. Novel iron/cobalt-containing polypyrrole hydrogel-derived trifunctional electrocatalyst for self-powered overall water splitting. *Adv. Funct. Mater.* **2017**, *27*, 1606497. DOI:10.1002/adfm.201606497

[40] Kong, F.; Fan, X.; Kong, A.; Zhou, Z.; Zhang, X.; Shan, Y. Covalent phenanthroline framework derived FeS@Fe_3C composite nanoparticles embedding in N-S-codoped carbons as highly efficient trifunctional electrocatalysts. *Adv. Funct. Mater.* **2018**, *28*, 1803973. DOI:10.1002/adfm.201803973

[41] Devi, B.; Koner, R. R.; Halder, A. Ni(II)-dimeric complex-derived nitrogen-doped graphitized carbon-encapsulated nickel nanoparticles: Efficient trifunctional electrocatalyst for oxygen reduction reaction, oxygen evolution reaction, and hydrogen evolution reaction. *ACS Sustain. Chem. Eng.* **2019**, *7*, 2187–2199. DOI:10.1021/acssuschemeng.8b04883

[42] Diao, J.; Qiu, Y.; Liu, S.; Wang, W.; Chen, K.; Li, H.; Yuan, W.; Qu, Y.; Guo, X. Interfacial engineering of W_2N/WC heterostructures derived from solid-state synthesis: A highly efficient trifunctional electrocatalyst for ORR, OER, and HER. *Adv. Mater.* **2020**, *32*, 1905679. DOI:10.1002/adma.201905679

[43] Peng, X.; Zhao, S.; Mi, Y.; Han, L.; Liu, X; Qi, D.; Sun, J.; Liu, Y.; Bao, H.; Zhuo, L.; Xin, H. L.; Luo, J.; Sun, X. Trifunctional single-atomic Ru sites enable efficient overall water splitting and oxygen reduction in acidic media. *Small* **2020**, 2002888. DOI:10.1002/smll.202002888

[44] Tang, C.; Zhong, L.; Zhang, B.; Wang, H.-F.; Zhang, Q. 3D mesoporous van der waals heterostructures for trifunctional energy electrocatalysis. *Adv. Mater.* **2018**, *30*, 1705110.
DOI:10.1002/adma.201705110

[45] He, L.; Liu, J.; Hu, B. ; Liu, Y.; Cui, B.; Peng, D.; Zhang, Z.; Wu, S.; Liu, B. Cobalt oxide doped with titanium dioxide and embedded with carbon nanotubes and graphene-like nanosheets for efficient trifunctional electrocatalyst of hydrogen evolution, oxygen reduction, and oxygen evolution reaction. *J. Power Sources* **2019**, *414*, 333–344.
DOI:10.1016/j.jpowsour.2019.01.020

[46] Alshehri, S. M.; Alhabarah, A. N.; Ahmed, J.; Naushad, M.; Ahamad, T. An efficient and cost-effective tri-functional electrocatalyst based on cobalt ferrite embedded nitrogen doped carbon. *J. Colloid Interface Sci.* **2018**, *514*, 1–9.
DOI:10.1016/j.jcis.2017.12.020

[47] Kwak, I.; Kwon, I. S.; Kim, J.; Park, K.; Ahn, J.-P.; Yoo, S. J.; Kim, J.-G.; Park, J. IrO_2–ZnO hybrid nanoparticles as highly efficient trifunctional electrocatalysts. *J. Phys. Chem. C* **2017**, *121*, 14899–14906.
DOI:10.1021/acs.jpcc.7b03844

[48] Deng, C.; Wu, K.-H.; Scott, J.; Zhu, S.; Zheng, X.; Amal, R.; Wang, D.-W. Spherical Murray-type assembly of Co–N–C nanoparticles as a high-performance trifunctional electrocatalyst. *ACS Appl. Mater. Interfaces* **2019**, *11*, 9925–9933.
DOI:10.1021/acsami.8b20565

[49] Li, K.; Guo, D.; Kang, J.; Wei, B.; Zhang, X.; Chen, Y. Hierarchical hollow spheres assembled with ultrathin CoMn double hydroxide nanosheets as trifunctional electrocatalyst for overall water splitting and Zn air battery. *ACS Sustain. Chem. Eng.* **2018**, *6*, 14641–14651.
DOI:10.1021/acssuschemeng.8b03232

[50] Sun, T.; Zhang, S.; Xu, L.; Wang, D.; Li, Y. An efficient multifunctional hybrid electrocatalyst: Ni_2P nanoparticles on MOF-derived Co,N-doped porous carbon polyhedrons for oxygen reduction and water splitting. *Chem. Commun.* **2018**, *54*, 12101–12104.
DOI:10.1039/C8CC06566G

[51] Surendran, S.; Shanmugapriya, S.; Sivanantham, A.; Shanmugam, S.; Selvan, R. K. Electrospun carbon nanofibers encapsulated with nicop: a multifunctional electrode for supercapattery and oxygen reduction, oxygen evolution, and hydrogen evolution reactions. *Adv. Energy Mater.* **2018**, *8*, 1800555.
DOI:10.1002/aenm.201800555

[52] Ren, J.-T.; Chen, L.; Wang, Y.-S.; Tian, W.-W.; Gao, L.-J.; Yuan, Z.-Y. FeNi nanoalloys encapsulated in N-doped CNTs tangled with N-doped carbon nanosheets as efficient multifunctional catalysts for overall water splitting and rechargeable Zn–air batteries. *ACS Sustain. Chem. Eng.* **2020**, *8*, 223–237.
DOI:10.1021/acssuschemeng.9b05238

[53] Bian, Y. ; Wang, H.; Gao, Z.; Hu, J.; Liu, D.; Dai, L. A facile approach to high-performance trifunctional electrocatalysts by substrate-enhanced electroless deposition of Pt/NiO/Ni on carbon nanotubes. *Nanoscale* **2020**, *12*, 14615–14625.
DOI:10.1039/D0NR03378B

[54] Lv, X.; Tian, W.; Liu, Y.; Yuan, Z.-Y. Well-defined CoP/Ni_2P nanohybrids encapsulated in a nitrogen-doped carbon matrix as advanced multifunctional electrocatalysts for efficient overall water splitting and zinc–air batteries. *Mater. Chem. Front.* **2019**, *3*, 2428–2436. DOI:10.1039/C9QM00449A

[55] Bai, Z.; Li, S.; Fu, J.; Zhang, Q.; Chang, F.; Yang, L.; Lu, J.; Chen, Z. Metal-organic framework-derived nickel cobalt oxysulfide nanocages as trifunctional electrocatalysts for high efficiency power to hydrogen. *Nano Energy* **2019**, *58*, 680–686. DOI:10.1016/j.nanoen.2019.01.050

[56] Shi, Q.; Liu, Q.; Ma, Y.; Fang, Z.; Liang, Z.; Shao, G.; Tang, B.; Yang, W.; Qin, L.; Fang, X. high-performance trifunctional electrocatalysts based on FeCo/Co_2P hybrid nanoparticles for zinc–air battery and self-powered overall water splitting. *Adv. Energy Mater.* **2020**, *10*, 1903854. DOI:10.1002/aenm.201903854

[57] Zhang, W.; Zhao, J.; Zhang, J.; Chen, X.; Zhang, X.; Yang, F. Electronic asymmetric distribution of RhCu bimetallic nanocrystals for enhancing trifunctional electrocatalysis. *ACS Appl. Mater. Interfaces* **2020**, *12*, 10299–10306. DOI:10.1021/acsami.9b19980

[58] Bai, J.; Meng, T.; Guo, D.; Wang, S.; Mao, B.; Cao, M. Co_9S_8@MoS_2 core–shell heterostructures as trifunctional electrocatalysts for overall water splitting and zn–air batteries. *ACS Appl. Mater. Interfaces* **2018**, *10*, 1678–1689. DOI:10.1021/acsami.7b14997

[59] Prabhakaran, S.; Balamurugan, J.; Kim, N. H.; Lee, J. H. Hierarchical 3D oxygenated cobalt molybdenum selenide nanosheets as robust trifunctional catalyst for water splitting and zinc–air batteries. *Small* **2020**, *16*, 2000797. DOI:10.1002/smll.202000797

[60] Zhang, W.; Zhao, X.; Zhao, Y.; Zhang, J.; Li, X.; Fang, L.; Li, L. Mo-doped Zn, Co zeolitic imidazolate framework-derived Co_9S_8 quantum dots and MoS_2 embedded in three-dimensional nitrogen-doped carbon nanoflake arrays as an efficient trifunctional electrocatalysts for the oxygen reduction reaction, oxygen evolution reaction, and hydrogen evolution reaction. *ACS Appl. Mater. Interfaces* **2020**, *12*, 10280–10290. DOI:10.1021/acsami.9b19193

[61] Kong, F.; Zhang, C.; Qiao, Y.; Li, R.; Kong, A.; Shan, Y. Coupled nanocomposite $Co_{5.47}N$–Co_3Fe_7 inlaid in a tremella-like carbon framework as a highly efficient multifunctional electrocatalyst for oxygen transformation and overall water splitting. *Sustain. Energy Fuels* **2019**, *3*, 3538–3549. DOI:10.1039/C9SE00657E

[62] Sun, H.; Li, Q.; Lian, Y.; Zhang, C.; Qi, P.; Mu, Q.; Jin, H.; Zhang, B.; Chen, M.; Deng, Z.; Peng, Y. Highly efficient water splitting driven by zinc–air batteries with a single catalyst incorporating rich active species. *Appl. Catal. B Environ.* **2020**, *263*, 118139. DOI:10.1016/j.apcatb.2019.118139

[63] Yang, C. C.; Zai, S. F.; Zhou, Y. T.; Du, L.; Jiang, Q. Fe_3C–Co nanoparticles encapsulated in a hierarchical structure of N-doped carbon as a multifunctional electrocatalyst for ORR, OER, and HER. *Adv. Funct. Mater.* **2019**, *29,* 1901949. DOI:10.1002/adfm.201901949

[64] Hu, C.; Dai, L. Multifunctional carbon-based metal-free electrocatalysts for simultaneous oxygen reduction, oxygen evolution, and hydrogen evolution. *Adv. Mater.* **2017**, *29*, 1604942.
DOI:10.1002/adma.201604942

[65] Hu, Q.; Li, G.; Li, G.; Liu, X.; Zhu, B.; Chai, X.; Zhang, Q.; Liu, J.; He, C. Trifunctional electrocatalysis on dual-doped graphene nanorings–integrated boxes for efficient water splitting and Zn–air batteries. *Adv. Energy Mater.* **2019**, *9*, 1803867.
DOI:10.1002/aenm.201803867

[66] Jia, Y.; Zhang, L.; Du, A.; Gao, G.; Chen, J.; Yan, X.; Brown, C. L.; Yao, X. Defect graphene as a trifunctional catalyst for electrochemical reactions. *Adv. Mater.* **2016**, *28*, 9532.
DOI:10.1002/adma.201602912

[67] Jiang, H.; Gu, J.; Zheng, X.; Liu, M.; Qiu, X.; Wang, L.; Li, W.; Chen, Z.; Ji, X.; Li, J. Defect-rich and ultrathin N doped carbon nanosheets as advanced trifunctional metal-free electrocatalysts for the ORR, OER and HER. *Energy Environ. Sci.* **2019**, *12*, 322–333.
DOI:10.1039/C8EE03276A

[68] Chen, Y. Z.; Zhang, R.; Jiao, L.; Jiang, H. L. Metal–organic framework-derived porous materials for catalysis. *Coord. Chem. Rev.* **2018**, *362*, 1–23.
DOI: 10.1016/j.ccr.2018.02.008

[69] Hsueh, H. Y.; Yao, C. T.; Ho, R. M. Well-ordered nanohybrids and nanoporous materials from gyroid block copolymer templates. *Chem. Soc. Rev.* **2015,** *44,* 1974–2018.
DOI:10.1039/C4CS00424H

[70] Zhao, C.; Dai, X.; Yao, T.; Chen, W.; Wang, X.; Wang, J.; Yang, J.; Wei, S.; Wu, Y.; Li, Y. Ionic exchange of metal–organic frameworks to access single nickel sites for efficient electroreduction of CO_2. *J. Am. Chem. Soc.* **2017,** *139,* 8078–8081.
DOI:10.1021/jacs.7b02736

[71] Varela, A.S.; Ju, W.; Strasser, P. Molecular nitrogen-carbon catalysts, solid metal organic framework catalysts, and solid metal/nitrogen-doped carbon (MNC) catalysts for the electrochemical CO_2 reduction. *Adv. Energy Mater.* **2018,** *8,* 1703614.
DOI:10.1002/aenm.201703614

[72] Hu, X. M.; Hval, H. H.; Bjerglund, E. T.; Dalgaard, K. J.; Madsen, M. R.; Pohl, M. M.; Welter, E.; Lamagni, P.; Buhl, K. B.; Bremholm, M.; Beller, M. Selective CO_2 reduction to CO in water using earth-abundant metal and nitrogen-doped carbon electrocatalysts. *ACS Catal*. **2018,** *8,* 6255–6264.
DOI:10.1021/acscatal.8b01022

[73] Leonard, N.; Ju, W.; Sinev, I.; Steinberg, J.; Luo, F.; Varela, A.S.; Cuenya, B.R.; Strasser, P.; The chemical identity, state and structure of catalytically active centers during the electrochemical CO_2 reduction on porous Fe–nitrogen–carbon (Fe–N–C) materials. *Chem. Sci.* **2018,** *9,* 5064–5073.
DOI:10.1039/C8SC00491A

[74] Gomes, V.G.; Kornienko, N. Metal-based nanomaterials for efficient CO_2 electroreduction: Recent advances in mechanism, material design and selectivity. *Nano Energy* **2020,** *78,* 105311.
DOI:10.1016/j.nanoen.2020.105311

[75] Hori, Y.; Murata, A.; Takahashi, R. Formation of hydrocarbons in the electrochemical reduction of carbon dioxide at a copper electrode in aqueous solution. *J. Chem. Soc. Faraday Trans. I* **1989**, *85,* 2309–2326.
DOI:10.1039/F19898502309

[76] Lu, X. F.; Xia, B. Y.; Zang, S. Q.; Lou, X. W. Metal–organic frameworks based electrocatalysts for the oxygen reduction reaction. *Angew. Chem., Int. Ed.* **2020,** *132,* 4662-4678.
DOI:10.1002/anie.201910309

[77] Chung, H. T.; Cullen, D. A.; Higgins, D.; Sneed, B. T.; Holby, E. F.; More, K. L.; Zelenay, P. Direct atomic-level insight into the active sites of a high-performance PGM-free ORR catalyst. *Science* **2017,** *357,* 479–484.
DOI:10.1126/science.aan2255

[78] Shen, C.; Jie, S.; Chen, H.; Liu, Z. The Co-NC catalyst synthesized with a hard-template and etching method to achieve well-dispersed active sites for ethylbenzene oxidation. *Front. Chem.* **2019,** *7,* 426.
DOI:10.3389/fchem.2019.00426

[79] Meng, Z.; Cai, S.; Wang, R.; Tang, H.; Song, S.; Tsiakaras, P. Bimetallic–organic framework-derived hierarchically porous Co-Zn-NC as efficient catalyst for acidic oxygen reduction reaction. *Appl. Catal. B*. **2019,** *244,* 120–127.
DOI:10.1016/j.apcatb.2018.11.037

[80] Ping, K.; Alam, M.; Käärik, M.; Leis, J.; Kongi, N.; Järving, I.; Starkov, P. Surveying iron–organic framework TAL-1-derived materials in ligandless heterogeneous oxidative catalytic transformations of alkylarenes. *Synlett* **2019,** *30,* 1536–1540.
DOI:10.1055/s-0037-1611877

[81] Baumann, A. E.; Burns, D.A.; Liu, B.; Thoi, V. S. Metal-organic framework functionalization and design strategies for advanced electrochemical energy storage devices*. Commun. Chem.* **2019**, *2,* 86.
DOI:10.1038/s42004-019-0184-6

[82] Sun, L.; Hendon, C.H.; Park, S. S.; Tulchinsky, Y.; Wan, R.; Wang, F.; Walsh, A.; Dincă, M. Is iron unique in promoting electrical conductivity in MOFs? *Chem. Sci*. **2017**, *8,* 4450–4457.
DOI:10.1039/C7SC00647K

[83] Stolar, T.; Užarević, K. Mechanochemistry: an efficient and versatile toolbox for synthesis, transformation, and functionalization of porous metal–organic frameworks. *CrystEngComm*. **2020,** *2,* 4511-4525.
DOI:10.1039/D0CE00091D

[84] Yang, M.; Zhou, Z. Recent breakthroughs in supercapacitors boosted by nitrogen-rich porous carbon materials. *Adv. Sci.* **2017,** *4,* 1600408.
DOI:10.1002/advs.201600408

[85] Kong, L.; Zhu, J.; Shuang, W.; Bu, X. H. Nitrogen-doped wrinkled carbon foils derived from MOF nanosheets for superior sodium storage. *Adv. Energy Mater.* **2018,** *8,* 1801515.
DOI:10.1002/aenm.201801515

[86] Liu, C.; Li, F.; Ma, L. P.; Cheng, H. M. Advanced materials for energy storage. *Adv. Mater.* **2010,** *22,* E28–E62.
DOI:10.1002/adma.200903328

[87] Nitta, N.; Wu, F.; Lee, J. T.; Yushin, G.; Li-ion battery materials: Present and future. *Mater. Today* **2015**, *18,* 252–264.
DOI:10.1016/j.mattod.2014.10.040

[88] Ping, K.; Braschinsky, A.; Alam, M.; Bhadoria, R.; Mikli, V.; Mere, A.; Aruväli, J.; Paiste, P.; Vlassov, S.; Kook, M.; Rähn, M.; Sammelselg, V.; Tammeveski, K.; Kongi, N.; Starkov, P. Fused hybrid linkers for metal–organic framework-derived bifunctional oxygen electrocatalysts. *ACS Appl. Energy Mater.* **2019,** *3,* 152–157.
DOI:10.1021/acsaem.9b02039

[89] Wright, A. G.; Fan, J.; Britton, B.; Weissbach, T.; Lee, H. F.; Kitching, E. A.; Peckham, T. J.; Holdcroft, S. Hexamethyl-*p*-terphenyl poly(benzimidazolium): A universal hydroxide-conducting polymer for energy conversion devices. *Energy Environ. Sci.* **2016,** *9,* 2130–2142.
DOI:10.1039/C6EE00656F

[90] Wang, Y.; Yang, Y.; Jia, S.; Wang, X.; Lyu, K.; Peng, Y.; Zheng, H.; Wei, X.; Ren, H.; Xiao, L.; Wang, J. Synergistic Mn-Co catalyst outperforms Pt on high-rate oxygen reduction for alkaline polymer electrolyte fuel cells. *Nat. Commun.* **2019.** *10,* 1–8.
DOI:10.1038/s41467-019-09503-4

[91] Ping, K. Rational design of carbonaceous MOF-based materials for chemo- and electrocatalytic applications. PhD thesis, Tallinn University of Technology, **2021.**
DOI:10.23658/taltech.21/2021

[92] Wang, J.; Huang, Z.; Liu, W.; Chang, C.; Tang, H.; Li, Z.; Chen, W.; Jia, C.; Yao, T.; Wei, S.; Wu, Y.; Li, Y. Design of N-coordinated dual-metal sites: A stable and active Pt-free catalyst for acidic oxygen reduction reaction. *J. Am. Chem. Soc.* **2017,** *139,* 17281–17284.
DOI:10.1021/jacs.7b10385

[93] Baumann, A. E.; Burns, D. A.; Liu, B.; Thoi, V. S. Metal-organic framework functionalization and design strategies for advanced electrochemical energy storage devices. *Commun. Chem.* **2019,** *2,* 1–14.
DOI:10.1038/s42004-019-0184-6

[94] Chen, L.; Zhang, Y.; Dong, L.; Yang, W.; Liu, X.; Long, L.; Liu, C.; Dong, S.; Jia, J. Synergistic effect between atomically dispersed Fe and Co metal sites for enhanced oxygen reduction reaction. *J. Mater. Chem. A* **2020,** *8,* 4369–4375.
DOI:10.1039/C9TA12516G

[95] Zhang, Y.; Kizilkaya, O.; Bilan, H. K.; Kurtz, R.; Podlaha, E. J. Activity and regeneration of electrodeposited Fe–Ni–Co-Based electrocatalysts for the alkaline oxygen evolution reaction. *ACS Appl. Energy Mater.* **2020,** *3,* 7239–7245.
DOI:10.1021/acsaem.0c00985

[96] Smith, R.D.; Prévot, M. S.; Fagan, R. D.; Trudel, S.; Berlinguette, C. P. Water oxidation catalysis: Electrocatalytic response to metal stoichiometry in amorphous metal oxide films containing iron, cobalt, and nickel. *J. Am. Chem. Soc.* **2013,** *135,* 11580–11586.
DOI:10.1021/ja403102j

[97] McCrory, C. C.; Jung, S.; Ferrer, I. M.; Chatman, S. M.; Peters, J. C.; Jaramillo, T. F. Benchmarking hydrogen evolving reaction and oxygen evolving reaction electrocatalysts for solar water splitting devices. *J. Am. Chem. Soc.* **2015,** *137,* 4347–4357.
DOI:10.1021/ja510442p

[98] Moysiadou, A.; Hu, X. Stability profiles of transition metal oxides in the oxygen evolution reaction in alkaline medium. *J. Mater. Chem. A* **2019,** *7,* 25865–25877. DOI: 10.1039/c9ta10308b

[99] Li, S.; Zhou, X.; Fang, G.; Xie, G.; Liu, X.; Lin, X.; Qiu, H. J. Multicomponent spinel metal oxide nanocomposites as high-performance bifunctional catalysts in Zn–air batteries. *ACS Appl. Energy Mater.* **2020,** *3,* 7710–7718. DOI:10.1021/acsaem.0c01121

[100] Ibraheem, S.; Chen, S.; Li, J.; Wang, Q.; Wei, Z. In situ growth of vertically aligned FeCoOOH-nanosheets/nanoflowers on Fe,N co-doped 3D-porous carbon as efficient bifunctional electrocatalysts for rechargeable zinc–O_2 batteries. *J. Mater. Chem. A* **2019,** *7,* 9497–9502. DOI:10.1039/C9TA01964B

[101] Ren, D.; Ying, J.; Xiao, M.; Deng, Y. P.; Ou, J.; Zhu, J.; Liu, G.; Pei, Y.; Li, S.; Jauhar, A. M.; Jin, H. Hierarchically porous multimetal-based carbon nanorod hybrid as an efficient oxygen catalyst for rechargeable zinc–air batteries. *Adv. Funct. Mater.* **2020,** *30,* 1908167. DOI:10.1002/adfm.201908167

[102] Xu, J.; Zhu, X.; Jia, X. From low-to high-crystallinity bimetal–organic framework nanosheet with highly exposed boundaries: An efficient and stable electrocatalyst for oxygen evolution reaction. *ACS Sustain. Chem. Eng.* **2019,** *7,* 16629–16639. DOI:10.1021/acssuschemeng.9b03952

[103] Rui, K.; Zhao, G.; Chen, Y.; Lin, Y.; Zhou, Q.; Chen, J.; Zhu, J.; Sun, W.; Huang, W.; Dou, S. X. Hybrid 2D dual metal–organic frameworks for enhanced water oxidation catalysis. *Adv. Funct. Mater.* **2018,** *28,* 1801554. DOI:10.1002/adfm.201801554

[104] Zhao, S.; Wang, Y.; Dong, J.; He, C. T.; Yin, H.; An, P.; Zhao, K.; Zhang, X.; Gao, C.; Zhang, L.; Lv, J. Ultrathin metal–organic framework nanosheets for electrocatalytic oxygen evolution. *Nat. Energy* **2016,** *1,* 1–10. DOI:10.1038/nenergy.2016.184

[105] Zhou, Y.; López, N. The role of Fe species on NiOOH in oxygen evolution reactions. *ACS Catal.* **2020,** *10,* 6254–6261. DOI:10.1021/acscatal.0c00304

[106] Yusibova, G.; Alam, M.; Ping, K.; Sild, S.; Vlassov, S.; Šmits, K.; Aruväli, J.; Käärik, M.; Leis, J.; Starkov, P.; Maran, U.; Kongi, N. Computationally rationalizing post-treatment of multifunctional cobalt-based heterogeneous materials for oxygen reduction/evolution reactions. *Manuscript in prep.*

[107] Ávila-Bolívar, B.; Cepitis R.; Alam, M.; Assafrei J.-M.; Ping, K.; Aruväli, J.; Kikas, A.; Kisand, V.; Vlassov, S.; Ivaništštev, V.; Starkov, P.; Montiel, V.; Solla-Gullón, J.; Kongi, N. CO_2 reduction to formate on an affordable bismuth metal-organic framework based catalyst. *J. CO_2 Util.* **2022,** *59,* 101937. DOI:10.1016/j.jcou.2022.101937

[108] Nitopi, S.; Bertheussen, E.; Scott, S. B.; Liu, X.; Engstfeld, A. K.; Horch, S.; Seger, B.; Stephens, I. F. L.; Chan, K.; Hahn, C.; Nørskov, J. K.; Jaramillo, T. F.; Chorkendorff, I. Progress and perspectives of electrochemical CO_2 reduction on copper in aqueous electrolyte. *Chem. Rev.* **2019,** *119,* 7610–7672. DOI:10.1021/acs.chemrev.8b00705

Acknowledgements

I would like to thank my supervisors Dr Pavel Starkov and Professor Nadezda Kongi for their valuable guidance and enthusiastic support during this research work.

I would also like to thank my research colleagues Kefeng Ping , Rohit Bhadoria, Parth Singh and other lab members for their support during my PhD work.

I would also like to thank all the members at Department of Chemistry and Biotechnology at Tallinn University of Technology, the Institute of Chemistry at the University of Tartu, the Institute of Electrochemistry at the University of Alicante and Department of Chemistry at Technical University Darmstadt.

I am deeply grateful to my family members for their constant encouragement, blessings, and support throughout my research work.

Funding from the Estonian Research Council (PUT1290 and PSG250), Tallinn University of Technology (B62 and SSGF22007), Environmental Investment Center (KIK18070) and the Graduate School of Biomedicine and Biotechnology (#ASTRA 2014-2020.4.01.16-032) is acknowledged.

Abstract

Fabrication of novel metal, nitrogen co-doped carbon materials based on a unique organic ligand

The nexus of electrochemical processes is the use of heterogenous electrocatalyst materials. They can and should be tailored with a high level of control and precision to broaden their use.

To meet higher green energy demands, many groups are working on new building blocks used to fabricate metal, nitrogen-doped carbon (MNC) materials by using different metal sources, heteroatoms and carbon supports. Less expensive transitions metals (e.g. Fe, Co, Ni) provide a good alternative to platinum group metals. Their use has the potential to bring down the costs in manufacturing; however, for them to be applicable at a large scale, more work needs to be done to reduce catalyst loadings. So far, metal–organic frameworks (MOFs) used to produce MNC materials lacked novelty and largely relied on 2-methylimidazole as the nitrogen ligand. Alternatively, one has to rely on complexation with 1,10-phenanthroline as organic ligand. Although, upon carbonization, these catalysts were shown to be effective in several applications, their non-modularity had prevented finetuning the electrocatalyst materials. To address the increased needs for energy conversion and energy storage devices, the focus should shift to the stability of MNC materials.

In this doctoral thesis, I developed and optimized several new electrocatalyst materials. All of them are based on a novel family of benzimidazole linkers with 1*H*-benzo[*d*]imidazole-5,6-diol identified as an alternative to 1,10-phenanthroline and 2-methylimidazole.

The novel materials were derived from polycrystalline and amorphous metal–organic frameworks, which contained various non-platinum group metals such iron, cobalt and nickel for various applications including (1) oxygen reduction reaction (ORR), (2) oxygen evolution reaction (OER), (3) hydrogen evolution reaction (HER) and (4) carbon dioxide reduction reaction (CO_2RR). In addition, multimetallic systems based on iron triad metals were screened. Using the best performing materials, I have fabricated single fuel cells and zinc–air batteries. These studies emphasize the use of rationally designed organic linkers in electrocatalysis and the potential of the new family of ligands in energy conversion and storage devices.

Chapter 1 gives a short overview of MNC materials used for the electrochemical conversions of small molecules (CO_2, H_2O, N_2, O_2). Chapter 2 focuses on novel iron and cobalt based electrocatalysts used in electrochemical reactions such as ORR, OER and HER. In Chapter 3, I introduce and electrochemically evaluate multimetallic materials developed on the basis of combinations of various iron triad metals (Fe, Co, Ni), which were prepared using 1*H*-benzo[*d*]imidazole-5,6-diol as an alternative organic ligand. In Chapter 4, the same linker used to fabricate optimized MNC materials that incorporate Bi(0) nanoparticles for their use in electrochemical reduction of CO_2 to formate.

Lühikokkuvõte

Uue orgaanilise ligandi kasutuselevõtt metalli ja lämmastikuga rikastatud süsinikmaterjalide sünteesimiseks

Efektiivsetel elektrokeemilistel reaktsioonidel on suur roll uute rohetehnoloogia protsesside arendamisel. Sealjuures on reaktsiooni keskmeks heterogeensed süsinikmaterjalid, mida nimetatakse elektrokatalüsaatoriteks. Üle maailma panustatakse hetkel nende uurimisse selleks, et tuvastada ja optimeerida metalli ja lämmastikuga rikastatud süsinikmaterjale (MNC materjale), kasutades erinevaid metalle, heteroaatomeid ja süsinikukandjaid. Ideaalis oleks odavamate ja keskkonnasõbralike siirdemetallide (nt raud, koobalt, nikkel) kasutuselevõtt kuluefektiivseks lahenduseks kasutatavatele plaatinarühma metallidele.

MNC materjalide arendamisel ja tootmisel kasutatakse laialdaselt lähteainetena metall–orgaanilisi võrestikke (MOFe), kuid paljudel juhtudel on neid vaja rikastada teiste komponentidega. Selle töö raames arendasime uut tüüpi orgaanilist ligandi, mis võimaldab rikastada MOFe juba varastel fabritseerimisstaadiumitel. Uued elektrokatalüsaatorid põhinevad süsinikrikka bensimidasooli derivaatidele. Neist kõige mitmekülgsemaks ja efektiivsemaks osutus 1*H*-benso[*d*]imidasool-5,6-diool, mis on osutunud väga heaks alternatiiviks 1,10-fenantroliinile ja 2-metüülimidasoolile.

Materjale sünteesiti moodustades metall-orgaanilisi võrestikke, kusjuures ei olnud vahet kas on tegemist polükristalliliste või amorfsete materjalidega. Lisaks ühemetallilistele variantidele oleme näidanud, et on võimalik samaaegselt inkorporeerida ka mitmesuguseid mitteplaatina rühma metalle. Lõppmaterjale testiti elektrokatalüsaatoritena mitmesugustes protsessides, sealhulgas hapniku redutseerimisreaktsioonis (ORR), hapniku eraldumisreaktsioonis, vesiniku eraldumisreaktsioonis (HER) ja süsinikdioksiidi redutseerimisreaktsioonis (CO2RR). Optimeeritud materjale testiti ka kütuseelementides ja tsink–õhk akudes. Antud uurimistöö näitas, et elektrienergia muundamise ja salvestamise jaoks MNC materjalide omadusi saab täiustada, kasutades uusi ratsionaalselt väljaarendatud orgaanilisi ligande.

Esimeses peatükis antakse ülevaade MNC materjalidest, mida kasutatakse väikeste molekulide (CO_2, H_2O, N_2, O_2) elektrokeemilistes muundamistes. Teine peatükk keskendub uudsetele raua- ja koobaltipõhistele katalüsaatoritele, mida rakendati elektrokeemiliste reaktsioonide näitel (ORR, OER ja HER). Kolmandas peatükis tutvustatakse ja võrreldakse materjale, mida valmistati erinevate raudtriaadi metallide ehk raua, koobalti ja nikli segudest kasutades 1*H*-benso[*d*]imidasool-5,6-diooli orgaanilise ligandina. Neljandas peatükis rakendatakse sama ligandi selleks, et optimeerida MNC materjale, mis sisaldavad metallilise vismuti erisuuruses nanoosakesi erinevates kogustes. Neid optimeeritud materjale kasutati süsinikdioksiidi elektrokeemilisel redutseerimisel formiaadiks.

Appendix

Publication I

Ping, K.; Brashinsky, A.; Alam, M.; Bhadoria, R.; Mihkli, V.; Mere, A.; Vlassov, S.; Kook, M.; Rähn, M.; Sammelselg, V.; Aruväli, J.; Tammeveski, K.; Kongi, N.; Starkov, P.

Fused hybrid linkers for metal–organic framework-derived bifunctional oxygen electrocatalysts.

ACS Appl. Energy Mater. **2020**, *3*, 152–157.

DOI:10.1021/acsaem.9b02039

ACS APPLIED ENERGY MATERIALS
Letter
Cite This: ACS Appl. Energy Mater. 2020, 3, 152−157
www.acsaem.org

Fused Hybrid Linkers for Metal−Organic Framework-Derived Bifunctional Oxygen Electrocatalysts

Kefeng Ping,[†] Alan Braschinsky,[‡,#] Mahboob Alam,[†] Rohit Bhadoria,[†] Valdek Mikli,[§] Arvo Mere,[§] Jaan Aruväli,[‖] Päärn Paiste,[‖] Sergei Vlassov,[⊥] Mati Kook,[⊥] Mihkel Rähn,[⊥] Väino Sammelselg,[‡,⊥] Kaido Tammeveski,[‡] Nadežda Kongi,[*,‡] and Pavel Starkov[*,†]

[†]Department of Chemistry and Biotechnology, Tallinn University of Technology, Tallinn 12618, Estonia
[‡]Institute of Chemistry, University of Tartu, Tartu 50411, Estonia
[§]Department of Materials and Environmental Technology, Tallinn University of Technology, Tallinn 19086, Estonia
[‖]Institute of Ecology and Earth Sciences, University of Tartu, Tartu 50411, Estonia
[⊥]Institute of Physics, University of Tartu, Tartu 50411, Estonia

Supporting Information

ABSTRACT: Preparation of electrocatalysts often relies on the use of multiple starting materials, with examples arising from a single precursor being less common. We have surveyed a series of heterobivalent scaffolds to identify an iron/benzimidazole-based metal−organic framework as a uniform starting material. By merging the catechol and imidazole units together, we get a direct entry into a highly efficient bifunctional oxygen electrocatalyst, which alleviates the need for dopants and modifying conditions. We demonstrate that by fine-tuning the chemical nature of an organic linker, one is able to modulate the electrochemical properties of a single precursor-derived electrocatalyst material.

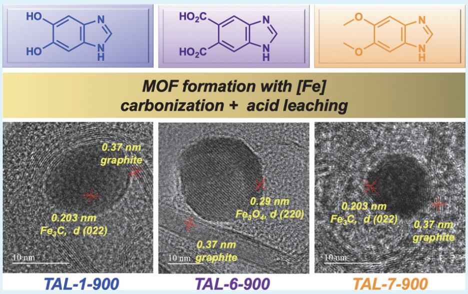

KEYWORDS: *bifunctional electrocatalyst, iron, oxygen reduction reaction, oxygen evolution reaction, renewable energy*

Metal−organic frameworks (MOFs) are a great platform for designing and building novel materials with a foray into applications in energy storage and conversion, e.g., water splitting, fuel cells, and metal−air batteries.[1] MOFs incorporate both the metal centers and organic ligands, which serve as essential building blocks.[2] Hence, having an intrinsic ability to modify their combinations may lead to more efficient, modular electrocatalyst materials. The oxygen reduction reaction (ORR) electrocatalysts have been exemplary with different MOFs having been traditionally employed as carbon-scaffolds and nitrogen-rich sources.[1] However, they often necessitate using dopants to raise the overall performance of the underlying electrocatalyst.[1] To date, only a few MOF-derived materials were shown to serve as highly efficient electrocatalysts for ORR (Figure 1). Among them are iron-based MIL-88B-NH$_2$,[3] cobalt-based ZIF-67,[4] and bimetallic systems based on MET-6[5] and hexaiminobenzene.[6]

In the ORR domain, the use of organic constituents for fabrication of earth-abundant-metal-based electrocatalyst materials (M−N−C) dates back[10,11] to the report of the first M−N−C catalyst, cobalt phthalocyanine (Figure 1A).[12] Since then, a number of complementary metal complexes (e.g., phthalocyanines,[12−14] porphyrins,[15] phenanthrolines,[16−18] and ferrocene[19]) have been examined. Recent work indicated that conductive MOFs such as $M_3(HITP)_2$[7,20] and $M_3(HHTP)_2$[20,21] may also serve as potential ORR catalysts. While such systems show low intrinsic activity, they have been used to demonstrate that organic constituents can participate in the electrochemical O_2 reduction through complementary ligand-centric mechanisms (Figure 1B).[7]

Herein, we introduce a new family of carbon-rich[22] benzimidazole-based MOF precursors, which are equipped with additional functional groups to modulate their electronic and ligating properties (Figure 1C). We assess them as ORR and oxygen evolution reaction (OER)[23] catalyst materials to identify that monocatechol/imidazole fused hybrid **1** is the best performing ligand for fabricating effective bifunctional oxygen (ORR/OER, ΔE = 0.73 V in 0.1 M KOH) electrocatalyst from an iron MOF-derived single-component precursor.

We envisaged building an Fe−N−C catalyst from a single MOF precursor by using designer ligands. While one would typically rely on multidirectional, symmetric structures based on porphyrins, phthalocyanines, and hexasubstituted tripheny-

Received: October 15, 2019
Accepted: December 18, 2019
Published: December 18, 2019

DOI: 10.1021/acsaem.9b02039
ACS Appl. Energy Mater. 2020, 3, 152−157

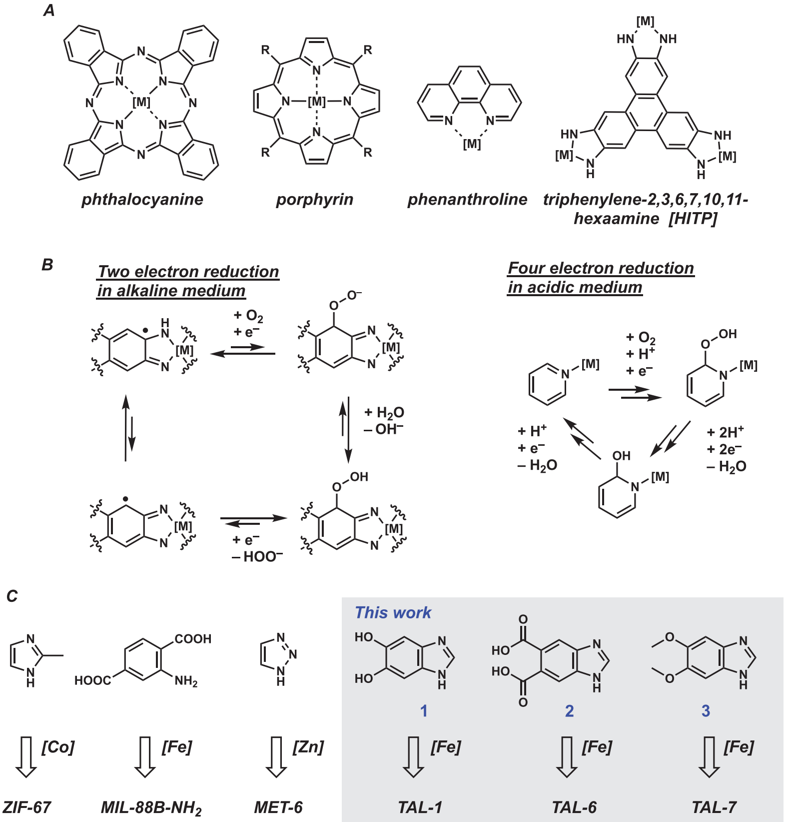

Figure 1. (A) Organic ligands complexed to a metal (M), widely used to prepare M−N−C cathode electrocatalyst materials for ORR. (B) Noninnocent ligand participation in the ORR.[7−9] (C) Metal−organic frameworks used as single precursors for unsupported and nondoped ORR electrocatalysts.

lenes, we wished to focus on constructing several related but unique heterobivalent scaffolds. This would have given us means to see whether and how different organic ligands could affect the morphology and catalytic performance of the final electrocatalyst materials. To test this hypothesis, we prepared three MOFs as insoluble, *polycrystalline* powders TAL-1, TAL-6, and TAL-7 from iron chloride and 5,6-disubstituted 1*H*-benzo[*d*]imidazoles (**1**, R = OH; **2**, R = COOH; **3**, R = OCH_3) as ligands (Figure 2A). For TAL-1, we have tested various ratios of metal to linker (2:1, 1:1, 1:2); however, they did not significantly alter the chemical composition of the material obtained (Table S5). TAL materials were then subjected to carbonization at T = 900 °C and acid leaching to give three electrocatalysts termed TAL-1-900, TAL-6-900, and TAL-7-900, respectively.

The structure and morphology of prepared electrocatalysts were examined by powder X-ray diffraction (PXRD), X-ray photoelectron spectroscopy (XPS), and high-resolution scanning and transmission electron microscopy (HRSEM and HRTEM) (Figure 2 and SI). The HRTEM images of TAL-1-900 and TAL-7-900 show dense α-Fe/Fe_3C@C nanocrystals, which are embedded into the structured, onion-like shells of carbon (Figure 2B). The characteristic layer distance of the iron/iron carbide particles was 0.203 nm, and the spacing of the carbon shells was 0.371 nm; they remain constant after acid leaching.[24−27] The presence of α-Fe in the Fe_3C@C nanocrystals in TAL-1-900 and TAL-7-900 was confirmed by PXRD (Figure 2C). TAL-6-900 material, however, incorporated iron oxide nanoparticles with a characteristic interplanar spacing of 0.29 nm corresponding to d(220) of Fe_3O_4.[28] The XPS survey spectra show the presence of carbon, oxygen, nitrogen, and iron on the surface of the catalyst materials (Figure 2D, Figure S1, and Table S2). The deconvolved N 1s region shows the presence of graphitic N (nitrogen), pyrrolic N, Fe−N_x, and pyridinic N species, which are all required for the high ORR/OER activity.[10,11,23] The iron content at the surface of the materials was low (<0.41 at. %). This is consistent with a low total content of iron in the materials as measured by microwave plasma atomic emission spectroscopy (MP-AES) (Table S1, <3.6 wt %).

With the optimized materials in hand, we evaluated the electrochemical behavior of TAL-1-900, TAL-6-900, and TAL-7-900 using cyclic voltammetry (CV) in argon-saturated 0.1 M KOH solution at room temperature (Figure 3A). We compared electrochemical performance (catalyst loading 800 μg cm^{-2}; loading dependences are shown in Figure S6c)

DOI: 10.1021/acsaem.9b02039
ACS Appl. Energy Mater. 2020, 3, 152−157

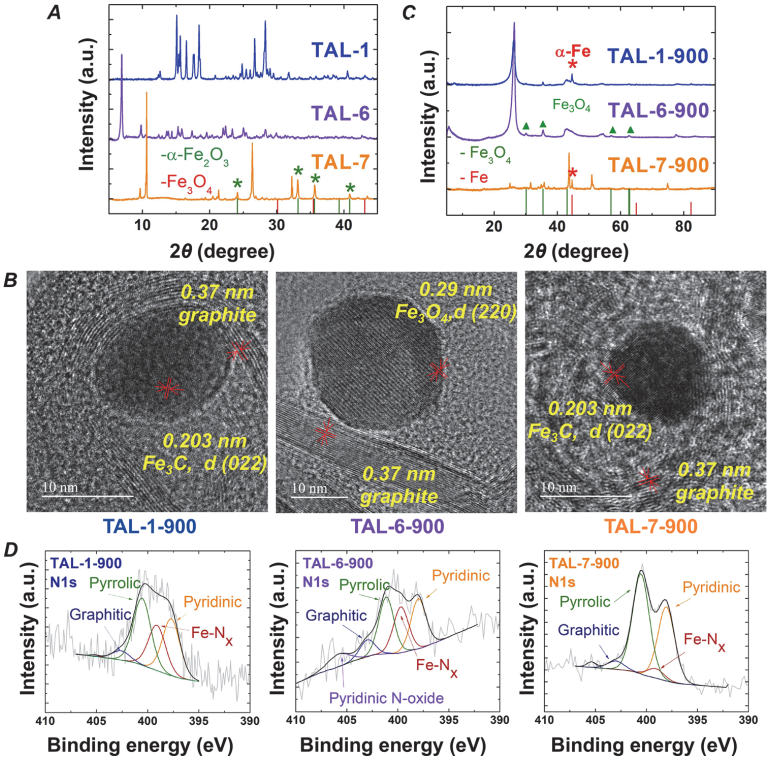

Figure 2. Physical and morphological characterization of TAL-X-900 precursors and derived catalyst materials. (A) PXRD patterns of TAL precursors. (B) HRTEM micrographs. (C) PXRD patterns of TAL-derived catalyst materials. (D) XPS core-level spectra in the N 1s region. Scale bars, 10 nm.

against the state-of-the-art commercial 20 wt % Pt/C catalyst (E-TEK; loading 20 μg_{Pt} cm^{-2}).

The TAL electrocatalysts exhibited a symmetrical and rectangular CV profile without any characteristic redox features. The double-layer capacitance was larger than that of Pt/C, indicating that TAL-derived materials have a high electrochemically accessible surface area. The porosity of prepared catalysts was examined with the Brunauer−Emmett−Teller (BET) multipoint theory (Table S4). TAL-1-900 has slightly larger surface area, while the pore size distribution indicates that all the materials are mesoporous (Figure S3).

The rotating disk electrode (RDE) technique was employed to study the ORR kinetics of TAL-modified glassy carbon (GC) electrodes in O_2-saturated 0.1 M KOH (Figure 3B). TAL-1-900 (R = OH) performed on par with 20 wt % Pt/C catalyst (E_{on} = 1.01 V, $E_{1/2}$ = 0.87 V vs E_{on} = 1.01 V, $E_{1/2}$ = 0.85 V). While TAL-6-900 was less active than TAL-1-900, electrocatalyst TAL-7-900 showed good performance, albeit with a slight offset in the onset potential (E_{on}). Notably, when **1** and iron(III) chloride were premixed in DMF for 2 h, concentrated, and subjected to carbonization, the afforded material was not effective in the ORR tests (data not shown). Hence, the formation of corresponding MOFs is a prerequisite for fabrication of an active electrocatalyst. The effect of various catalyst loadings was explored. RDE measurements confirmed that increasing the catalyst loading from 0.1 to 0.8 mg cm^{-2} significantly improved the ORR activity (Figure S4c): higher current densities and more positive half-wave potentials. For loadings <0.4 mg cm^{-2}, the calculated electron count (n) was <4.

Koutecky−Levich (K−L) plots (Figure 3C) were constructed from the RDE data (Figure 3D) and showed good linearity and parallelism for TAL-1-900. This behavior is typical for the first-order reaction kinetics with respect to the concentration of dissolved dioxygen. The number of electrons transferred per O_2 molecule (n) was calculated from the RDE data using the K−L equation. All TAL-derived electrocatalysts follow the desired four-electron transfer pathway (n = 4; the insets in Figure 3C and Figure S11), indicating that oxygen is reduced fully to water. Kinetic current densities were calculated using the K−L equation at 0.9 V and compared. TAL-1-900 exhibited the j_k value similar to that of Pt/C (2.0 vs 1.9 mA cm^{-2}).

In the kinetically controlled region of the ORR, the Tafel plots of TAL-1-900 overlapped with those of Pt/C, with two distinct regions present at different potential ranges (Figure 3E). TAL-1-900 catalyst had similar dual Tafel slopes in the low and high overpotential regions as Pt/C (−56 and −130 mV dec^{-1} vs −61 and −117 mV dec^{-1}). The Tafel slope value of −56 mV dec^{-1} for TAL-1-900 indicates that the rate-determining step in the ORR is the formation of adsorbed intermediates (OOH).

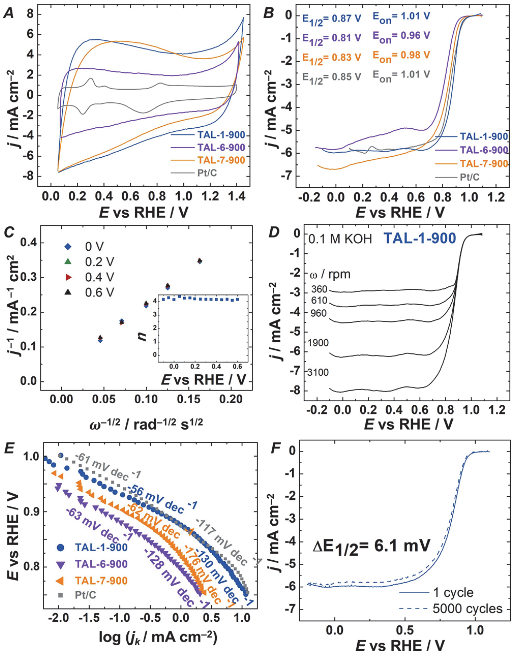

Figure 3. Electrochemical oxygen reduction on TAL materials in 0.1 M KOH. (A) Cyclic voltammograms of electrocatalyst-modified GC electrodes (under argon); ν = 50 mV s^{-1}. (B) RDE polarization curves for TAL and Pt/C-modified GC electrodes at 1900 rpm; ν = 10 mV s^{-1}. (C) Koutecky−Levich plots for O_2 reduction on TAL-1-900 modified GC electrode. Inset: number of electrons transferred per O_2 molecule. (D) RDE polarization data on oxygen reduction recorded at various rotation rates on TAL-1-900 modified GC electrode; ν = 10 mV s^{-1}. (E) Tafel plots for O_2 reduction on TAL and Pt/C catalysts. (F) Electrochemical stability test for TAL-1-900 (mid-range: 0.6−1.0 V).

After continuous cycling from 0.6 to 1.0 V vs RHE, electrocatalytic activity of TAL-1-900 remained at the same level without any change in the onset potential (Figure 3F). However, only a slight decrease in diffusion-limited current density was observed indicating that its porosity remains largely unaffected.

As TAL-1-900 showed excellent electrocatalytic behavior in the ORR tests, we wished to see how it performs in the oxygen evolution reaction (Figure 4). The materials with high bifunctional activity are used in metal−air batteries;[23] however, the active sites responsible for OER's high activity are different from the sites required for ORR.[10,11,23] To assess the overall oxygen electrode activity (ΔE) of TAL electrocatalysts, the potential differences of OER at a current density of 10 mA cm^{-2} and of ORR at a current density of −3 mA cm^{-2} were calculated at electrode rotation rate of 1600 rpm. The bifunctional ORR/OER activity of TAL-1-900 (ΔE = 0.73 V; E_{10} = 1.60 V @10 mA cm^{-2}) is among the best reported to date (Table S7), while TAL-6-900 and TAL-7-900 were less active (ΔE = 0.83 and 0.78 V, respectively).

TAL-1-900 has a Tafel slope of 84 mV dec^{-1} (Figure 4B), which is considerably smaller than those of TAL-6-900 (95 mV dec^{-1}), TAL-7-900 (112 mV dec^{-1}), RuO_2 (116 mV dec^{-1}), and Pt/C (112 mV dec^{-1}), indicating faster OER kinetics. The durability of the TAL-1-900 catalyst was evaluated by a chronoamperometry test at an applied potential of 1.6 V (Figure 4C). The current density of the TAL-1-900 catalyst shows a slight increase during the testing time, demonstrating that the catalyst exhibits excellent durability toward OER. Electrocatalytic OER behavior also remained unchanged after continuous cycling of the TAL-1-900 electrode 5000 times in the potential range between 1.0 and 1.8 V vs RHE (Figure 4D).

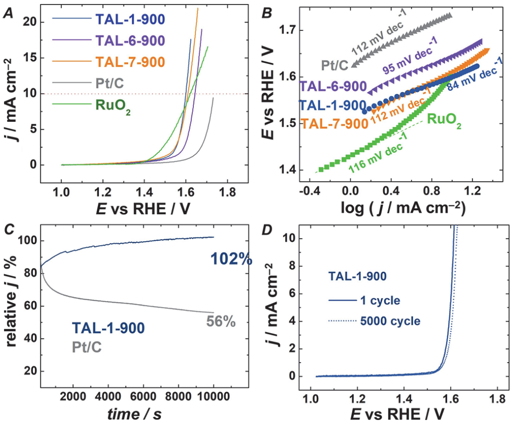

Figure 4. Electrochemical oxygen evolution on TAL materials in 0.1 M KOH. (A) LSV curves for TAL-modified GC electrodes, ν = 10 mV s^{-1}. (B) Tafel plots based on LSV curves. (C) Chronoamperometric response for TAL-1-900 and Pt/C recorded at applied potential of 1.6 V. (D) Electrochemical stability of TAL-1-900 after 5000 cycles.

The overall relationship TAL-1-900 > TAL-7-900 ≫ TAL-6-900 indicates that electron-rich precursors may boost the ORR/OER catalyst's activity. Our observation, however, may have several alternative explanations. These include rendering the activity of Fe−N_x sites and pyridinic, pyrrolic, and graphitic nitrogen;[8−11] initiation of the ligand-centered 2e × 2e pathway similar to the one proposed for HITP and HHTP ligands (Figure 1B);[7,20,21] creation of catalytically active M−O_x[14] or mixed Fe−N_xO_y sites; the control of pore sizes and other structural aspects of the carbonized molecular meshwork. Notably, in the case of TAL-6-900, we observed formation of Fe_3O_4 but not Fe/Fe_3C nanocrystals. While the M−N_x species are known to reduce dioxygen in the ORR via a direct reduction of oxygen to hydroxide (a 4e process), the less active metal-based particles (e.g., Fe/Fe_3C,[24−27] Fe_2N[26]) do it in a stepwise 2e × 2e manner (first, forming the peroxides and then decomposing them to water).[10,11,24,25] This observation also suggests that the organic linker itself may modulate not only the rate of formation of nanocrystals embedded into carbon support but also their composition.

Interestingly, we observed an improvement in the TAL-1-900 vs TAL-7-900 performance. This may be attributed to the catechol unit itself because the iron−catechol complexation is sufficiently strong,[29] and several polycatechol-based covalent[30] and metal−organic frameworks were previously reported.[14,20] Hence, employing catechol precursors may lead to increased conductivity of the final material and/or additional (electro)-

chemical contributions (e.g., enhanced carbonization or ligand-centered 2*e* × 2*e* processes).

In summary, we have surveyed a series of carbon-rich, fused hybrid-type organic linkers to construct iron-based MOFs, which serve as direct precursors for efficient bifunctional electrocatalyst materials. This single simple-precursor strategy relied on carbonization of benzimidazole derivatives under a nonmodifying (N_2) atmosphere. The active Fe−N−C materials contained $Fe-N_x$ sites, pyridinic nitrogen, and Fe/Fe_3C nanocrystals, except for TAL-6-900, which contained Fe_3O_4 and was much less active. Our results confirm that there is a link between the electronic and ligating properties of the initial organic ligands and the electrocatalytic properties of the final electrocatalyst materials. Translating this into practice will require further exploration of structure−activity relationships of chemically decorated carbon-rich precursors.

ASSOCIATED CONTENT

Supporting Information

The Supporting Information is available free of charge at https://pubs.acs.org/doi/10.1021/acsaem.9b02039.

> Experimental details and characterization of catalyst materials (PXRD, XPS, MP-AES, HRTEM, HRSEM, BET, CHN analysis, and Raman), characterization of spent catalyst (PXRD, HRTEM), and preparation and characterization of ligands (NMR, IR) (PDF)

AUTHOR INFORMATION

Corresponding Authors

*E-mail: nadezda.kongi@ut.ee.
*E-mail: pavel.starkov@taltech.ee.

ORCID

Pavel Starkov: 0000-0003-1421-4731

Present Address

#A.B.: Department of Chemistry, Durham University, South Road, Durham DH1 3LE, United Kingdom.

Author Contributions

The manuscript was written through contributions of all authors. All authors have given approval to the final version of the manuscript.

Notes

The authors declare the following competing financial interest(s): K.P., K.T., N.K., P.S. are inventors on a related patent application owned by Tallinn University of Technology and the University of Tartu.

ACKNOWLEDGMENTS

This research was supported by Estonian Research Council Grant PUT1290 and TalTech Young Investigator Grant B62 (to P.S.); Estonian Research Council Grant PSG250 (to N.K.) and an Institutional Research Funding IUT20-16 of the Estonian Ministry for Education and Research and the Centre of Excellence TK141: Advanced materials and high-technology devices for energy recuperation systems from the EU ERDF program (both to K.T.). We thank COST Actions CA15135 and CA18224 members for helpful discussions and Dr. Maike Käärik and Dr. Jaan Leis for the BET measurements. TalTech (V.M.) and UT HRSEM (S.V.) facilities are supported by TK141, and IUT-T4 and PUT1689, respectively. TalTech (A.M.) and UT (J.A.) XRD facilities are supported by IUT19-4 and TK141. UT HRTEM (M.R., V.S.) and BET facilities are supported by Institutional Research Funding IUT2-24 and IUT34-14 of the Estonian Ministry for Education and Research. K.P. acknowledges the Estonian Smart Specialization PhD Fellowship.

REFERENCES

(1) Wu, H. B.; Lou, X. W. Metal-organic frameworks and their derived materials for electrochemical energy storage and conversion: promises and challenges. *Sci. Adv.* **2017**, *3*, No. eaap9252.

(2) Diercks, C. S.; Kalmutzki, M. J.; Diercks, D. J.; Yaghi, O. M. Conceptual advances from Werner complexes to metal−organic frameworks. *ACS Cent. Sci.* **2018**, *4*, 1457−1464.

(3) Zhao, S.; Yin, H.; Du, L.; He, L.; Zhao, K.; Chang, L.; Yin, G.; Zhao, H.; Liu, S.; Tang, Z. Carbonized nanoscale metal−organic frameworks as high performance electrocatalyst for oxygen reduction reaction. *ACS Nano* **2014**, *8*, 12660−12668.

(4) Xia, B. Y.; Yan, Y.; Li, N.; Wu, H. B.; Lou, X. W.; Wang, X. A metal−organic framework-derived bifunctional oxygen electrocatalyst. *Nat. Energy* **2016**, *1*, 15006.

(5) Zhao, R.; Liang, Z.; Gao, S.; Yang, C.; Zhu, B.; Zhao, J.; Qu, C.; Zou, R.; Xu, Q. Puffing up energetic metal−organic frameworks to large carbon networks with hierarchical porosity and atomically dispersed metal sites. *Angew. Chem., Int. Ed.* **2019**, *58*, 1975−1979.

(6) Shinde, S. S.; Lee, C. H.; Jung, J.-Y.; Wagh, N. K.; Kim, S.-H.; Kim, D.-H.; Lin, C.; Lee, S. U.; Lee, J. H. Unveiling dual-linkage 3D hexaiminobenzene metal−organic frameworks towards long-lasting advanced reversible Zn−air batteries. *Energy Environ. Sci.* **2019**, *12*, 727−738.

(7) Miner, E. M.; Gul, S.; Ricke, N. D.; Pastor, E.; Yano, J.; Yachandra, V. K.; van Voorhis, T.; Dincă, M. Mechanistic evidence for ligand-centered electrocatalytic oxygen reduction with the conductive MOF Ni_3(hexaiminotriphenylene)$_2$. *ACS Catal.* **2017**, *7*, 7726−7731.

(8) Guo, D.; Shibuya, R.; Akiba, C.; Saji, S.; Kondo, T.; Nakamura, J. Active sites of nitrogen-doped carbon materials for oxygen reduction reaction clarified using model catalysts. *Science* **2016**, *351*, 361−365.

(9) Kabir, S.; Artyushkova, K.; Serov, A.; Atanassov, P. Role of nitrogen moieties in N-doped 3D-graphene nanosheets for oxygen electroreduction in acidic and alkaline media. *ACS Appl. Mater. Interfaces* **2018**, *10*, 11623−11632.

(10) Sarapuu, A.; Kibena-Põldsepp, E.; Borghei, M.; Tammeveski, K. Electrocatalysis of oxygen reduction on heteroatom-doped nanocarbons and transition metal−nitrogen−carbon catalysts for alkaline membrane fuel cells. *J. Mater. Chem. A* **2018**, *6*, 776−804.

(11) Shao, M.; Chang, Q.; Dodelet, J.-P.; Chenitz, R. Recent advances in electrocatalysts for oxygen reduction reaction. *Chem. Rev.* **2016**, *116*, 3594−3657.

(12) Jasinski, R. A new fuel cell cathode catalyst. *Nature* **1964**, *201*, 1212−1213.

(13) Jiang, R.; Li, L.; Sheng, T.; Hu, G.; Chen, Y.; Wang, L. Edge-site engineering of atomically dispersed $Fe-N_4$ by selective C−N bond cleavage for enhanced oxygen reduction reaction activities. *J. Am. Chem. Soc.* **2018**, *140*, 11594−11598.

(14) Zhong, H.; Ly, K. H.; Wang, M.; Krupskaya, Y.; Han, X.; Zhang, J.; Zhang, J.; Kataev, V.; Büchner, B.; Weidinger, I. M.; Kaskel, S.; Liu, P.; Chen, M.; Dong, R.; Feng, X. A phthalocyanine-based layered two-dimensional conjugated metal-organic framework as a highly efficient electrocatalyst for the oxygen reduction reaction. *Angew. Chem., Int. Ed.* **2019**, *58*, 10677−10682.

(15) Zhang, W.; Lai, W.; Cao, R. Energy-related small molecule activation reactions: oxygen reduction and hydrogen and oxygen evolution reactions catalyzed by porphyrin- and corrole-based systems. *Chem. Rev.* **2017**, *117*, 3717−3797.

(16) Lefèvre, M.; Proietti, E.; Jaouen, F.; Dodelet, J.-P. Iron-based catalysts with improved oxygen reduction activity in polymer electrolyte fuel cells. *Science* **2009**, *324*, 71−74.

(17) Strickland, K.; Miner, E.; Jia, Q.; Tylus, U.; Ramaswamy, N.; Liang, W.; Sougrati, M.; Jaouen, F.; Mukerjee, S. Highly active oxygen

reduction non-platinum group metal electrocatalyst without direct metal-nitrogen coordination. *Nat. Commun.* **2015**, *6*, 7343.

(18) Ratso, S.; Ranjbar Sahraie, N.; Sougrati, M. T.; Käärik, M.; Kook, M.; Saar, R.; Paiste, P.; Jia, Q.; Leis, J.; Mukerjee, S.; Jaouen, F.; Tammeveski, K. Synthesis of highly-active Fe−N−C catalysts for PEMFC with carbide-derived carbons. *J. Mater. Chem. A* **2018**, *6*, 14663−14674.

(19) Hu, Y.; Jensen, J. O.; Zhang, W.; Cleemann, L. N.; Xing, W.; Bjerrum, N. J.; Li, Q. Hollow spheres of iron carbide nanoparticles encased in graphitic layers as oxygen reduction catalysts. *Angew. Chem., Int. Ed.* **2014**, *53* (2014), 3675−3679.

(20) Miner, E. M.; Wang, L.; Dincă, M. Modular O_2 electroreduction activity in triphenylene-based metal−organic frameworks. *Chem. Sci.* **2018**, *9*, 6289−6291.

(21) Liu, X.-H.; Hu, W.-L.; Jiang, W.-J.; Yang, Y.-W.; Niu, S.; Sun, B.; Wu, J.; Hu, J.-S. Well-defined metal−O_6 in metal−catecholates as a novel active site for oxygen electroreduction. *ACS Appl. Mater. Interfaces* **2017**, *9*, 28473−28477.

(22) Kong, D.; Gao, Y.; Xiao, Z.; Xu, X.; Li, X.; Zhi, L. Rational design of carbon-rich materials for energy storage and conversion. *Adv. Mater.* **2019**, *31*, 1804973.

(23) Huang, Z.-F.; Wang, J.; Peng, Y.; Jung, C.-Y.; Fisher, A.; Wang, X. Design of efficient bifunctional oxygen reduction/evolution electrocatalyst: recent advances and perspectives. *Adv. Energy Mater.* **2017**, *7*, 1700544.

(24) Yang, W.; Liu, X.; Yue, X.; Jia, J.; Guo, S. Bamboo-like carbon nanotube/Fe_3C nanoparticle hybrids and their highly efficient catalysis for oxygen reduction. *J. Am. Chem. Soc.* **2015**, *137*, 1436−1439.

(25) Kim, J. H.; Sa, Y. J.; Jeong, H. Y.; Joo, S. H. Roles of Fe−N_x and Fe−Fe_3C@C species in Fe−N/C electrocatalysts for oxygen reduction reaction. *ACS Appl. Mater. Interfaces* **2017**, *9*, 9567−9575.

(26) Sun, T.; Jiang, Y.; Wu, Q.; Du, L.; Zhang, Z.; Yang, L.; Wang, X.; Hu, Z. Is iron nitride or carbide highly active for oxygen reduction reaction in acidic medium? *Catal. Sci. Technol.* **2017**, *7*, 51−55.

(27) Hu, E.; Yu, X.-Y.; Chen, F.; Wu, Y.; Hu, Y.; Lou, X. W. Graphene layers-wrapped Fe/Fe_5C_2 nanoparticles supported on N-doped graphene nanosheets for highly efficient oxygen reduction. *Adv. Energy Mater.* **2018**, *8*, 1702476.

(28) Yang, S.; Jiang, J.-T.; Xu, C.-Y.; Wang, Y.; Xu, Y.-Y.; Cao, L.; Zhen, L. Synthesis of Zn(II)-doped magnetite leaf-like nanorings for efficient electromagnetic wave absorption. *Sci. Rep.* **2017**, *7*, 45480.

(29) Filippidi, E.; Cristiani, T. R.; Eisenbach, C. D.; Waite, J. H.; Israelachvili, J. N.; Ahn, B. K.; Valentine, M. T. Toughening elastomers using mussel-inspired iron-catechol complexes. *Science* **2017**, *358*, 502−505.

(30) Côté, A. P.; Benin, A. I.; Ockwig, N. W.; O'Keeffe, M.; Matzger, A. J.; Yaghi, O. M. Porous, crystalline, covalent organic frameworks. *Science* **2005**, *310*, 1166−1170.

Publication II

Ping, K.; Alam, M.; Kahnert, S. R.; Bhadoria, R.; Mere, A.; Mikli, V.; Käärik, M.; Aruväli, J.; Paiste, P.; Kikas, A.; Kisand, V.; Järving, I.; Leis, J.; Tammeveski, K.; Kongi, N.; Starkov, P.

Multi-purpose chemo- and electrocatalyst material from an amorphous cobalt metal–organic framework.

Mater. Adv. **2021,** *2,* 4005–4019.

DOI:10.1039/D1MA00414J

Materials Advances

ROYAL SOCIETY OF CHEMISTRY

PAPER

View Article Online
View Journal | View Issue

Check for updates

Cite this: *Mater. Adv.*, 2021, 2, 4009

Multi-purpose heterogeneous catalyst material from an amorphous cobalt metal–organic framework†

Kefeng Ping,‡[a] Mahboob Alam,‡[a] Sean Ray Kahnert,§[a] Rohit Bhadoria,[a] Arvo Mere,[b] Valdek Mikli,[b] Maike Käärik,[c] Jaan Aruväli,[d] Päärn Paiste,[d] Arvo Kikas,[e] Vambola Kisand,[e] Ivar Järving,[a] Jaan Leis,[c] Nadežda Kongi *[c] and Pavel Starkov *[a]

Received 6th May 2021,
Accepted 15th May 2021

DOI: 10.1039/d1ma00414j

rsc.li/materials-advances

Sustainable technologies rely on the development of universal catalyst materials. While a lot of the attention has been given to improving the performance of one single catalyst material for one specific application, there is still a need to find ways to develop catalysts that can simultaneously be utilized for several chemo- and electrocatalytic processes. In this work, we have surveyed a series of novel, cobalt-based catalyst materials derived from an amorphous MOF in an array of diverged applications. Specifically, we have focused on organic transformations such as oxidative of alkylarenes and benzylic homocoupling reactions as well as several electrocatalytic processes, which directly relate to energy conversion and storage devices, such as oxygen reduction (ORR), oxygen evolution (OER) and hydrogen evolution (HER) reactions. We have observed that only one material, TAL-2-900, delivered the optimal solution. The stability and recyclability of this unique multifunctional material has been examined.

1. Introduction

The notion of M–N–C catalysts, where M is typically Fe, Co, Mn or Ni, is often reserved for the catalysts developed for applications in energy conversion and storage devices.[1–3] However, recent reports have also emphasized the potential of this type of materials in facilitating heterogeneous organic transformations.[4–6]

There is an accountable divergence in the ways that the M–N–C materials are prepared, and they depend on the ultimate application prerogative.[1–12] When used in the electrochemical settings, the underlying materials are typically acid-etched to make sure that the additional influence of related nanoparticles (metal and/or that of metal oxides, carbides, nitrides, sulfides and phosphides) deposited directly at the surface of the catalyst is eliminated. In heterogeneous catalysis applications, however, the contribution of these species to the overall chemical reactivity – while being well acknowledged and often relied upon – is not readily distinguished from the instances of single-atom catalysis[9,10] and the role that nanocrystals protected by graphitic carbon layers might play.

Metal–organic frameworks (MOFs) are one of the most attractive building blocks for the formation of active M–N–C materials.[12] Whereas only a handful of crystalline MOFs can directly be used as electrocatalysts,[13–15] a vast majority of MOFs still require an additional carbonization step to allow for increased stability and conductivity as well as to introduce a variety of catalytically active species (M–N$_x$).[12] During this process, additional doping with heteroatoms and metals[7,8] or the use of alternative supports[16,17] is often advantageous.

While crystalline MOFs are widely used for carbonization,[7–9] their innate crystallinity may not always be a critical factor to achieve high catalytic activities (aside from contributing to the topology). All the catalyst materials reported to date are based on monometallic (*e.g.* MIL-101, ZIF-67, MOF-74-Zn, Prussian blue analogues)[11] and mixed ligand/mixed metal (*e.g.* the MIL-101/ZIF-67 composite[18] and ZnCo-MOFs[19]) MOFs are highly crystalline. During the pyrolysis, however, MOFs undergo drastic molecular rearrangements; hence, amorphous MOFs can be used as the precursors.[20,21] To this end, we recently assessed iron-based catalysts derived from polycrystalline

---

[a] *Department of Chemistry and Biotechnology, Tallinn University of Technology, Tallinn 12618, Estonia. E-mail: pavel.starkov@taltech.ee*
[b] *Department of Materials and Environmental Technology, Tallinn University of Technology, Tallinn 19086, Estonia*
[c] *Institute of Chemistry, University of Tartu, Tartu 50411, Estonia. E-mail: nadezda.kongi@ut.ee*
[d] *Institute of Ecology and Earth Sciences, University of Tartu, Tartu 50411, Estonia*
[e] *Institute of Physics, University of Tartu, Tartu 50411, Estonia*

† Electronic supplementary information (ESI) available. See DOI: 10.1039/d1ma00414j

‡ These authors contributed equally.

§ Present address: Institute of Organic Chemistry, Clausthal University of Technology, Clausthal-Zellerfeld 38678, Germany.

metal–organic framework precursors (TAL-1-900, TAL-6-900, TAL-7-900),[22,23] which were based on carbon-rich[24] organic linkers. Even the slightest variations around the benzimidazole core have led to alterations in the performance of the materials as bifunctional oxygen electrocatalysts[22] and in heterogeneous catalysis.[23]

Herein, we report a unique *amorphous* cobalt-based MOF-derived multifunctional material, which acts as an efficient trifunctional electrocatalyst[25,26] and as a robust heterogeneous catalyst.

2. Results and discussion

2.1 Morphological and physical characterizations

We prepared a series of catalysts from an amorphous metal–organic framework precursor TAL-2 by carbonizing it at different temperatures (Fig. 1). Importantly, we have treated these carbonized materials with 0.5 M HNO_3 to remove the traces of cobalt(0) and cobalt oxides from the surface of the materials. Regardless of this treatment, the final porous M–N–C materials still contained cobalt(0) nanoparticles, which were protected by the graphitic layers as is evident from the high resolution transmission electron microscopy (HRTEM; Fig. 1B–D and Fig. S1, S2, ESI†) micrographs. Increasing the temperature of carbonization did not lead to a substantial change in the N_2 adsorption/desorption isotherms or the distribution of pore sizes, which effectively remained in the 3–4 nm range (Fig. 1E and F). However, as is seen in the powder X-ray diffraction (PXRD; Fig. 1G) patterns and the microwave plasma-atomic emission spectroscopy (MP-AES; Table S1, ESI†) datasets, the graphitic carbon and cobalt(0) content was significantly higher in the samples that have been treated at 900 and 1000 °C. The X-ray photoelectron spectroscopy (XPS) data indicated that carbonization at higher temperatures both lowered the nitrogen content and altered the distribution of nitrogen species at the surface (Fig. S3 and Tables S1–S5, ESI†).

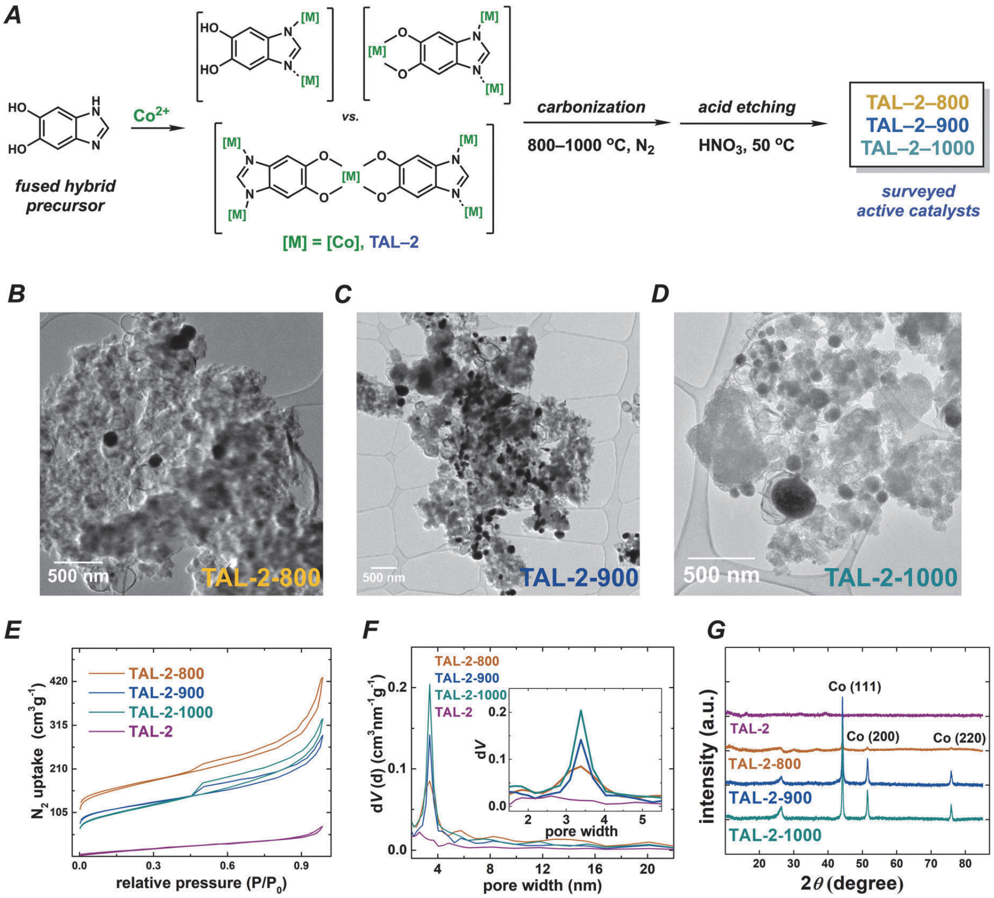

Fig. 1 (A) Preparation of TAL-2 derived catalysts materials. HRTEM micrographs of (B) TAL-2-800, (C) TAL-2-900 and (D) TAL-2-1000 catalysts. Physical characterization of the materials by (E) N_2 uptake, and (F) pore size distribution and (G) PXRD patterns.

2.2 Oxidative organic transformations

The *de novo* Co–N–C catalysts were screened against oxidative transformations with *tert*-butyl peroxide (TBHP) as terminal oxidant at a considerably low catalyst loadings, namely, that of 5 mg mmol^{-1}. While TBHP-driven oxidations of arylmethanes have been reported to be catalyzed by Fe–N–C materials effectively,[23,27–29] the cobalt corresponding Co–N–C catalysts were not.[30] Typically, Co–N–C catalysts are used for reduction reactions (nitroarenes,[31,32] *N*-heterocycles,[33] and hydrocarbons[34]), reductive aminations[35] and alkylations,[36,37] while the oxidative esterification of benzyl alcohols were done under dioxygen.[38–40]

Overall, the cobalt materials outperformed the three previously reported related Fe–N–C systems (TAL-1-900, TAL-6-900, TAL-7-900),[22,23] and importantly, they sustained their activity over a larger number of cycles (Fig. 2A and B; Tables S6 and S7, ESI†). TAL-2-900 and TAL-2-1000 were more active because they contained metallic Co nanoparticles, which were protected by graphitic carbon layers, as confirmed by PXRD and HRTEM.

Interestingly, TAL-2-900 was a more robust catalyst for converting toluene to benzoic acid, while TAL-2-1000 was better at oxidizing diphenylmethane to benzophenone. This indicates that small differences in the active sites (*e.g.* the total content of pyridinic nitrogen) at the surface of the catalyst play an important role in catalyst stability. A further set of substrates was subjected to oxidation (Fig. 2C). Addition of acetic acid slightly improved the yields in the cases where polymethylated arenes were converted to the corresponding carboxylic acids.

2.3 Benzylic homocoupling

Knowing that radical pathways were involved in oxidative transformation reactions, has encouraged us to extend the use of TAL-2-900 as a heterogeneous catalyst for carbon–carbon bond forming reactions *via* activation at the benzylic positions. While M–N–C materials are widely explored in oxidative and reductive processes,[4–6] there is only a handful of examples of their use in other organic transformations. For instance, Zhang *et al.* developed an oxidative coupling between primary and secondary alcohols.[41] This reaction was shown to proceed *via* formation of intermediary aldehydes and ketones, respectively, which undergo aldol condensation. A reductive C–H alkylation of quinolines by aldehydes using cobalt-based catalysts was also demonstrated.[42,43]

We were interested to see whether the M–N–C catalysts could be compatible with organometallic reagents; hence, we explored C(sp^3)–C(sp^3) homocoupling reaction of benzyl bromides in the presence of a Grignard reagent. This reaction traditionally requires stoichiometric metallic lithium,[44] magnesium,[45] copper[46] or nickel.[47] Recently, a rhodium-catalyzed

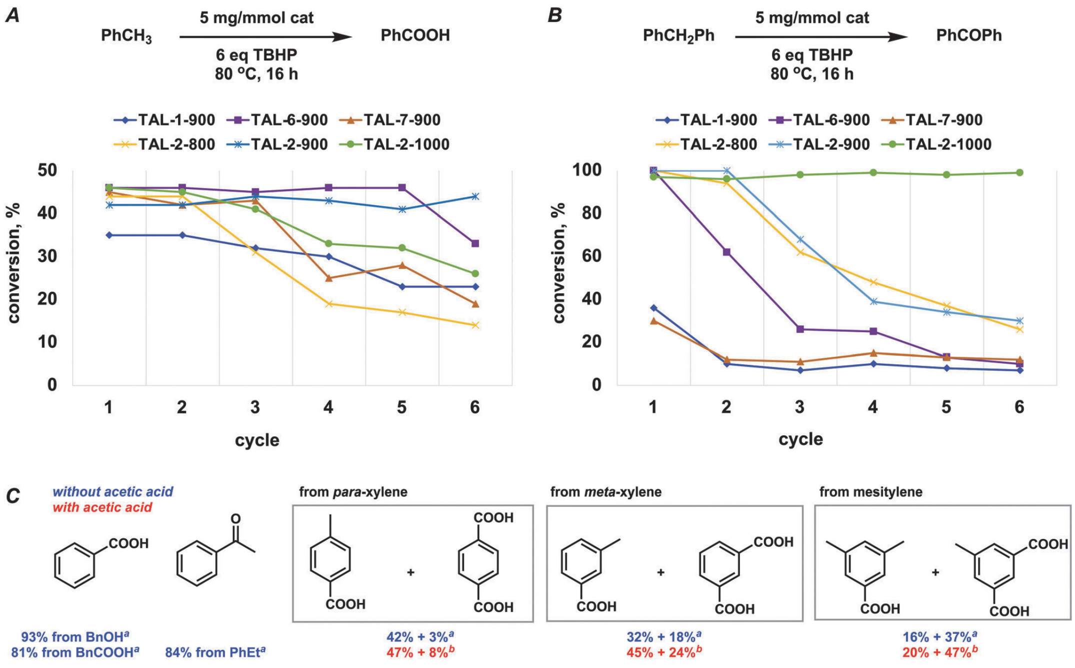

[a] ***Reaction conditions:*** **substrate (1.0 equiv), TBHP (6 equiv per CH_3 group), TAL-2-900 (5 mg/mmol), neat, 80 °C, 24 h.** [b] **Additional AcOH (1 equiv per CH_3 group)**

Fig. 2 Use of TAL-derived catalysts in oxidative transformations. (A) Catalyst recyclability during oxidation of toluene into benzoic acid. (B) Catalyst recyclability during oxidation of diphenylmethane into benzophenone (conversion were determined by NMR using 1,3,5-trimethoxybenzene as internal standard). (C) Substrate scope for TAL-2-900-catalyzed oxidations (isolated yields).

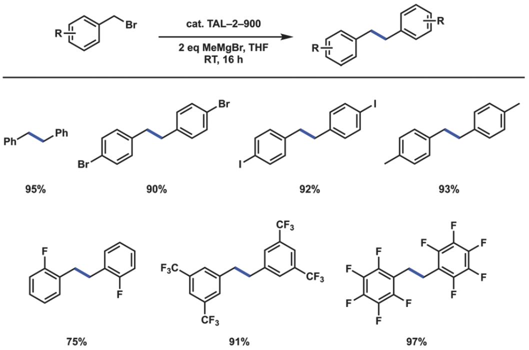

^{a} *Reaction conditions:* substrate (1.0 equiv), MeMgBr (2.0 equiv), TAL-2-900 (5 mg/mmol), THF, RT, 16 h

Scheme 1 TAL-2-900 catalyzed C(sp^3)–C(sp^3) homocoupling reactions^a.

version employing dimethylzinc was demonstrated,[48] and several photocatalyzed conditions were developed.[49,50] Gratifyingly, we observed the desired homocoupling products with cobalt based catalyst TAL-2-900 but not the iron version (TAL-1-900) (Scheme 1). The reactions were carried out using methylmagnesium bromide at ambient temperature to give corresponding bibenzyls in good to excellent yields, while aryliodides and bromides were also well tolerated. After standard aqueous workup, the spent catalyst had a significantly reduced activity. Specifically, on the next cycle, the isolated yield of homocoupled product has dropped from 93% to 38%. Alternatively, the THF solution containing the product was removed by syringe under anhydrous conditions and the reaction vessel was recharged with THF, benzyl bromide and MeMgBr. This modification gave the desired product with an improved yield on the second run (93%).

2.4 Electrocatalytic transformations

After having identified the most promising catalyst for the organic transformations, we wished to screen the TAL-2 catalyst series as *trifunctional* electrocatalyst materials across oxygen reduction (ORR), oxygen evolution (OER) and hydrogen evolution (HER) reactions (Fig. 3). Potentially, these datasets should give insights into whether there is a link between the performance of the individual catalysts across electrocatalytic and chemocatalytic interconversions.[51,52] Out of the three catalysts, TAL-2-900, once again, showed a superior activity profiles in all of the electrocatalytic reactions.

To learn the effect of different carbonization temperatures on electrocatalytic ORR performance, TAL-2 based catalysts were tested by rotating disc electrode (RDE) and rotating ring-disc electrode (RRDE) techniques in 0.1 M KOH electrolyte. Oxygen reduction polarization curves (Fig. 3A) confirmed that TAL-2 based catalyst carbonized at 900 °C had the highest ORR electrocatalytic activity with an onset potential (E_{on}) of 1.00 V, a half-wave potential ($E_{1/2}$) of 0.85 V and a diffusion-limiting current density of -5.78 mA cm^{-2}. The kinetic parameters of TAL-2-900 were on par with the ones obtained for commercial Pt/C catalyst ($E_{\mathrm{on}} = 1.01$ V; $E_{1/2} = 0.86$; $j_{\mathrm{d}} = -6.16$ mA cm^{-2}) and other promising non-noble metal ORR catalysts (Table S9, ESI†). Despite the fact that BET surface area of TAL-2-900 (421 m^2 g^{-1}) is lower than that obtained for TAL-2-800 (589 m^2 g^{-1}) (Table S11, ESI†), the superior ORR performance of TAL-2-900 indicates higher density of electrochemically accessible active sites for ORR.

To shed light on the enhancement of the ORR activity, electrochemically active surface area (ECSA) of TAL-2 derived catalysts was estimated by collecting the electrochemical double-layer capacitance (C_{dl}) from CV curves (Table S10, ESI†). The ECSA values have decreased for the samples that were obtained by increasing the carbonization temperatures. Hence, the superior electrocatalytic activity of the TAL-2-900 sample may be explained by a higher amount of ORR active sites, specifically in the form of cobalt(0) nanoparticles.

The Koutecky–Levich (K–L) plots were constructed using data derived from RDE (Fig. S4, ESI†) and the calculated number of electrons transferred per oxygen molecule n was in all the cases approximately four. RRDE studies confirmed that oxygen reduction proceeds *via* a two-step 2×2 H_2O_2 mechanism (Fig. S5B and C, ESI†). The Tafel plot analysis demonstrated that the TAL-2-900 material had the highest slope value (-76 mV decade^{-1}) against all the other samples that were surveyed in this study (Fig. 3B). Similarly to Pt/C, this means that the rate determining step for ORR is the first electron transfer step, whereby $O_{2(\mathrm{ads})}$ is reduced to $O_{2(\mathrm{ads})}{}^{-}$. A continuous potential cycling in the range between 0.6 and 1.0 V was used to assess the long-term stability of TAL-2-900, with $E_{1/2}$ shifting only by 20 mV after 5,000 cycles (Fig. 3C). The RDE studies have confirmed that TAL-2-900 was a highly stable active ORR electrocatalyst in 0.1 M KOH.

The electrocatalytic activity towards ORR of the TAL-2-900 material has also been tested under acidic conditions (0.5 M H_2SO_4; Fig. S7, ESI†). As in the case of alkaline media, TAL-2-900 has shown higher onset and half-wave potentials (0.82 V and 0.73 V *vs.* RHE) than those for TAL-2-800 and TAL-2-1000. Notably, TAL-2-900 remained stable after 5000 cycles with $E_{1/2}$ having decreased only by 20 mV (Fig. S7D, ESI†).

The OER performance of the TAL-2 derived catalysts was assessed and i*R*-corrected OER polarization curves are shown in Fig. 3D. The benchmark current density of 10 mA cm^{-2} was achieved at 1.60 V for TAL-2-900 material, which is superior to that of ruthenium oxide (1.69 V). The Tafel slopes obtained for the OER electrocatalytic activity among the series, confirm that TAL-2-900 functions similarly to the RuO_2 systems. Under the long-term OER operation, this catalyst material is stable (Fig. 3F). The overall oxygen bifunctional electroactivity (ΔE) value for TAL-2-900 is 0.75 V, which makes it much lower than the rest of the M–N–C samples, whilst haven been screened at the similar loadings (Table S10, ESI†).

The electrocatalytic HER activity of the best performing catalyst was compared with the commercial Pt/C in 1 M KOH (Fig. 3G and H) at the current density of -10 mA cm^{-2}. Under these conditions, the overpotential with TAL-2-900 as a catalyst was achieved at -264 mV *vs.* RHE with a low Tafel slope value of 115 mV dec^{-1}. The HER overpotential values η for TAL-2-800

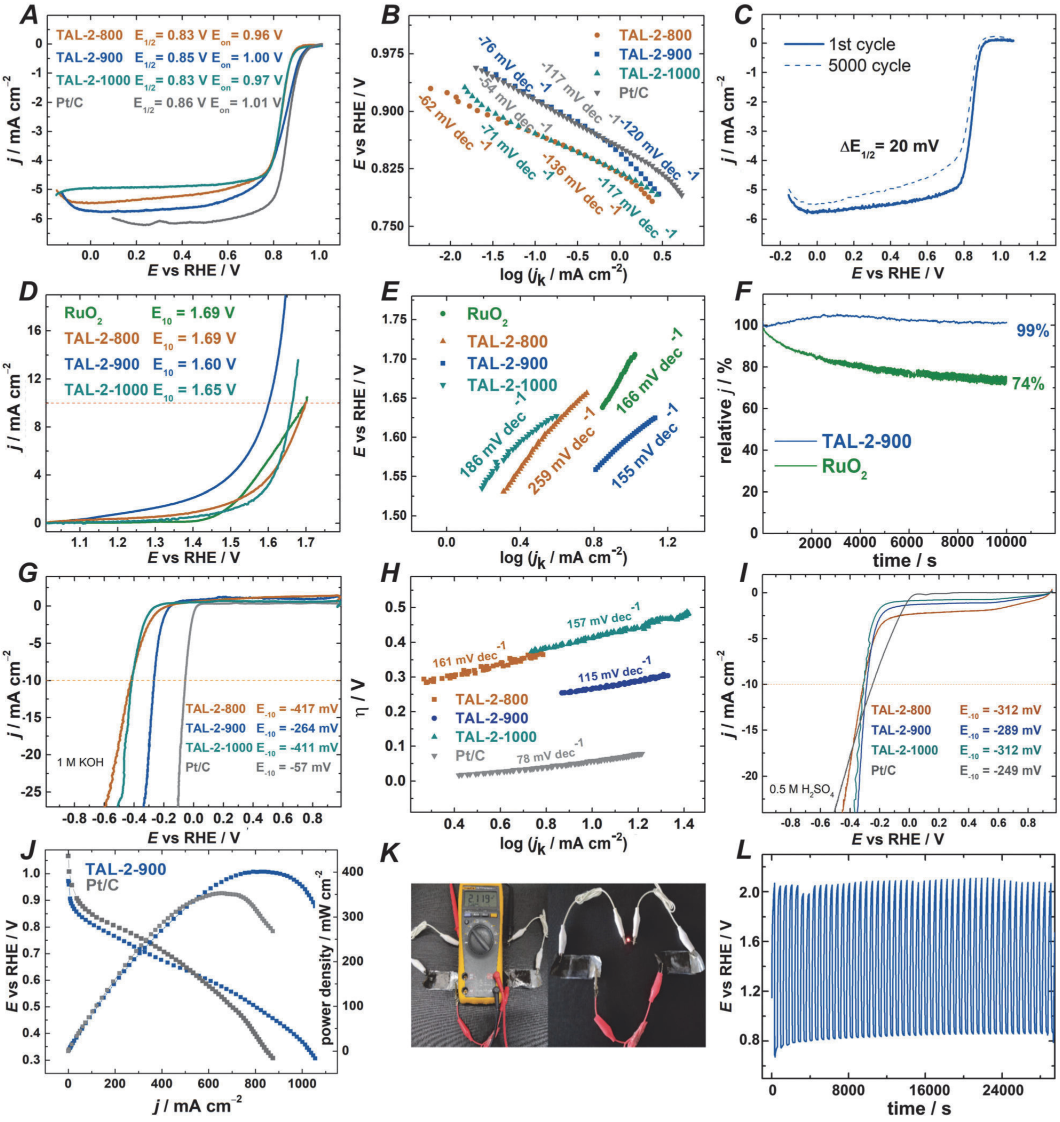

Fig. 3 Electrochemical characterization of TAL-2 derived catalyst materials. (A) ORR polarization curves for TAL and Pt/C-modified GC electrodes at 1600 rpm; ν = 10 mV s^{-1}. (B) Tafel plots for ORR on TAL and Pt/C catalysts. (C) Electrochemical ORR stability test for TAL-2-900 (mid-range: 0.6–1.0 V). (D) OER polarization curves (under argon); ν = 10 mV s^{-1}. (E) OER Tafel plots. (F) OER chronoamperometric stability of TAL-2-900 and RuO_2 in 0.1 M KOH over 10 000 seconds (1.6 V). (G) HER polarization curves for TAL and Pt/C electrocatalysts in 1 M KOH; ν = 10 mV s^{-1}. (H) HER Tafel plots for TAL and Pt/C electrocatalysts in 1 M KOH. (I) HER polarization curves for TAL and Pt/C electrocatalysts in 0.5 M H_2SO_4; ν = 10 mV s^{-1}. (J) Alkaline single fuel cell test of TAL-2-900 and Pt/C. (K) Zinc–air battery testing with TAL-2-900, shows the voltage produced by two batteries, LED light using the same batteries, and (L) galvanostatic cycling of one battery for 8 h.

and TAL-2-1000 were 417 and 411 mV, respectively, indicating that the carbonization step at 900 °C was the optimal path to improve the electroactivity toward HER. In acidic media, the overpotential (η) was the smallest for TAL-2-900, while its overpotential was comparable to the values obtained for other Pt-free HER catalysts (Fig. 3I and Table S9, ESI†).

Finally, the performance of TAL-2-900 as catalyst material was evaluated in alkaline electrolyte membrane fuel cell and zinc–air battery. Alkaline membrane fuel cell test yielded current density up to 1100 mA cm^{-2} (Fig. 3J). Loading of the catalyst was kept at 2 mg cm^{-2} on GDL membrane modified with direct suspension pipetting. HMT-PMBI (hydroxide conducting membrane) was used as polymer electrolyte in both tests for Pt/C and TAL-2-900. Under similar conditions, TAL-2-900 showed 20% better activity than Pt/C. The value of power density for TAL-2-900 is >400 mW cm^{-2} leaving behind Pt/C 350 mW cm^{-2}. Similar results were recently reported using the same anion exchange membrane and an alternative Co–N–C material as a cathode catalyst.[53] Durability tests of poly(vinyl alcohol)-based solid-state zinc–air battery assembled using TAL-2-900 as an electrode material were performed by cycling at constant current density of 5.0 mA cm^{-2} (Fig. 3K). As expected from the ORR/OER data, TAL-2-900 catalyst-driven Zn–air battery delivered long cycle life over 8 h (Fig. 3L).

3. Conclusions

In conclusion, we have introduced a new materials preparation strategy by involving *amorphous not crystalline* MOFs, which were obtained from dihydroxybenzimidazole as a carbonaceous linker. Upon carbonization, it delivered a unique Co–N–C material, which simultaneously served as a heterogeneous catalyst for several organic transformations (incl. oxidation and homocoupling reactions) as well as an electrocatalyst material for ORR, OER and HER processes. This is the first example of an M–N–C catalyst being used for C(sp^3)–C(sp^3) carbon–carbon bond formation, and it was carried out in the presence of an organometallic reagent.

Author contributions

Kefeng Ping, Mahboob Alam: investigation, methodology, formal analysis, validation, writing – original draft; writing – review and editing; Sean Ray Kahnert, Rohit Bhadoria, Arvo Mere, Valdek Mikli, Maike Käärik, Jaan Aruväli, Päärn Paiste, Arvo Kikas, Vambola Kisand, Ivar Järving, Jaan Leis: investigation, methodology, formal analysis, writing – review and editing; Nadežda Kongi, Pavel Starkov: conceptualization, supervision, writing - original draft, writing – review and editing, funding acquisition.

Conflicts of interest

K. P., N. K. and P. S. are inventors on the PCT Appl. filed by the University of Tartu and Tallinn University of Technology.

Acknowledgements

This research was supported by Estonian Research Council (PSG250 and PUT1290) and TalTech Young Investigator Grant B62. We thank Prof. Steven Holdcroft (Simon Fraser University) for providing the HMT-PMBI membrane. The measurement facilities were supported by Institutional Research Grants IUT34-14 and TK141 (Advanced materials and high-technology devices for energy recuperation systems). K. P. acknowledges Estonian Smart Specialization PhD Fellowship. P. S. thanks COST Action CA18224 members (https://greenering.eu) for fruitful discussions.

Notes and references

1 Z. W. Seh, J. Kibsgaard, C. F. Dickens, I. Chorkendorff, J. K. Nørskov and T. F. Jaramillo, *Science*, 2017, **355**, eaad4998.
2 J. Masa, C. Andronescu and W. Schuhmann, *Angew. Chem., Int. Ed.*, 2020, **59**, 15298–15312.
3 A. Sarapuu, E. Kibena-Põldsepp, M. Borghei and K. Tammeveski, *J. Mater. Chem. A*, 2018, **6**, 776–804.
4 L. He, F. Weniger, H. Neumann and M. Beller, *Angew. Chem., Int. Ed.*, 2016, **55**, 12582–12594.
5 L. Liu and A. Corma, *Chem. Rev.*, 2018, **118**, 4981–5079.
6 M. B. Gawande, P. Fornasiero and R. Zbořil, *ACS Catal.*, 2020, **10**, 2231–2259.
7 H. B. Wu and X. W. Lou, *Sci. Adv.*, 2017, **3**, eaap9252.
8 P.-Q. Liao, J.-Q. Shen and J.-P. Zhang, *Coord. Chem. Rev.*, 2018, **373**, 22–48.
9 H. Yan, C. Su and J. He, *J. Mater. Chem. A*, 2018, **6**, 8793–8814.
10 S. Mitchell, E. Vorobyeva and J. Pérez–Ramírez, *Angew. Chem., Int. Ed.*, 2018, **57**, 15316–15329.
11 H.-F. Wang, L. Chen, H. Pang, S. Kaskel and Q. Xu, *Chem. Soc. Rev.*, 2020, **49**, 1414–1448.
12 X. F. Lu, B. Y. Xia, S.-Q. Zang and X. W. Lou, *Angew. Chem., Int. Ed.*, 2020, **59**, 4634–4650.
13 E. M. Miner, L. Wang and M. Dincă, *Chem. Sci.*, 2018, **9**, 6286–6291.
14 H. Zhong, K. H. Ly, M. Wang, Y. Krupskaya, X. Han, J. Zhang, J. Zhang, V. Kataev, B. Büchner, I. M. Weidinger, S. Kaskel, P. Liu, M. Chen, R. Dong and X. Feng, *Angew. Chem., Int. Ed.*, 2019, **58**, 10677–10682.
15 S. S. Shinde, C. H. Lee, J.-Y. Jung, N. K. Wagh, S.-H. Kim, D.-H. Kim, C. Lin, S. U. Lee and J.-H. Lee, *Energy Environ. Sci.*, 2019, **12**, 727–738.
16 M. Aygün, T. W. Chamberlain, M. C. Gimenez–Lopez and A. N. Khlobystov, *Adv. Funct. Mater.*, 2018, **28**, 1802869.
17 X.-J. Bai, X.-Y. Lu, R. Ju, H. Chen, L. Shao, X. Zhai, Y.-N. Li, F.-Q. Fan, Y. Fu and W. Qi, *Angew. Chem., Int. Ed.*, 2021, **60**, 701–705.
18 S. L. Zhang, B. Y. Guan and X. W. Lou, *Small*, 2019, **15**, 1805324.
19 X. P. Han, X. F. Ling, Y. Wang, T. Y. Ma, C. Zhong, W. B. Hu and Y. D. Deng, *Angew. Chem., Int. Ed.*, 2019, **58**, 5359–5364.
20 T. D. Bennett and A. K. Cheetham, *Acc. Chem. Res.*, 2014, **47**(5), 1555–1562.
21 T. D. Bennett and S. Horike, *Nat. Rev. Mater.*, 2018, **3**, 431–440.
22 K. Ping, A. Braschinsky, M. Alam, R. Bhadoria, V. Mikli, A. Mere, J. Aruväli, P. Paiste, S. Vlassov, M. Kook, M. Rähn, V. Sammelselg, K. Tammeveski, N. Kongi and P. Starkov, *ACS Appl. Energy Mater.*, 2020, **3**, 152–157.
23 K. Ping, M. Alam, M. Käärik, J. Leis, N. Kongi, I. Järving and P. Starkov, *Synlett*, 2019, 1536–1540.

24 D. Kong, Y. Gao, Z. Xiao, X. Xu, X. Li and L. Zhi, *Adv. Mater.*, 2019, **31**, 201804973.

25 S. Li, X. Hao, A. Abudula and G. Guan, *J. Mater. Chem. A*, 2019, **7**, 18674–18707.

26 W. Zhang, L. Cui and J. Liu, *J. Alloys Compd.*, 2020, **821**, 153542.

27 W. Liu, L. Zhang, X. Liu, X. Liu, X. Yang, S. Miao, W. Wang, A. Wang and T. Zhang, *J. Am. Chem. Soc.*, 2017, **139**, 10790–10798.

28 T. Song, Z. Ma, Y. Yuan, J. Xiao, Y. Yang and P. Ren, *ACS Catal.*, 2020, **10**, 4617–4629.

29 M. Nakanishi and C. Bolm, *Adv. Synth. Catal.*, 2007, **349**, 861–864.

30 Y. Li, S. Jie, K. Li and Z. Liu, *New J. Chem.*, 2018, **42**, 12677–12683.

31 P. Zhou, L. Jiang, F. Wang, K. Deng, K. Lv and Z. Zhang, *Sci. Adv.*, 2017, **3**, e1601945.

32 S. Yang, L. Peng, D. T. Sun, E. Oveisi, S. Bulut and W. L. Queen, *ChemSusChem*, 2018, **11**, 3131–3138.

33 F. Chen, A. Surkus, L. He, M. Pohl, J. Radnik, C. Topf, K. Junge and M. Beller, *J. Am. Chem. Soc.*, 2015, **137**, 11718–11724.

34 F. Chen, C. Kreyenschulte, J. Radnik, H. Lund, A. Surkus, K. Junge and M. Beller, *ACS Catal.*, 2017, **7**, 1526–1532.

35 R. V. Jagadeesh, K. Murugesan, A. S. Alshammari, H. Neumann, M. M. Pohl, J. Radnik and M. Beller, *Science*, 2017, **358**, 326–332.

36 R. Xie, F. Xie, C. J. Zhou, H. F. Jiang and M. Zhang, *J. Catal.*, 2019, **377**, 449–454.

37 F. Xie, R. Xie, J. X. Zhang, H. F. Jiang, L. Du and M. Zhang, *ACS Catal.*, 2017, **7**, 4780–4785.

38 H. Luo, L. Wang, S. Shang, G. Li, Y. Lv, S. Gao and W. Dai, *Angew. Chem., Int. Ed.*, 2020, **59**, 19268–19274.

39 Y. Zhou, Y. Chen, L. Cao, J. Lu and H. Jiang, *Chem. Commun.*, 2015, **151**, 8292–8295.

40 W. Zhong, H. Liu, C. Bai, S. Liao and Y. Li, *ACS Catal.*, 2015, **5**, 1850–1856.

41 L. Zhang, A. Wang, W. Wang, Y. Huang, X. Liu, S. Miao, J. Liu and T. Zhang, *ACS Catal.*, 2015, **5**, 6563–6572.

42 F. Xie, R. Xie, J. X. Zhang, H. F. Jiang, L. Du and M. Zhang, *ACS Catal.*, 2017, **7**, 4780–4785.

43 R. Xie, F. Xie, C. J. Zhou, H. F. Jiang and M. Zhang, *J. Catal.*, 2019, **377**, 449–454.

44 H. Gilman and R. G. Gorsich, *J. Am. Chem. Soc.*, 1955, **77**, 3134–3135.

45 R. A. Aitken, P. K. G. Hodgson, J. J. Morrison and A. O. J. Oyewale, *J. Chem. Soc., Perkin Trans. 1*, 2002, **3**, 402–415.

46 F. O. Ginah, T. A. Donovan Jr., S. D. Suchan, D. R. Pfennig and G. W. Ebert, *J. Org. Chem.*, 1990, **55**, 584–589.

47 S.-i. Inaba, H. Matsumoto and R. D. Rieke, *Tetrahedron Lett.*, 1982, **23**, 4215–4216.

48 K. Sato, Y. Inoue, T. Mori, A. Sakaue, A. Tarui, M. Omote, I. Kumadaki and A. Ando, *Org. Lett.*, 2014, **16**, 3756–3759.

49 V. V. Levin, D. P. Agababyan, M. I. Struchkova and A. D. Dilman, *Synthesis*, 2018, 2930–2935.

50 G. Park, S. Y. Yi, J. Jung, E. J. Cho and Y. You, *Chem. – Eur. J.*, 2016, **22**, 17790–17799.

51 R. Paul, F. Du, L. Dai, Y. Ding, Z. L. Wang, F. Wei and A. Roy, *Adv. Mater.*, 2019, **31**, 1805598.

52 S. Ghosh and R. N. Basu, *Nanoscale*, 2018, **10**, 11241–11280.

53 J. Lilloja, E. Kibena-Põldsepp, A. Sarapuu, M. Kodali, Y. Chen, T. Asset, M. Käärik, M. Merisalu, P. Paiste, J. Aruväli, A. Treshchalov, M. Rähn, J. Leis, V. Sammelselg, S. Holdcroft, P. Atanassov and K. Tammeveski, *ACS Appl. Energy Mater.*, 2020, **3**, 5375–5384.

Publication III

Ávila-Bolívar, B.; Cepitis, R.; Alam, M.; Assafrei, J.-M.; Ping, K.; Aruväli, J.; Kikas, A.; Kisand, V.; Vlassov, S.; Ivaništštev, V.; Starkov, P.; Montiel, V.; Solla-Gullón, J.; Kongi, N.

CO_2 reduction to formate on an affordable bismuth metal–organic framework based catalyst.

J. CO_2 Util. **2022,** *59,* 101937.

DOI:10.1016/j.jcou.2022.101937

Journal of CO2 Utilization 59 (2022) 101937

Contents lists available at ScienceDirect

Journal of CO2 Utilization

journal homepage: www.elsevier.com/locate/jcou

CO_2 reduction to formate on an affordable bismuth metal-organic framework based catalyst

Beatriz Ávila-Bolívar [a,1], Ritums Cepitis [b,1], Mahboob Alam [c], Jürgen-Martin Assafrei [b], Kefeng Ping [c], Jaan Aruväli [d], Arvo Kikas [e], Vambola Kisand [e], Sergei Vlassov [e], Maike Käärik [b], Jaan Leis [b], Vladislav Ivaništštev [b], Pavel Starkov [c], Vicente Montiel [a], José Solla-Gullón [a], Nadezda Kongi [b,*]

[a] *Institute of Electrochemistry, University of Alicante, E-03080 Alicante, Spain*
[b] *Institute of Chemistry, University of Tartu, 50411 Tartu, Estonia*
[c] *Department of Chemistry and Biotechnology, Tallinn University of Technology, 12618 Tallinn, Estonia*
[d] *Institute of Ecology and Earth Sciences, University of Tartu, 50411 Tartu, Estonia*
[e] *Institute of Physics, University of Tartu, 50411 Tartu, Estonia*

ARTICLE INFO

Keywords:
CO_2 electroreduction
Bismuth
Metal-organic framework
Formate
Formic acid

ABSTRACT

Electrochemical reduction of carbon dioxide (CO_2) into green fuels and valuable chemicals is an up-and-coming method of CO_2 valorization. Formate/formic acid is one the most desirable product among the many other possible chemicals that can be generated from CO_2. Herein, we report on a simple and tunable method to prepare Bi-based electrocatalyst. An affordable metal-organic framework (MOF) precursor TAL-33 has been utilized upon carbonization. This MOF was fabricated from a novel modular carbon-rich ligand 1*H*-benzo[*d*]imidazole-5,6-diol and bismuth chloride. Cyclic voltammetry and chronoamperometric measurements were performed to investigate the electrocatalytic activity and selectivity towards the formate. The most promising samples have shown high Faradaic efficiency and stability. The in-depth physical characterization of catalyst structure (XPS, XRD, SEM, and TEM) was performed to investigate the structure-activity relationships. Theoretical studies have been performed to confirm that the enhanced CO_2 electroreduction to formate is linked to the presence of metallic bismuth sites.

1. Introduction

Over the past century, human industrial development has led to the production of carbon dioxide (CO_2) at a higher rate than its consumption. The resulting rise in the concentration of CO_2 in the atmosphere is one of the primary drivers of global warming [1]. One of the more sustainable ways to solve this issue is through electrochemical reduction of CO_2 [2–4]. There are various products, which can be produced by CO_2 reduction, including methane, ethanol, methanol, and other high value products. One of the most reliable compounds is formic acid (HCOOH) or formate ($HCOO^-$) depending on pH value [5,6]. The formic acid/-formate market is expected to grow to one megaton per year by 2030 [6]. Formic acid and formate have various uses in medical, agricultural, and textile industries. Formic acid can also be used for energy production and storage devices, which can be used in hydrogen fuel cells [7,8]. The first catalysts used to reduce CO_2 to formic acid were rhodium-based catalysts, which exhibited a Faradaic efficiency (FE) of ca. 80% [9]. More recently, catalytic materials based on ruthenium have been implemented with the resultant FE values up to 95%, and the iridium-based materials exhibited FE values up to 97% [10]. Metals such as In, Pb, Hg, Sn and Bi are often reported to catalyze CO_2RR to formate with high selectivity, [11] among them tin and tin oxides are the most commonly used metals for electrocatalytic conversion of CO_2 to formic acid [11–13]. Typically, the combination of additional metal and/or nitrogen-doped carbon materials enhances the electrocatalytic performance of CO_2RR electrodes due to the increased conductivity and electrochemical accessibility of the surface area [14]. Often, bismuth-based composites exhibit highest selectivity, and good activity,

---

* Corresponding author.
E-mail address: nadezda.kongi@ut.ee (N. Kongi).

[1] Contributed equally to this work.

https://doi.org/10.1016/j.jcou.2022.101937
Received 24 October 2021; Received in revised form 25 January 2022; Accepted 14 February 2022

towards formate/formic acid [15,16]. In comparison, bismuth shows inferior activity for hydrogen evolution reaction (HER), meaning that the HER reaction does not interfere with CO_2 reduction reaction [17, 18].

Bismuth has recently gained popularity as a promising nontoxic electrocatalytic material for the production of formate/formic acid via the electroreduction of CO_2 [7,19]. In recent studies, several bismuth-based electrode configurations were implemented for the electrochemical conversion of CO_2. The examples include bismuth(0) particles synthesized on copper and titanium substrates [20], bismuth particles deposited onto the copper surface [21], oxide-derived bismuth films [22], carbon-supported bismuth nanoparticles [23], and bismuth nanosheets [24]. Zhong et al. [25] used nanostructured bismuth dendrite electrocatalysts, which were grown on a carbon paper and showed good performance in CO_2 reduction to formic acid with a Faradaic efficiency of 96.4% and a current density of 15.2 mA cm^{-2} at 1.8 V. In another study by Zhong et al. [24], BiOCl nanosheets were used in the electrochemical reduction of CO_2 into formic acid with FE of 92% and a current density of 3.7 mA mg^{-1} at $-$ 1.5 V. Due to their promising results, attention has focused on the electrochemical valorization of CO_2 to formate using a bismuth-based catalyst. However, further studies are needed to optimize the mass-transfer between the reactants and to explore sustainable ways of applying Bi-based electrocatalysts at the large scale.

Metal–organic frameworks (MOFs)-derived metal/carbon hybrids have demonstrated promising potential in electrochemical reactions because they might have intrinsic conductivity and activities [26–30]. Because of their high porosity and their large specific surface area, which are both highly beneficial for charge transfer, MOF-derived materials can be utilized as carbon-rich catalyst materials for the electrochemical reduction of CO_2 [31–33]. Often, the MOF precursors are combined with additional carbon and nitrogen sources to generate optimal amounts of the desired electroactive sites [34–37]. For instance, Zhang et al. applied in-situ electrochemical transformation strategy to prepare the bismuth nanosheet arrays from the bismuth-based metal organic framework CAU-17 ($Bi_9(C_9H_3O_6)_9(H_2O)_9$) supported on carbon cloth [34]. Hwang et al. combined Cu-based MOFs (Cu−benzene-1,3, 5-tricarboxylic acid) along with graphene oxide sheets to yield an efficient Cu-MOF/GO material with FE of 58% in 0.1 M tetrabutylammonium bromide /dimethylformamide [35]. Zhang et al. utilized bismuth single-site catalysts by thermal decomposition of Bi-MOF with dicyandiamide. Obtained Bi-N_4 sites on porous carbon networks promoted CO_2 electroreduction to CO with high turnover frequencies [36].

Herein, we report on the use of novel TAL-33 MOF as a single precursor for Bi-based catalyst material, which has excellent activity and selectivity towards formate production. The Bi-based electrocatalyst materials were synthesized from novel TAL-33 MOF precursor, and post-synthetic treatments of catalyst powders were optimized. Subsequently, electrochemical and morphological studies of the samples were conducted to compare the TAL-33-based catalytic materials carbonized at different temperatures. The catalytic mechanism was studied by comparing the morphological, structural, and electrochemical results. Observed selectivity of prepared Bi-based electrocatalysts was rationalized using DFT calculations.

2. Experimental part

2.1. Synthesis. Carbonization

TAL-33 MOF material was synthesized using 1 H-benzo[*d*]imidazole-5,6-diol linker and Bi-metal precursor ($BiCl_3$) (Fig. 1). Synthesis of 1 H-benzo[*d*]imidazole-5,6-diol was performed using an earlier published procedure [38]. $BiCl_3$ (3.15 g, 9.99 mmol, 1.0 equiv) was slowly added into a mixture of 1 H-benzo[*d*]imidazole-5,6-diol (3.00 g, 19.98 mmol, 2.0 equiv) in 25% aq. NH_3/DMF/EtOH/water (4:10:10:15), the resulting solution was left to stir at room temperature. After 24 h, suspension was filtered, washed with EtOH, and dried to give the desired material (4.98 g).

Bi-based materials were prepared by carbonizing the TAL-33 MOF at different temperatures (300 −700 °C) in a tube furnace, leading to five samples: TAL-33-300, TAL-33-400, TAL-33-500, TAL-33-600, and TAL-33-700. Carbonization of the material was done by applying a rapid heating process in a N_2 atmosphere. The material was placed into a ceramic boat, which was moved into the furnace tube after the specified temperature was reached. The temperature was kept constant for 2 h. After the heating, the heater was turned off and the material was left to cool down at room temperature.

2.2. Morphology studies

Powder X-ray diffraction (PXRD) measurements were performed on a Bruker D8 Advance instrument. The ICDD PDF-4 + database (2020) was used for qualitative analysis. Bruker Topas 6 software was used for the full profile analysis. The surface morphology of the material was examined using scanning electron microscopy (SEM) with FEI HR-SEM NanoSem 450. SEM samples were prepared by dissolving the powder material in isopropyl alcohol and then drop-coating a catalyst suspension onto polished GC plates. SEM data was acquired at 10 kV accelerating voltage using secondary electrons detector. The X-ray photoelectron spectroscopy (XPS) experiments were conducted at ultrahigh vacuum conditions with a non-monochromatic twin anode X-ray tube (Thermo XR3E2) which has the characteristic energy of 1253.6 eV (Mg K_α). The electron energy analyzer was SCIENTA SES 100. The data was processed by CasaXPS software (version 2.3.17). The obtained XPS spectra were averaged over the sample area. TEM images were taken using a JEOL JEM-1400 Plus microscope (JEOL, Akishima, Tokyo, Japan) working at 120 kV. The samples were dispersed in absolute ethanol, dropped onto a Lacey-covered copper grid and evaporated in the air at room temperature. Low-temperature nitrogen adsorption was done at the boiling temperature of nitrogen (77 K) by using the NovaTouch LX2 (Quantachrome Instruments) and the calculations were done with TouchWin 1.11 software (Quantachrome Instruments).

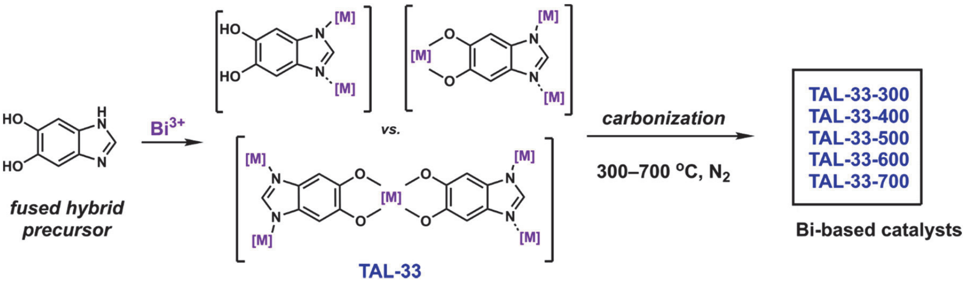

Fig. 1. Synthesis of Bi-based catalyst materials.

2.3. Electrochemical measurements

The catalytic ink, for application of catalyst onto the electrode surface, was made by dispersing the sample in a Nafion solution (perfluorosulfonic acid- PTFE copolymer 5% w/w solution, Alfa Aesar) at a catalyst: Nafion mass ratio of 80:20. The mixture was diluted 50-fold to 2% in absolute ethanol (EMSURE). An ultrasonic bath was used for homogenizing the ink for roughly 0.5 h. The cathode was prepared by air-brushing the ink on a 6 cm^2 Toray paper (TGPH-120, QuinTech) on a heated metallic plate at 90 °C for faster evaporation. The bismuth loading was 1 mg cm^{-2}.

The electrochemical activity of Bi-based materials was measured in a standard three-electrode configuration glass cell in a 0.45 M $KHCO_3$ (99.7% Sigma Aldrich) and 0.5 M KCl (99.5%, EMSURE) solution, saturated by CO_2 or Ar, using an AgCl/Ag (3.5 M KCl) as the reference electrode and a Pt wire as the counter electrode. The electrode potentials were referred to the reversible hydrogen electrode (RHE) scale according to the equation:

$$E_{\mathrm{RHE}} = E_{\mathrm{Ag/AgCl}} + 0.059\ \mathrm{pH} + E^{o}{}_{\mathrm{Ag/AgCl}}$$

where $E^{o}{}_{\mathrm{Ag/AgCl}}$= 0.205 at 25 °C, pH= 8.4 (corresponding to 0.45 M $KHCO_3$ and 0.5 M KCl solution), and $E_{\mathrm{Ag/AgCl}}$ is the applied potential against Ag/AgCl reference. Cyclic voltammetry was performed using PGSTAT302N (Metrohm Autolab B.V.). All cyclic voltammetry measurements were performed at room temperature (25 °C), and the currents were normalized by the geometric area of the electrodes. CO_2RR was performed in an H-type cell that has compartments divided by a cationic exchange membrane (Nafion 112). A 0.45 M $KHCO_3$ and 0.5 M KCl solution saturated with CO_2 was used as a catholyte. A 1.0 M KOH (85% Panreac) solution was used as anolyte. The cation exchange membrane was activated in 0.1 M NaOH solution for 24 h. A nickel mesh immersed in the anolyte was used as a counter electrode, and AgCl/Ag placed in the catholyte was utilized as a reference electrode. The CO_2RR was carried out by chronoamperometry measurements at a controlled potential of − 1.0 V vs. RHE for 1.5 h using the same PGSTAT302N. The reduction of CO_2 into formate was followed by ionic chromatography (883 Basic IC plus, Metrohm), with a conductivity up to 15000 μS cm^{-1}. The mobile phase consisted of 1.8 mM Na_2CO_3 and 1.7 mM $NaHCO_3$ solution. The calibration curve was carried out from 0 to 30 ppm in a solution of 0.0045 M $KHCO_3$ and 0.005 M KCl (corresponding with a 100 times dilution of the catholyte). The gaseous compounds were analysed by gas chromatography using a GC, Hewlett Packard HP 5890 Series II coupled to a thermal conductivity detector (TCD). The gaseous compounds were collected from the sealed cathodic compartment during the electrolyses in a Tedlar Bag (1 liter). Previous calibration was carried out with pure gaseous samples of O_2, N_2, CO, H_2 and CO_2.

2.4. DFT calculation method

For computational models, bismuth (111) surface, BiN_4, and BiN_2 with nitrogens in *cis* and *trans* arrangements were used, as shown in Fig. 2. The Metal-N-C structures used in the electronic structure calculations were taken from previous studies and optimized for bismuth metal centers.

Electronic structure calculations were performed using GPAW software [39] using the RPBE functional [40]. In all calculations (2 ×2 ×1) *k*-point sampling, grid spacing of 0.18, at least 14 Å vacuum layer, and force minimization below 0.01 eV/Å were used. Geometric structures were optimized until no imaginary vibration frequencies for the adsorbate were observed. The obtained frequencies were further used to calculate energy corrections from zero-point energy, heat capacity, and entropy within harmonic approximation. Solvation effects were included by shifting solvated species with an OH group by − 0.30 eV [41]. Dispersion correction was applied using the D4 method [42]. In the gas-phase calculation of CO_2, further correction by 0.45 eV was applied to account for systematic error in RPBE functional [43]. The energy for concerted proton-electron transfer steps was calculated employing a computational hydrogen electrode [44].

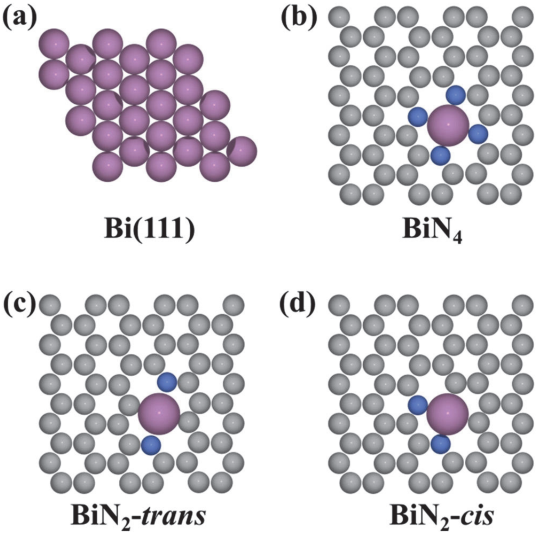

Fig. 2. Top view on models used in calculations – (a) bismuth (111) surface and (b, c, d) Bi-N-C structures.

3. Results and discussion

3.1. Electrochemical characterization

To initially evaluate the electrochemical properties of the samples, cyclic voltammetry and chronoamperometry studies were performed. Fig. 3 shows the voltammetric responses of the different samples in the Ar and CO_2 saturated solution. The reduction of Bi oxide occurs at about − 0.05 V vs. RHE, whereas the CO_2 electroreduction appears at about − 0.7 V vs. RHE [45]. However, interestingly, the activity of the samples is remarkably affected by the carbonizing temperature and samples carbonized at 400–600 °C display much better activity than those carbonized at 300 and 700 °C. Also, in Fig. S1, the comparison among the different catalysts both in Ar and CO_2-saturated solution is reported.

To better study the electrocatalytic properties of the samples towards CO_2 electroreduction, chronoamperometry measurements were performed in an H-type cell at − 1.0 V vs. RHE for 1.5 h. The faradaic efficiency towards the formate was calculated using the following eq.:

$$\mathrm{FE} = nNF/Q$$

Where n is the number of moles of the formate, N represents the number of electrons transferred from CO_2 to produce one molecule of formate in the reaction (= 2), F is the Faradaic constant (= 96,485 C mol^{-1}) and Q is the charge passed through the working electrode (calculated from the current produced in the chronoamperometry measurement). GC analyses of the gas products indicate that hydrogen was the only subproduct detected. Fig. 4a shows the variation of current density versus time at constant potential for every sample. The results indicate that currents remain rather stable during 1.5 h. The current density values were similar to those reported in previous studies [46]. Fig. 4b reports FE values towards formate for the different samples after 1.5 h. The results evidence that, in agreement with the voltammetric results (Fig. 3), the behavior of the samples is determined by the carbonizing temperature and samples treated at 400–600 °C display a high selectivity towards the

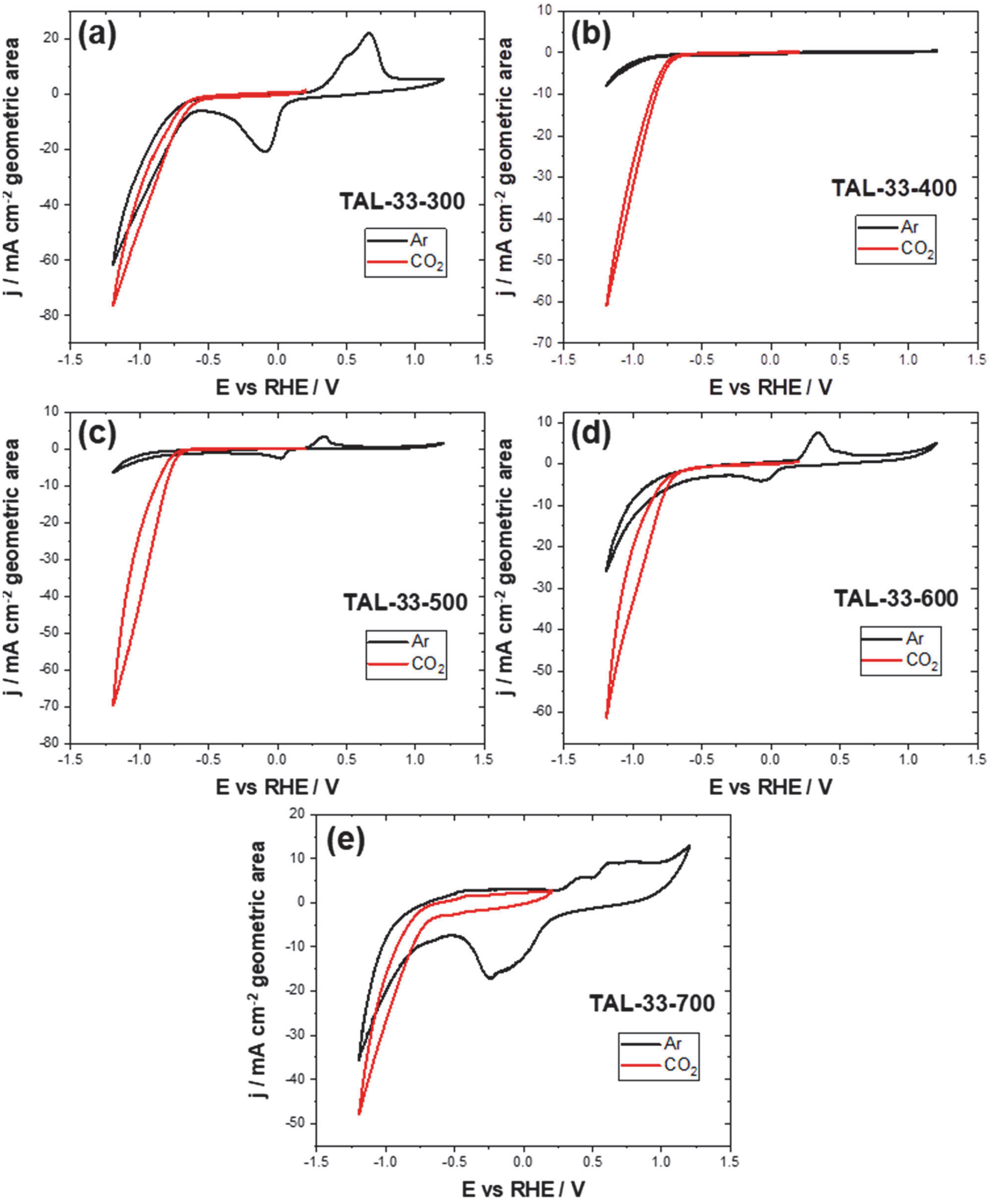

Fig. 3. Cyclic voltammetry response in Ar (black line) and CO_2 (red line) saturated 0.45 M $KHCO_3$ and 0.5 M KCl solution of (a) TAL-33-300, (b) TAL-33-400, (c) TAL-33-500, (d) TAL-33-600, and (e) TAL-33-700. Scan rate 50 mV s^{-1}.

production of formate. In particular, the sample treated at 600 °C displays the best FE and reaches a value close to 100%. However, for carbonizing temperatures higher than 600 °C, the FE decreases to values about 70%. FE values above 95% are promising, with most current catalytic materials falling below that efficiency [47]. Detailed values of current density and formate faradaic efficiency are shown in the Table S1. From these results, it can be assumed that the TAL-33-600 sample has the highest activity for CO_2RR with the highest efficiency out of the measured samples.

To complete this electrochemical study, chronoamperometry measurements were also carried out at − 1.0 V vs RHE for 4 h with TAL-33-based samples to preliminary testing their stability under working

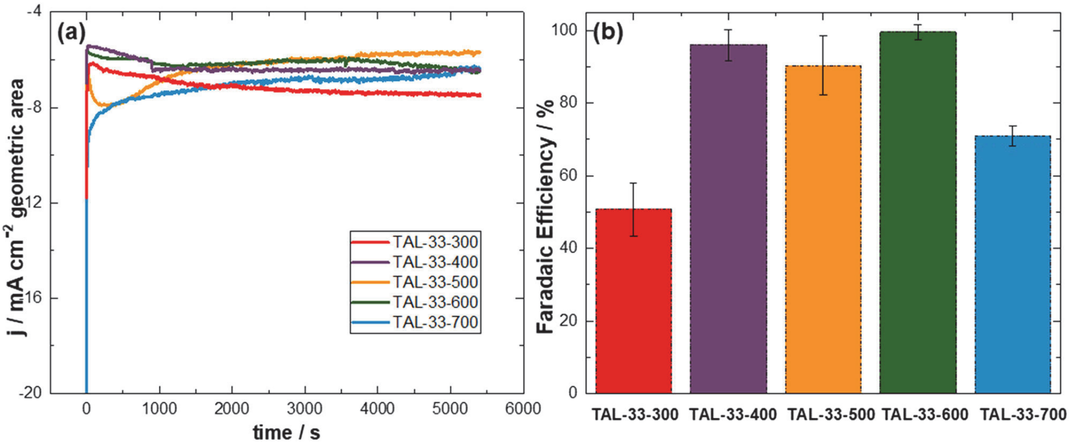

Fig. 4. (a) Chronoamperometric measurements at − 1.0 V vs RHE for 1.5 h with different samples. (b) Formate Faradaic efficiency for 1.5 h.

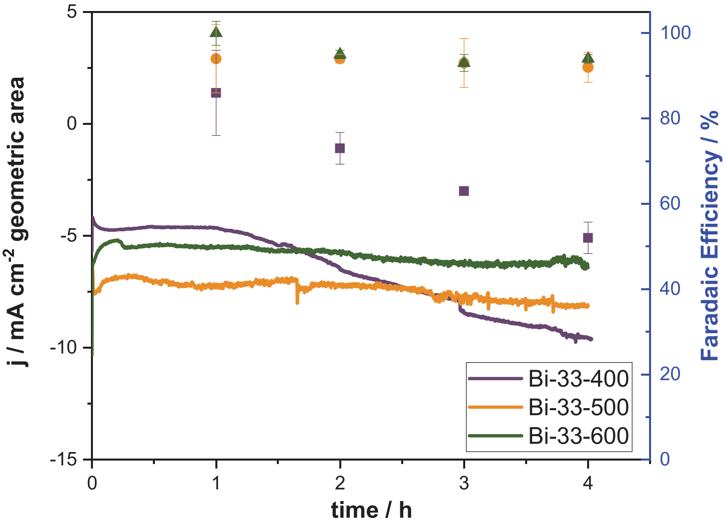

Fig. 5. Stability chronoamperometric measurements at − 1.0 V vs RHE and formate faradaic efficiency for 4 h.

conditions. Fig. 5 shows the current density and the Faradaic efficiency results during these 4 h. The results indicate that, for the TAL-33-400 sample, the formate FE significantly decreased after 4 h of CO_2RR. However, samples carbonized at 500 and 600 °C display much better stability and the resulting FE values show a decrease of only 6–8% after 4 h, remarkably less than the other samples. The stability of these samples is similar to values for previously established catalysts [4,46]. Also, the formate FE values are promising with a valued of 92–94% for TAL-33-500 and TAL-33-600 after 4 h. These numerical values are also displayed in Table S2.

3.2. *Morphology studies*

The porosity data collected from the analysis of N_2 adsorption-desorption isotherms are summarized in Table S3. The highest surface area (S_a) was observed with TAL-33-600 (123 m^2 g^{-1}), followed by TAL-33-800 (109 m^2 g^{-1}), which can be another indicator of the importance of optimized carbonization. Results of total volume (V_{tot}) calculations correlate with S_a values among the carbonized TAL-33-derived samples, with **TAL-33-600** having the highest total volume (0.16 cm^3 g^{-1}). Obtained results were in agreement with electrochemical capacitance behavior, which clearly indicated that the surface area of the samples increases with the increasing annealing temperatures (Fig. S2).

To investigate the structural features of TAL-33 derived materials, and to understand the structure versus electrochemical activity and stability of prepared Bi-based catalysts, XRD and XPS analyses were conducted. XRD data confirms the presence of amorphous carbon material and bismuth in all carbonized samples. Two sharp peaks at 38° and 40° in XRD patterns (Fig. 6a) indicate the presence of metallic bismuth in samples carbonized at 400–600 °C. To investigate the surface chemical state of the most active samples (TAL-33-400, TAL-33-500, TAL-33-600), XPS measurements were carried out. The survey spectra in Fig. 6b of the three samples show that all the materials consist of Bi, C, O, and N elements, and that their average concentrations are similar.

Table 1 summarizes the surface elemental composition for Bi, C, O and N. The atomic concentration of bismuth on the surface of catalyst

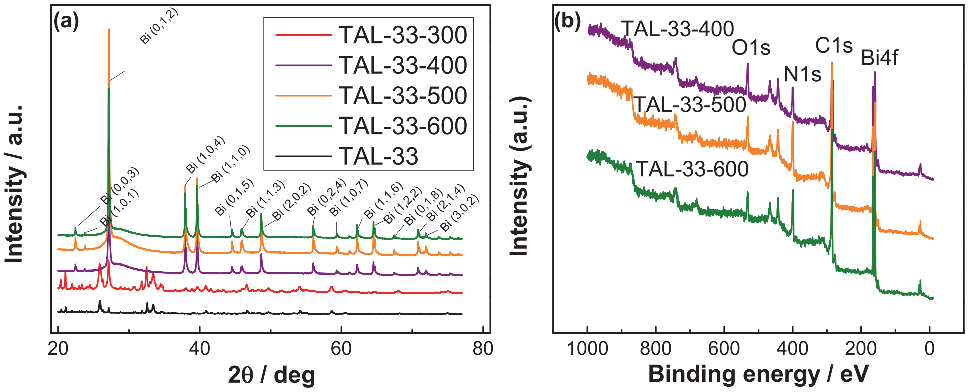

Fig. 6. (a) XRD patterns and (b) XPS survey spectra of the TAL-33-derived Bi-based materials.

Table 1
Surface elemental composition of the three primary samples determined by XPS.

Catalyst	Surface elemental composition (at%)			
	Bi	C	N	O
TAL-33-400	2.6	70.2	15.3	11.9
TAL-33-500	2.3	67.9	20.3	9.6
TAL-33-600	2.4	71.5	18.5	7.7

materials is relatively equal for all the samples, while the concentration of oxygen, carbon, and nitrogen varies with carbonization temperature. A trend can be observed for concentrations of oxygen – as it decreases with increased carbonization temperature. In contrast, the carbon and nitrogen atomic concentrations do not show any apparent shift.

High-resolution XPS spectra of the Bi 4 f region (Fig. 7) has peaks at binding energies of 159 eV and 165 eV, which correspond to Bi 4 $f_{7/2}$ and Bi 4 $f_{5/2}$. This indicates that a large portion of bismuth has an oxidation state of + 3, suggesting the possibility of an oxide layer formation. According to high-resolution XPS data bismuth particles in all samples have the same oxidation state (Table S4).

The fitted O 1 s spectra in Fig. 8 consists of the following oxygen species: O=C-OH, C=O, C-O, C-OH and water along with chemisorbed oxygen. The occurrence of bismuth oxide could have slight beneficial properties to the charge transfer because the oxide layer inhibits the HER reaction [48]. In recent contribution by Deng et al. electrochemical results on MOF-derived Bi catalysts also demonstrated that the Bi_2O_3 is beneficial for improving the reaction kinetics and selectivity to formate [49]. Summarized data on relative oxygen content can be seen in Table S5.

High resolution C 1 s spectra consist of the following peaks: sp^2, sp^3, carbide, C–O, C=O, and π–π * (Fig. S3). These show the bonds found in the carbon backbone of the Bi-based material. The carbide peak is much larger in TAL-33-400 than in the other samples, which means that in samples TAL-33-500 and TAL-33-600, the bismuth particles did not form as many bonds with the carbon backbone as the TAL-33-400 sample. From Table S6, the TAL-33-600 sample has a high amount of sp^3 carbon, which has been previously shown to be beneficial for reducing CO_2 into formate. According to previous speculations, the synergy of carbon matrix and Bi_2O_3 moieties may synergistically increase the abundant active sites (enhancing intrinsic activity), thus causing excellent charge-transfer behavior [49].

The high-resolution N 1 s spectra consist of peaks corresponding to NO, bulk N-h, graphitic-N, pyrrolic-N, imine, pyridinic-N, and metal-N_x species (Fig. S4). Relative concentrations of different nitrogen species found in the samples can be seen in Table 2. The most significant observation is that the amount of metal-N_x decreases with increasing temperature, TAL-33-400 sample has the highest concentration of the metal-N_x sites. This indicates that in samples TAL-33-400 and TAL-33-500, the Bi particles form much more coordinate bonds with nitrogen than in the TAL-33-600 sample, correlating to the observed increase in activity with increase in metallic bismuth concentration.

In summary, the morphological data shows that samples TAL-33-400 and TAL-33-600, which had high activity and selectivity, had high amounts of oxide in the sample, thus inhibiting the competing HER reaction. TAL-33-600 also had a high amount of sp^3 carbon, which was beneficial for the CO_2RR reaction. Notable amounts of sp^2 carbon, which most probably was responsible for the side reactions that occurred at the beginning of the measurement. The XPS data also indicates that the TAL-33-600 sample has less bonds between bismuth and carbon/nitrogen. According to the XPS and XRD data, higher amounts of metallic bismuth in the lattice, sufficient amounts of bismuth oxide, and sp^3 carbon led to a more efficient CO_2RR reaction and higher FE of CO_2 electroreduction

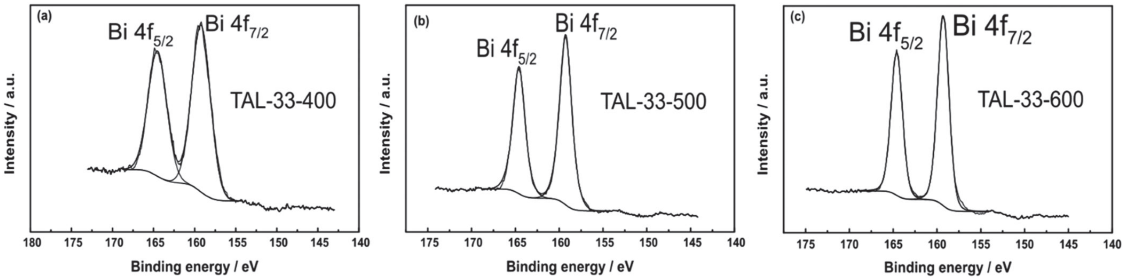

Fig. 7. High-resolution Bi 4 f spectra of (a) TAL-33-400, (b) TAL-33-500, and (c) TAL-33-600 samples.

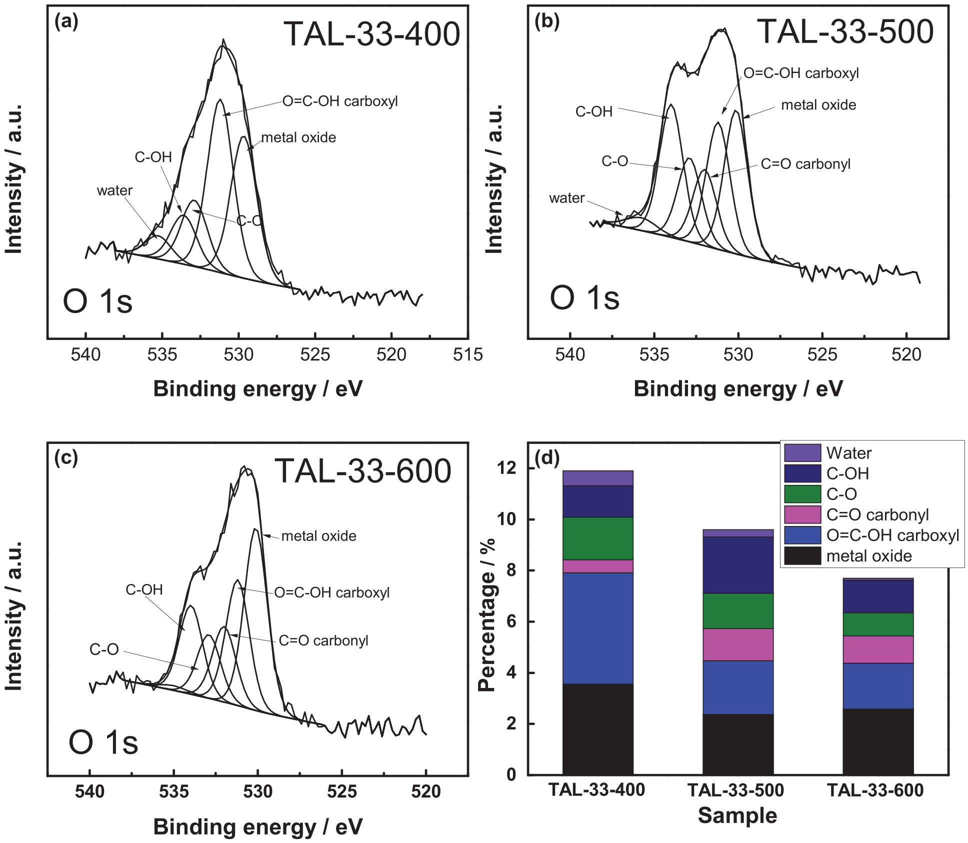

Fig. 8. High-resolution O 1 s spectra of (a) TAL-33-400, (b) TAL-33-500, and (c) TAL-33-600 samples; (d) O 1 s state composition histogram.

Table 2
The relative content of nitrogen species at the surface of TAL-33-derived samples.

Catalyst	N total (%)	Imine (%)	Pyridinic-N (%)	Metal-N$_X$ (%)	Pyrrolic (%)	Graphitic (%)	NO (%)	Bulk N-h (%)
TAL-33-400	15.4	19.1	9.2	33.7	27.0	7.6	1.2	2.2
TAL-33-500	20.3	0.0	40.7	17.0	31.5	6.6	1.7	2.5
TAL-33-600	18.5	0.3	46.6	7.6	32.5	7.5	2.0	3.5

to formate.

3.3. Microscopic imaging

To investigate the surface morphology of the materials and to understand the difference in electrocatalytic behavior, TEM and SEM analysis of the samples carbonized at different temperatures were conducted. According to SEM observations (Fig. 9), samples carbonized at 300 °C consist of a mixture of larger (in order of 1–10 μm) porous flakes and smaller (sub-μm) irregularly-shaped structures. Rounded particles can be seen in the image of the TAL-33-400 sample carbonized at 400 °C. Particles are partly embedded into bigger flakes and have rough surface. The size of the particles is ranging from few hundred to several hundreds of nm. At 500 °C particles are bigger (up to two μm) and appear more separated from flakes, but still have rough irregular surfaces. For TAL-33–600 carbonized at 600 °C, clearly separated particles can be seen everywhere on the samples. Compared to lower temperatures, particles at 600 °C are even bigger and have smooth surfaces with facets. The improvement of the SEM image quality can also be noticed, indicating than conductivity of the samples has been increased probably due to the complete separation of particles from carbon matrix. Further increase in temperature lead to sintering of Bi particles into bigger structures.

TEM images in Fig. 10a indicate that after carbonization at 400 °C, bismuth existed predominantly in amorphous form. Fig. 10b, the TEM images indicate the beginning of Bi nucleation and crystallization. The carbonization of samples at 600 °C resulted in the formation of clearly crystallized structures of Bi metallic nanoparticles (Fig. 10c). Inset in Fig. 10c shows a homogeneous distribution of spherical Bi nanoparticles with an average size of 25 ± 8 nm. The SEM and TEM analysis further prove the nucleation and formation of metallic Bi nanoparticles with increasing carbonization temperature (Fig. S5 and S6).

3.4. DFT calculations results

Experimental studies have shown that under experimental

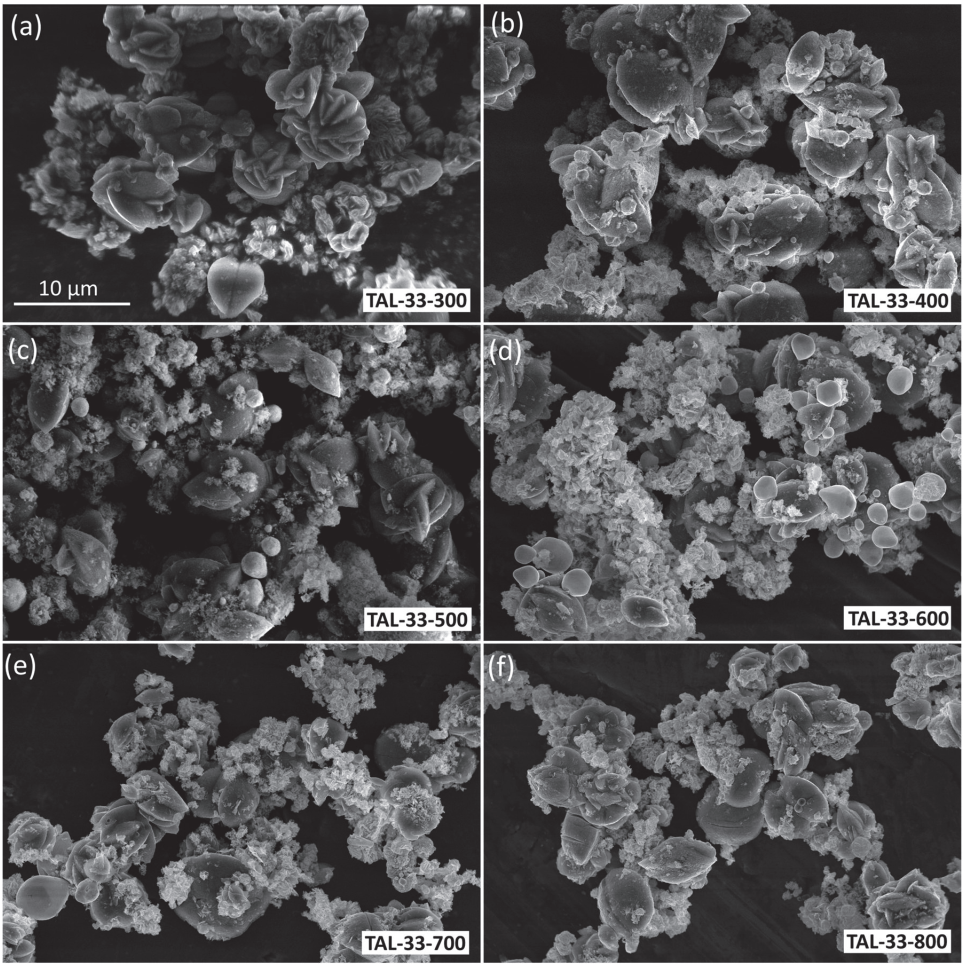

Fig. 9. SEM images of the TAL-33-derived samples carbonized at different temperatures. All images were made with the same magnification (x10000).

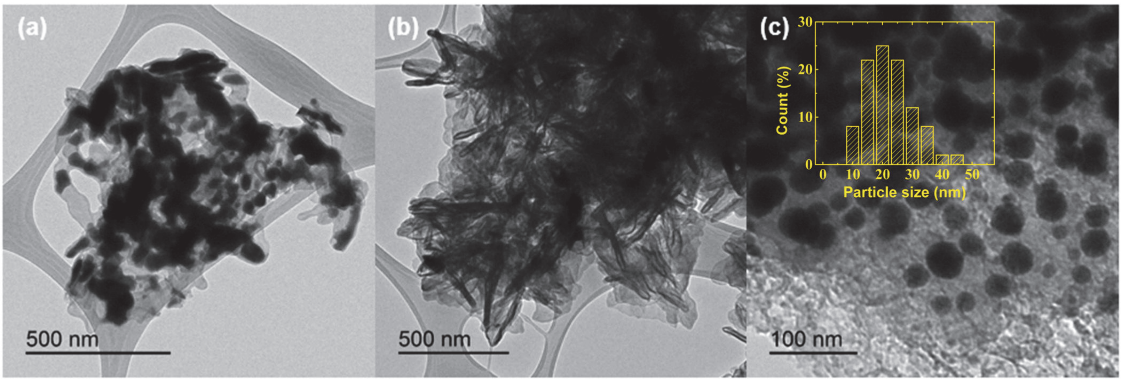

Fig. 10. (a) TEM images of TAL-33-400, (b) TAL-33-500 and (c) TAL-33-600 materials.

conditions bismuth oxide undergoes reduction to pure metal [45] which displays selectivity towards HCOOH formation [50]. To confirm the positive effect of metallic Bi on CO_2 selective electroreduction to formic acid and to contrast it to the selectivity on coexisting Metal-N-C structures, density functional theory (DFT) calculations were performed. Bi (111) surface was chosen to model reaction pathways on bismuth metal, as it is the most stable bismuth surface and the most common cleavage plane [50–52]. Three main pathways that can occur on bismuth surfaces were investigated [47] – CO_2 reduction to CO or HCOOH and the competing hydrogen evolution reaction (HER). For each of the pathways, energy of each intermediate structure was calculated, and the highest energy barrier (limiting potential) for each pathway was found and used to describe the observed selectivity in our catalyst.

The results obtained in terms of limiting potentials for different calculated species for each pathway are summarized in Table 3. From the calculations, it can be found that *cis*-BiN_2 is predicted to show the best activity towards HCOOH formation. However, our calculations indicate that the formation energy of *cis*-BiN_2 is less favorable than that of *trans*-BiN_2 (see Table S7). Hence, it is unlikely for it to be present in our catalyst in significant concentrations. Therefore, the observed activity and selectivity is attributed to the Bi(111) surface, hence confirming the experimental observation that the TAL-33-600 sample which contains most metallic bismuth is the best-performing.

In addition to the excellent Bi(111) activity and selectivity, it can be observed that the limiting potential for HER is noticeably higher than for the respective HCOOH and CO pathways, thus corroborating our observation that HER is not a significant side reaction for any of the samples.

To further explain the different observed selectivity for HCOOH formation on Bi(111) surface and contrast it to the CO formation on BiN_4, free energy diagrams were plotted for all involved states in CO and HCOOH formation as shown in Fig. 11. The selectivity for the HCOOH formation was highly dependent on the adsorption strength of the *OCHO intermediate. This is best visible for the BiN_4 that binds the intermediate too strongly, resulting in the high potential required to produce HCOOH in the second step. Furthermore, the strong adsorption of *OCHO intermediate over time poisons the site, since the second reduction step to yield HCOOH has a very high reaction barrier (0.95 eV). This allows us to explain the observed Faradaic efficiency drop with time in the TAL-33-400 sample, which (as shown from morphological studies) contains the most metal-N_x sites.

4. Summary

In this work, the Bi-based electrocatalysts were fabricated by an optimized carbonization of TAL-33 MOF material. The prepared catalysts have exhibited promising results in the CO_2RR by conversion to formate. The bismuth MOF-based materials' structure, composition and morphology were analyzed by scanning and transmission electron, X-ray diffraction and X-ray photoelectron spectroscopies. Additionally, electrocatalytic activity and stability of the bismuth MOF-based catalysts in CO_2 electroreduction were investigated in the $KHCO_3$ solution by using cycling voltammetry and potentiometric measurements. Overall, five different samples were optimized (across the carbonization temperatures 300–700 °C), and the obtained FE values varied between 51% and 100% upon 1.5 h of testing. The sample carbonized at 600 °C delivered the highest efficiency and stability, with a loss of only 6% of FE after 4 h. With the TAL-33-600 sample reaching FE of 100%, HER played a minor role during the reaction, and only CO_2RR occurred in the cell. According to the surface morphological investigations, the TAL-33-600 sample showed the highest activity because at this temperature the bismuth nanoparticles were formed. SEM and TEM measurements indicate that the formation of bismuth(0) is important to achieve high CO_2 conversions. The DFT calculations have also confirmed these results.

Table 3

Calculated limiting potentials (eV) towards HER and CO_2RR to HCOOH and CO.

Model / Product	H_2	HCOOH	CO
BiN_4	0.69	0.95	0.55
***trans*-BiN_2**	1.52	0.94	1.51
***cis*-BiN_2**	1.04	0.23	1.00
Bi(111)	1.19	0.37	0.99

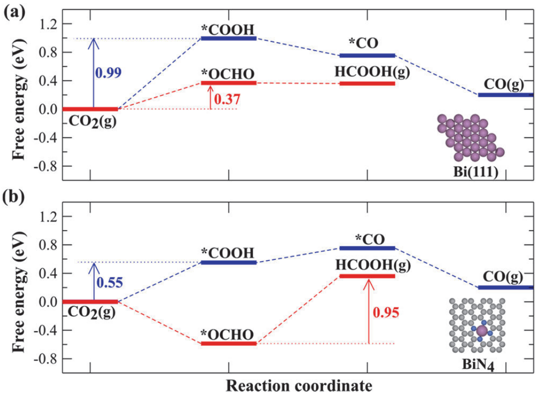

Fig. 11. Free energy diagrams for HCOOH and CO formation on (a) Bi(111) and (b) BiN_4. In blue color is shown CO pathway, while in red color is shown HCOOH pathway. Starred species denote surface adsorbates.

CRediT authorship contribution statement

Beatriz Ávila-Bolívar: Methodology, Investigation, Formal analysis. **Vicente Montiel:** Investgation. **Jürgen-Martin Assafrei:** Formal analysis, Writing. **Kefeng Ping:** Methodology. **Mahboob Alam:** Methodology. **Sergei Vlassov:** Investigation, Methodology. **Maike Käärik:** Analysis. **Jaan Leis:** Analysis. **Jaan Aruväli:** Investigation, Methodology, Formal analysis. **Arvo Kikas:** Analysis. **Vambola Kisand:** Investigation, Formal analysis. **Ritums Cepitis:** Writing, Formal Analysis, Investigation. **Vladislav Ivaniststev:** Conceptualization. **Pavel Starkov:** Conceptualization, Investigation. **José Solla-Gullón:** Conceptualization, Writing - Original Draft. **Nadezda Kongi:** Conceptualization, Writing - Original Draft, Funding acquisition.

Declaration of Competing Interest

The authors declare that they have no known competing financial interests or personal relationships that could have appeared to influence the work reported in this paper.

Acknowledgements

This research was supported by Estonian Research Council grant PSG250; EU through the European Regional Development Fund, Estonia (TK141, “Advanced materials and high-technology devices for energy recuperation systems” and TK143, “Molecular Cell Engineering”); Environmental Investment Center circular economy program (KIK18070). A.B, V. M. and J.S.G. acknowledge the financial support of the Ministerio de Ciencia e Innovación-FEDER (Spain) through the project PID2019-108136RB-C32 and Generalitat Valenciana (Project PROMETEO/2020/063). S.V. acknowledges the financial support of ERA Chair MATTER from the European Union’s Horizon 2020, Estonia research and innovation programme under grant agreement No 856705.

Appendix A. Supporting information

Supplementary data associated with this article can be found in the online version at doi:10.1016/j.jcou.2022.101937.

References

[1] P. Friedlingstein, M. O'Sullivan, M.W. Jones, R.M. Andrew, J. Hauck, A. Olsen, G. P. Peters, W. Peters, J. Pongratz, S. Sitch, C. Le Quéré, J.G. Canadell, P. Ciais, R. B. Jackson, S. Alin, L.E.O.C. Aragão, A. Arneth, V. Arora, N.R. Bates, M. Becker, A. Benoit-Cattin, H.C. Bittig, L. Bopp, S. Bultan, N. Chandra, F. Chevallier, L. P. Chini, W. Evans, L. Florentie, P.M. Forster, T. Gasser, M. Gehlen, D. Gilfillan, T. Gkritzalis, L. Gregor, N. Gruber, I. Harris, K. Hartung, V. Haverd, R.A. Houghton, T. Ilyina, A.K. Jain, E. Joetzjer, K. Kadono, E. Kato, V. Kitidis, J.I. Korsbakken, P. Landschützer, N. Lefèvre, A. Lenton, S. Lienert, Z. Liu, D. Lombardozzi, G. Marland, N. Metzl, D.R. Munro, J.E.M.S. Nabel, S.-I. Nakaoka, Y. Niwa, K. O'Brien, T. Ono, P.I. Palmer, D. Pierrot, B. Poulter, L. Resplandy, E. Robertson, C. Rödenbeck, J. Schwinger, R. Séférian, I. Skjelvan, A.J.P. Smith, A.J. Sutton, T. Tanhua, P.P. Tans, H. Tian, B. Tilbrook, G. van der Werf, N. Vuichard, A. P. Walker, R. Wanninkhof, A.J. Watson, D. Willis, A.J. Wiltshire, W. Yuan, X. Yue, S. Zaehle, Global carbon budget 2020, Earth Syst. Sci. Data 12 (2020) 3269–3340, https://doi.org/10.5194/essd-12-3269-2020.

[2] L.D. Ramírez-Valencia, E. Bailón-García, F. Carrasco-Marín, A.F. Pérez-Cadenas, From CO_2 to value-added products: a review about carbon-based materials for electro-chemical CO_2 conversion, Catalysts 11 (2021) 351, https://doi.org/10.3390/catal11030351.

[3] G. Wang, J. Chen, Y. Ding, P. Cai, L. Yi, Y. Li, C. Tu, Y. Hou, Z. Wen, L. Dai, Electrocatalysis for CO_2 conversion: from fundamentals to value-added products, Chem. Soc. Rev. 50 (2021) 4993–5061, https://doi.org/10.1039/D0CS00071J.

[4] S. Park, D.T. Wijaya, J. Na, C.W. Lee, Towards the large-scale electrochemical reduction of carbon dioxide, Catalysts 11 (2021) 253, https://doi.org/10.3390/catal11020253.

[5] M. Alfath, C.W. Lee, Recent advances in the catalyst design and mass transport control for the electrochemical reduction of carbon dioxide to formate, Catalysts 10 (2020) 859, https://doi.org/10.3390/catal10080859.

[6] M. Rumayor, A. Dominguez-Ramos, P. Perez, A. Irabien, A techno-economic evaluation approach to the electrochemical reduction of CO_2 for formic acid manufacture, J. CO2 Util. 34 (2019) 490–499, https://doi.org/10.1016/j.jcou.2019.07.024.

[7] J. Albo, M. Alvarez-Guerra, P. Castaño, A. Irabien, Towards the electrochemical conversion of carbon dioxide into methanol, Green Chem. (2015) 21, https://doi.org/10.1039/C4GC02453B.

[8] B. Loges, A. Boddien, F. Gärtner, H. Junge, M. Beller, Catalytic generation of hydrogen from formic acid and its derivatives: useful hydrogen storage materials, Top. Catal. 53 (2010) 902–914, https://doi.org/10.1007/s11244-010-9522-8.

[9] C.M. Bolinger, N. Story, B.P. Sullivan, T.J. Meyer, Electrocatalytic reduction of carbon dioxide by 2,2'-bipyridine complexes of rhodium and iridium, Inorg. Chem. 27 (1988) 4582–4587, https://doi.org/10.1021/ic00298a016.

[10] P. Ding, H. Zhao, T. Li, Y. Luo, G. Fan, G. Chen, S. Gao, X. Shi, S. Lu, X. Sun, Metal-based electrocatalytic conversion of CO_2 to formic acid/formate, J. Mater. Chem. A 8 (2020) 21947–21960, https://doi.org/10.1039/D0TA08393C.

[11] A. Liu, M. Gao, X. Ren, F. Meng, Y. Yang, L. Gao, Q. Yang, T. Ma, Current progress in electrocatalytic carbon dioxide reduction to fuels on heterogeneous catalysts, J. Mater. Chem. A 8 (2020) 3541–3562, https://doi.org/10.1039/C9TA11966C.

[12] M.F. Philips, G.-J.M. Gruter, M.T.M. Koper, K.J.P. Schouten, Optimizing the electrochemical reduction of CO_2 to formate: a state-of-the-art analysis, ACS Sustain. Chem. Eng. 8 (2020) 15430–15444, https://doi.org/10.1021/acssuschemeng.0c05215.

[13] J. Wu, X. Bai, Z. Ren, S. Du, Z. Song, L. Zhao, B. Liu, G. Wang, H. Fu, Multivalent Sn species synergistically favours the CO_2-into-HCOOH conversion, Nano Res. 14 (2021) 1053–1060, https://doi.org/10.1007/s12274-020-3149-2.

[14] S. Zhao, S. Li, T. Guo, S. Zhang, J. Wang, Y. Wu, Y. Chen, Advances in Sn-based catalysts for electrochemical CO_2 reduction, Nano Micro Lett. 11 (2019) 62, https://doi.org/10.1007/s40820-019-0293-x.

[15] G. Díaz-Sainz, M. Alvarez-Guerra, B. Ávila-Bolívar, J. Solla-Gullón, V. Montiel, A. Irabien, Improving trade-offs in the figures of merit of gas-phase single-pass continuous CO_2 electrocatalytic reduction to formate, Chem. Eng. J. 405 (2021), 126965, https://doi.org/10.1016/j.cej.2020.126965.

[16] H. Jiang, L. Wang, Y. Li, B. Gao, Y. Guo, C. Yan, M. Zhuo, H. Wang, S. Zhao, High-selectivity electrochemical CO_2 reduction to formate at low overpotential over Bi catalyst with hexagonal sheet structure, Appl. Surf. Sci. 541 (2021), 148577, https://doi.org/10.1016/j.apsusc.2020.148577.

[17] Y. Li, J. Chen, P. Cai, Z. Wen, An electrochemically neutralized energy-assisted low-cost acid-alkaline electrolyzer for energy-saving electrolysis hydrogen generation, J. Mater. Chem. A 6 (2018) 4948–4954, https://doi.org/10.1039/C7TA10374C.

[18] J. Greeley, T.F. Jaramillo, J. Bonde, I. Chorkendorff, J.K. Nørskov, Computational high-throughput screening of electrocatalytic materials for hydrogen evolution, Nat. Mater. 5 (2006) 909–913, https://doi.org/10.1038/nmat1752.

[19] J. Liu, Y. Li, Y. Wang, C. Xiao, M. Liu, X. Zhou, H. Jiang, C. Li, Isolated ultrasmall Bi nanosheets for efficient CO_2-to-formate electroreduction, Nano Res. 15 (2022) 1409–1414, https://doi.org/10.1007/s12274-021-3677-4.

[20] E. Bertin, S. Garbarino, C. Roy, S. Kazemi, D. Guay, Selective electroreduction of CO 2 to formate on Bi and oxide-derived Bi films, J. CO2 Util. 19 (2017) 276–283, https://doi.org/10.1016/j.jcou.2017.04.006.

[21] J.H. Koh, D.H. Won, T. Eom, N.-K. Kim, K.D. Jung, H. Kim, Y.J. Hwang, B.K. Min, Facile CO_2 electro-reduction to formate via oxygen bidentate intermediate stabilized by high-index planes of Bi dendrite catalyst, ACS Catal. 7 (2017) 5071–5077, https://doi.org/10.1021/acscatal.7b00707.

[22] School of Chemistry and Chemical Engineering, Jiangsu University, Zhenjiang 212013, P.R. China, L. Shao, A Highly Efficient Bi-based Electrocatalyst for the Reduction of CO2 to Formate, Int. J. Electrochem. Sci., 2019, 114–125. ⟨https://doi.org/10.20964/2019.01.28⟩.

[23] C.W. Lee, J.S. Hong, K.D. Yang, K. Jin, J.H. Lee, H.-Y. Ahn, H. Seo, N.-E. Sung, K. T. Nam, Selective electrochemical production of formate from carbon dioxide with bismuth-based catalysts in an aqueous electrolyte, ACS Catal. 8 (2018) 931–937, https://doi.org/10.1021/acscatal.7b03242.

[24] H. Zhong, Y. Qiu, T. Zhang, X. Li, H. Zhang, X. Chen, Bismuth nanodendrites as a high performance electrocatalyst for selective conversion of CO_2 to formate, J. Mater. Chem. A 4 (2016) 13746–13753, https://doi.org/10.1039/C6TA06202D.

[25] P. Su, W. Xu, Y. Qiu, T. Zhang, X. Li, H. Zhang, Ultrathin bismuth nanosheets as a highly efficient CO_2 reduction electrocatalyst, ChemSusChem 11 (2018) 848–853, https://doi.org/10.1002/cssc.201702229.

[26] P.-Q. Liao, J.-Q. Shen, J.-P. Zhang, Metal–organic frameworks for electrocatalysis, Coord. Chem. Rev 373 (2018) 22–48, https://doi.org/10.1016/j.ccr.2017.09.001.

[27] F.N. Al-Rowaili, A. Jamal, M.S. Ba Shammakh, A. Rana, A review on recent advances for electrochemical reduction of carbon dioxide to methanol using metal–organic framework (MOF) and non-MOF catalysts: challenges and future prospects, ACS Sustain. Chem. Eng. 6 (2018) 15895–15914, https://doi.org/10.1021/acssuschemeng.8b03843.

[28] H.-F. Wang, L. Chen, H. Pang, S. Kaskel, Q. Xu, MOF-derived electrocatalysts for oxygen reduction, oxygen evolution and hydrogen evolution reactions, Chem. Soc. Rev. 49 (2020) 1414–1448, https://doi.org/10.1039/C9CS00906J.

[29] K. Ping, A. Braschinsky, M. Alam, R. Bhadoria, V. Mikli, A. Mere, J. Aruväli, P. Paiste, S. Vlassov, M. Kook, M. Rähn, V. Sammelselg, K. Tammeveski, N. Kongi, P. Starkov, Fused hybrid linkers for metal–organic framework-derived bifunctional oxygen electrocatalysts, ACS Appl. Energy Mater. 3 (2020) 152–157, https://doi.org/10.1021/acsaem.9b02039.

[30] K. Ping, M. Alam, S.R. Kahnert, R. Bhadoria, A. Mere, V. Mikli, M. Käärik, J. Aruväli, P. Paiste, A. Kikas, V. Kisand, I. Järving, J. Leis, N. Kongi, P. Starkov, Multi-purpose heterogeneous catalyst material from an amorphous cobalt metal–organic framework, Mater. Adv. 2 (2021) 4009–4015, https://doi.org/10.1039/D1MA00414J.

[31] C. Cao, D. Ma, J. Gu, X. Xie, G. Zeng, X. Li, S. Han, Q. Zhu, X. Wu, Q. Xu, Metal–organic layers leading to atomically thin bismuthene for efficient carbon dioxide electroreduction to liquid fuel, Angew. Chem. Int. Ed. 59 (2020) 15014–15020, https://doi.org/10.1002/anie.202005577.

[32] P. Deng, F. Yang, Z. Wang, S. Chen, Y. Zhou, S. Zaman, B.Y. Xia, Metal–organic framework-derived carbon nanorods encapsulating bismuth oxides for rapid and selective CO_2 electroreduction to formate, Angew. Chem. Int. Ed. 59 (2020) 10807–10813, https://doi.org/10.1002/anie.202000657.

[33] N. Kornienko, Y. Zhao, C.S. Kley, C. Zhu, D. Kim, S. Lin, C.J. Chang, O.M. Yaghi, P. Yang, Metal–organic frameworks for electrocatalytic reduction of carbon dioxide, J. Am. Chem. Soc. 137 (2015) 14129–14135, https://doi.org/10.1021/jacs.5b08212.

[34] B. Zhang, S. Cao, Y. Wu, P. Zhai, Z. Li, Y. Zhang, Z. Fan, C. Wang, X. Zhang, J. Hou, L. Sun, Metal-organic-framework-derived bismuth nanosheets for electrochemical and solar-driven electrochemical CO_2 reduction to formate, ChemElectroChem 8 (2021) 880–886, https://doi.org/10.1002/celc.202001613.

[35] S.-M. Hwang, S.Y. Choi, M.H. Youn, W. Lee, K.T. Park, K. Gothandapani, A. N. Grace, S.K. Jeong, Investigation on electroreduction of CO_2 to formic acid using $Cu_3(BTC)_2$ metal–organic framework (Cu-MOF) and graphene oxide, ACS Omega 5 (2020) 23919–23930, https://doi.org/10.1021/acsomega.0c03170.

[36] E. Zhang, T. Wang, K. Yu, J. Liu, W. Chen, A. Li, H. Rong, R. Lin, S. Ji, X. Zheng, Y. Wang, L. Zheng, C. Chen, D. Wang, J. Zhang, Y. Li, Bismuth single atoms resulting from transformation of metal–organic frameworks and their use as electrocatalysts for CO_2 reduction, J. Am. Chem. Soc. 141 (2019) 16569–16573, https://doi.org/10.1021/jacs.9b08259.

[37] W.-W. Yuan, J.-X. Wu, X.-D. Zhang, S.-Z. Hou, M. Xu, Z.-Y. Gu, In situ transformation of bismuth metal–organic frameworks for efficient selective electroreduction of CO_2 to formate, J. Mater. Chem. A 8 (2020) 24486–24492, https://doi.org/10.1039/D0TA08092F.

[38] K. Ping, M. Alam, M. Käärik, J. Leis, N. Kongi, I. Järving, P. Starkov, Surveying iron–organic framework TAL-1-derived materials in ligandless heterogeneous oxidative catalytic transformations of alkylarenes, Synlett 30 (2019) 1536–1540, https://doi.org/10.1055/s-0037-1611877.

[39] J. Enkovaara, C. Rostgaard, J.J. Mortensen, J. Chen, M. Dułak, L. Ferrighi, J. Gavnholt, C. Glinsvad, V. Haikola, H.A. Hansen, H.H. Kristoffersen, M. Kuisma, A.H. Larsen, L. Lehtovaara, M. Ljungberg, O. Lopez-Acevedo, P.G. Moses, J. Ojanen, T. Olsen, V. Petzold, N.A. Romero, J. Stausholm-Møller, M. Strange, G. A. Tritsaris, M. Vanin, M. Walter, B. Hammer, H. Häkkinen, G.K.H. Madsen, R. M. Nieminen, J.K. Nørskov, M. Puska, T.T. Rantala, J. Schiøtz, K.S. Thygesen, K. W. Jacobsen, Electronic structure calculations with GPAW: a real-space implementation of the projector augmented-wave method, J. Phys. Condens. Matter 22 (2010), 253202, https://doi.org/10.1088/0953-8984/22/25/253202.

[40] B. Hammer, L.B. Hansen, J.K. Nørskov, Improved adsorption energetics within density-functional theory using revised Perdew-Burke-Ernzerhof functionals, Phys. Rev. B 59 (1999) 7413–7421, https://doi.org/10.1103/PhysRevB.59.7413.

[41] V. Tripkovic, M. Vanin, M. Karamad, M.E. Björketun, K.W. Jacobsen, K. S. Thygesen, J. Rossmeisl, Electrochemical CO_2 and CO reduction on metal-functionalized porphyrin-like graphene, J. Phys. Chem. C 117 (2013) 9187–9195, https://doi.org/10.1021/jp306172k.

[42] S. Grimme, C. Bannwarth, E. Caldeweyher, J. Pisarek, A. Hansen, A general intermolecular force field based on tight-binding quantum chemical calculations, J. Chem. Phys. 147 (2017), 161708, https://doi.org/10.1063/1.4991798.

[43] N. Han, Y. Wang, L. Ma, J. Wen, J. Li, H. Zheng, K. Nie, X. Wang, F. Zhao, Y. Li, J. Fan, J. Zhong, T. Wu, D.J. Miller, J. Lu, S.-T. Lee, Y. Li, Supported cobalt polyphthalocyanine for high-performance electrocatalytic CO_2 reduction, Chem 3 (2017) 652–664, https://doi.org/10.1016/j.chempr.2017.08.002.

[44] J.K. Nørskov, J. Rossmeisl, A. Logadottir, L. Lindqvist, J.R. Kitchin, T. Bligaard, H. Jónsson, Origin of the overpotential for oxygen reduction at a fuel-cell cathode, J. Phys. Chem. B 108 (2004) 17886–17892, https://doi.org/10.1021/jp047349j.

[45] A. Dutta, I. Zelocualtecatl Montiel, K. Kiran, A. Rieder, V. Grozovski, L. Gut, P. Broekmann, A. Tandem, Bi2O3 → Bimet) catalyst for highly efficient ec-CO_2 conversion into formate: operando Raman spectroscopic evidence for a reaction pathway change, ACS Catal. 11 (2021) 4988–5003, https://doi.org/10.1021/acscatal.0c05317.

[46] B. Ávila-Bolívar, L. García-Cruz, V. Montiel, J. Solla-Gullón, Electrochemical reduction of CO_2 to formate on easily prepared carbon-supported Bi nanoparticles, Molecules 24 (2019) 2032, https://doi.org/10.3390/molecules24112032.

[47] H. Louis, O.U. Akakuru, P. Monday, O.O. Funmilayo, A review on the state-of-the-art advances for CO_2 electro-chemical reduction using metal complex molecular catalysts, Eclética Quím. J. 44 (2019) 11, https://doi.org/10.26850/1678-4618eqj.v44.1.2019.p11-39.

[48] X. Zhang, Y. Zhang, Q. Li, X. Zhou, Q. Li, J. Yi, Y. Liu, J. Zhang, Highly efficient and durable aqueous electrocatalytic reduction of CO $_2$ to HCOOH with a novel bismuth–MOF: experimental and DFT studies, J. Mater. Chem. A 8 (2020) 9776–9787, https://doi.org/10.1039/D0TA00384K.

[49] P. Deng, H. Wang, R. Qi, J. Zhu, S. Chen, F. Yang, L. Zhou, K. Qi, H. Liu, B.Y. Xia, Bismuth oxides with enhanced bismuth–oxygen structure for efficient electrochemical reduction of carbon dioxide to formate, ACS Catal. 10 (2020) 743–750, https://doi.org/10.1021/acscatal.9b04043.

[50] W. Oh, C.K. Rhee, J.W. Han, B. Shong, Atomic and molecular adsorption on the Bi (111) surface: insights into catalytic CO $_2$ reduction, J. Phys. Chem. C 122 (2018) 23084–23090, https://doi.org/10.1021/acs.jpcc.8b07865.

[51] Ph. Hofmann, The surfaces of bismuth: structural and electronic properties, Prog. Surf. Sci. 81 (2006) 191–245, https://doi.org/10.1016/j.progsurf.2006.03.001.

[52] H. Mönig, J. Sun, Yu.M. Koroteev, G. Bihlmayer, J. Wells, E.V. Chulkov, K. Pohl, Ph Hofmann, Structure of the (111) surface of bismuth: LEED analysis and first-principles calculations, Phys. Rev. B 72 (2005), 085410, https://doi.org/10.1103/PhysRevB.72.085410.

Publication IV

Mahboob Alam, Kefeng Ping, Mati Danilson, Valdek Mikli, Maike Käärik, Jaan Leis, Jaan Aruväli, Päärn Paiste, Mihkel Rähn, Väino Sammelselg, Kaido Tammeveski, Ulrike Kramm, Nadezda Kongi, Pavel Starkov

Comparison of benzimidazolediol-derived iron triad M–N–C nanomaterials as trifunctional catalysts in alkaline and acidic media

Manuscript submitted.

The rules of the publisher prevent publication of the manuscript of Publication IV prior to the acceptance. Official committee members and opponents will be given a copy of the manuscript to enable them to carry out a judicious review of the dissertation.

Curriculum vitae

Personal data

Name	Mahboob Alam
Date of birth	April 16, 1993
Place of birth	Kasur, Pakistan
Citizenship	Pakistani

Contact details

E-mail	mahboob218@gmail.com

Education

2018–2022	PhD in Chemistry Tallinn University of Technology Dept of Chemistry and Biotech
2016–2018	MSc in Applied Measurement Science University of Tartu
2010–2015	BSc in Chemistry Univesity of the Punjab

Languages and Skills

English (intermediate), Urdu (native); synthetic materials chemistry (NMR, UV–Vis, FTIR); materials science (PXRD, SEM, TEM, XPS, Raman), TopSpin, MestReNova, ImageJ/Fiji, ChemDraw, Origin, EndNote, MS Office.

Publications

Yusibova, G.; Alam, M.; Ping, K.; Sild, S.; Vlassov, S.; Šmits, K.; Aruväli, J.; Käärik, M.; Leis, J.; Starkov, P.; Maran, U.; Kongi, N. Computationally rationalizing tpost-treatment of multifunctional cobalt-based heterogeneous materials for oxygen reduction/evolution reactions. *Manuscript in prep.*

Alam, M.; Ping, K.; Danilson, M.; Mikli, V.; Käärik, M.; Leis, J.; Aruväli, J.; Paiste, P.; Rähn, M.; Sammelselg, V.; Tammeveski, K.; Kramm, U.; Kongi, N.; Starkov, P. Comparison of benzimidazolediol-derived iron triad M–N–C nanomaterials as trifunctional catalysts in alkaline and acidic media. *Manuscript submitted.*

Ávila-Bolívar, B.; Cepitis, R.; Alam, M.; Assafrei, J.-M.; Ping, K.; Aruväli, J.; Kikas, A.; Kisand, V.; Vlassov, S.; Ivaništštev, V.; Starkov, P.; Montiel, V.; Solla-Gullón, J.; Kongi, N. CO_2 reduction to formate on an affordable bismuth metal–organic framework based catalyst. *J. CO_2 Util.* **2022,** *59,* 101937.
DOI:10.1016/j.jcou.2022.101937

Ping, K.; Alam, M.; Kahnert, S. R.; Bhadoria, R.; Mere, A.; Mikli, V.; Käärik, M.; Aruväli, J.; Paiste, P.; Kikas, A.; Kisand, V.; Järving, I.; Leis, J.; Tammeveski, K.; Kongi, N.; Starkov, P. Multi-purpose chemo- and electrocatalyst material from an amorphous cobalt metal–organic framework. *Mater. Adv.* **2021,** *2,* 4005–4019.
DOI: 10.1039/D1MA00414J

Kazimova, N.; Ping, K.; Danilson, M.; Merisalu, M.; Aruväli, J.; Käärik, M.; Mikli, V.; Leis, J.; Tammeveski, K.; Starkov, P.; Kongi, N. Shungite-derived graphene as a carbon support for bifunctional oxygen electrocatalysts. *J. Catal.* **2021,** *395,* 178–187.
DOI: 10.1016/j.jcat.2021.01.004

Ping, K.; Brashinsky, A.; Alam, M.; Bhadoria, R.; Mihkli, V.; Mere, A.; Vlassov, S.; Kook, M.; Rähn, M.; Sammelselg, V.; Aruväli, J.; Tammeveski, K.; Kongi, N.; Starkov, P. Fused hybrid linkers for metal–organic framework-derived bifunctional oxygen electrocatalysts. *ACS Appl. Energy Mater.* **2020**, *3*, 152–157.
DOI: 10.1021/acsaem.9b02039

Ping, K.; Alam, M.; Käärik, M.; Leis, J.; Kongi, N.; Järving, I.; Starkov, P. Surveying iron–organic framework TAL–1-derived materials in ligandless heterogeneous oxidative catalytic transformations of alkylarenes. *Synlett* **2019**, *30*, 1536–1540. [invited]
DOI: 10.1055/s-0037-1611877

Elulookirjeldus

Isikuandmed

Nimi	Mahboob Alam
Sünniaeg	March 16, 1993
Sünnikoht	Kasur, Pakistan
Kodakondsus	pakistanlane

Kontaktandmed

E-mail	mahboob218@gmail.com

Hariduskäik

2018–2022	PhD (keemia) Tallinna Tehnikaülikool Keemia ja biotehnoloogia instituut
2016–2018	MSc (rakenduslik mõõteteadus) Tartu ülikool
2010–2015	BSc (keemia) Punjabi ülikooli

Keelte- ja muud oskused

Inglise (C1), urdu (emakeel); sünteetiline materjalide keemia (TMR, UV–Vis, FTIR); materjalitehnoloogia (PXRD, SEM, TEM, XPS, Raman); TopSpin, MestReNova, ImageJ/Fiji, ChemDraw, Origin, EndNote, MS Office.

Publikatsioonid

Yusibova, G.; Alam, M.; Ping, K.; Sild, S.; Vlassov, S.; Šmits, K.; Aruväli, J.; Käärik, M.; Leis, J.; Starkov, P.; Maran, U.; Kongi, N. Computationally rationalizing tpost-treatment of multifunctional cobalt-based heterogeneous materials for oxygen reduction/evolution reactions. *Manuscript in prep.*

Alam, M.; Ping, K.; Danilson, M.; Mikli, V.; Käärik, M.; Leis, J.; Aruväli, J.; Paiste, P.; Rähn, M.; Sammelselg, V.; Tammeveski, K.; Kramm, U.; Kongi, N.; Starkov, P. Comparison of benzimidazolediol-derived iron triad M–N–C nanomaterials as trifunctional catalysts in alkaline and acidic media. *Manuscript submitted.*

Ávila-Bolívar, B.; Cepitis, R.; Alam, M.; Assafrei, J.-M.; Ping, K.; Aruväli, J.; Kikas, A.; Kisand, V.; Vlassov, S.; Ivaništštev, V.; Starkov, P.; Montiel, V.; Solla-Gullón, J.; Kongi, N. CO_2 reduction to formate on an affordable bismuth metal–organic framework based catalyst. *J. CO_2 Util.* **2022,** *59,* 101937.
DOI:10.1016/j.jcou.2022.101937

Ping, K.; Alam, M.; Kahnert, S. R.; Bhadoria, R.; Mere, A.; Mikli, V.; Käärik, M.; Aruväli, J.; Paiste, P.; Kikas, A.; Kisand, V.; Järving, I.; Leis, J.; Tammeveski, K.; Kongi, N.; Starkov, P. Multi-purpose chemo- and electrocatalyst material from an amorphous cobalt metal–organic framework. *Mater. Adv.* **2021,** *2,* 4005–4019.
DOI: 10.1039/D1MA00414J

Kazimova, N.; Ping, K.; Danilson, M.; Merisalu, M.; Aruväli, J.; Käärik, M.; Mikli, V.; Leis, J.; Tammeveski, K.; Starkov, P.; Kongi, N. Shungite-derived graphene as a carbon support for bifunctional oxygen electrocatalysts. *J. Catal.* **2021,** *395,* 178–187.
DOI: 10.1016/j.jcat.2021.01.004

Ping, K.; Brashinsky, A.; Alam, M.; Bhadoria, R.; Mihkli, V.; Mere, A.; Vlassov, S.; Kook, M.; Rähn, M.; Sammelselg, V.; Aruväli, J.; Tammeveski, K.; Kongi, N.; Starkov, P. Fused hybrid linkers for metal–organic framework-derived bifunctional oxygen electrocatalysts. *ACS Appl. Energy Mater.* **2020**, *3*, 152–157.
DOI: 10.1021/acsaem.9b02039

Ping, K.; Alam, M.; Käärik, M.; Leis, J.; Kongi, N.; Järving, I.; Starkov, P. Surveying iron–organic framework TAL–1-derived materials in ligandless heterogeneous oxidative catalytic transformations of alkylarenes. *Synlett* **2019**, *30*, 1536–1540. [invited]
DOI: 10.1055/s-0037-1611877

ISSN 2585-6901 (PDF)
ISBN 978-9949-83-910-0 (PDF)